UNIVERSITY OF CALIFORNIA, SAN DIEGO

Sliding Contacts and the Dynamics of Magnetic Tape Transport

A Dissertation submitted in partial satisfaction of the

requirements for the degree of Doctor of Philosophy

in

Engineering Sciences (Mechanical Engineering)

by

Bart Raeymaekers

Committee in charge:

Professor Frank E. Talke, Chair
Professor David J. Benson, Co-Chair
Professor Raymond A. de Callafon
Professor Kenneth Kreutz-Delgado
Professor Jack K. Wolf

2007

The Dissertation of Bart Raeymaekers is approved, and it is acceptable in quality and form for publication on microfilm:

_____

_____

_____

_____
Co-Chair

_____
Chair

University of California, San Diego

2007

TABLE OF CONTENTS

LIST OF SYMBOLS

Symbol	Description	Unit
a	Radius of the cylindrical guide	m
A	Cross sectional area of tape	m²
A_{az}	Amplitude of lateral displacement due to reel azimuth angle	m
b	Tape thickness	m
B	Magnetic inductance	Tesla
B_r	Remanent Magnetism	Tesla
c	minimum tape/guide spacing	m
c_1	Damping of voice coil motor	Nsm^{-1}
c_2	Damping of PZT micro-actuator	Nsm^{-1}
$\boldsymbol{c}$	Unit vector of bending moment	
C	Magnitude of bending moment	Nm
C_v	Maximum non-dimensional contact pressure at yield inception in slip (frictionless)	
$\boldsymbol{C}$	Bending moment vector	
d	Matrix of piezoelectric constants	CN^{-1}
$d_{\max}$	Maximum tape deflection	m
D	Diameter of the tape pack	m
$\boldsymbol{e}_r, \boldsymbol{e}_\varphi, \boldsymbol{k}$	Unit vectors, representing the basis of the r, φ, z coordinate	

	system	
E	Young's modulus	Nm^{-2}
$\boldsymbol{E}$	Electric field strength	NC^{-1}
f	Frequency	Hz
f_{imp}	Tape edge impact force	N
f_0	Experimentally measured LTM at point s_0	m
$f_{1,2}$	Arbitrary functions f_1 and f_2	
$\boldsymbol{f}_f$	Unit vector of friction force	
F_s	Spring force	N
F_{em}	Electromagnetic force	N
F_p	Point force	N
F_a	Harmonic force	N
F_0	Reaction force of roller flange	N
F_f	Magnitude of (local) friction force	N
$\boldsymbol{F}_f$	Friction force vector	
g	Gravitational acceleration	ms^{-2}
g_{imp}	Transfer function for the tape edge impact measurement circuit	
$h(x,y)$	Tape/guide spacing in global coordinates	m
h_p	Depth of dimple	m

h_d	Ball drop height	m
h_R	Tape curvature value	m
$h^*\left(x^*, y^*\right)$	Tape/guide spacing in local coordinates	m
$\overline{h}$	Dimensionless tape/guide spacing, $\overline{h} = h / \sigma_s$	
H	Heaviside function	
H	Magnetic field strength	Am^{-1}
H_c	Coercivity	Am^{-1}
$H\left(X, Y\right)$	Dimensionless spacing in global coordinates, $H = h / c$	
$H^*\left(X^*, Y^*\right)$	Dimensionless spacing in local coordinates, $H^* = h^* / c$	
i	Index refering to space grid	
I	Moment of inertia	m^4
I_c	Electric current flowing through a coil	A
$\boldsymbol{i}, \boldsymbol{j}, \boldsymbol{k}$	Unit vectors, representing the basis of the x, y, z coordinate system	
j	Index refering to time grid	
k	Effective tape stiffness	Nm^{-1}
k_0	Stiffness of roller flange	Nm^{-1}
k_1	Stiffness of voice coil motor	Nm^{-1}
k_2	Stiffness of PZT micro-actuator	Nm^{-1}
l	Length of a beam (tape) element	m

l_c	Length of the coil	m
L	Position of flange	m
L_C	Critical normal load at yield inception under frictional contact	N
$\overline{L_C}$	Normalized critical normal load at yield inception under frictional contact, $\overline{L_C} = L_C / P_C$	
l_1	Length along the tape centerline between s_0 and s_1	m
l_2	Length along the tape centerline between s_1 and s_2	m
l_3	Length along the tape centerline between s_2 and s_3	m
m	Mass	kg
m_0 , m_2 , m_4	Spectral moments of the surface roughness	
$\boldsymbol{M}$	Position vector, describing the position of a point on the centerline of the tape	
n	Number of contacting asperities	
$\boldsymbol{n}$	Unit vector of normal force	
N	Magnitude of normal force, maximum tape/guide contact load in the absence of any air bearing support	N
N_c	Number of windings on the coil	
N_{asp}	Load portion carried by the contacting asperities	N
dN_{asp}	Increment of load portion carried by the contacting asperities	N
$\boldsymbol{N}$	Normal force vector	

$p(x,y)$	Air bearing pressure	Nm^{-2}
p_a	Atmospheric pressure	Nm^{-2}
p_{avg}	Average air bearing pressure	Nm^{-2}
$P(X,Y)$	Dimensionless air bearing pressure, $P = p / p_a$	
P_{asp}	Normal load on one asperity	N
P_C	Critical normal load at yield inception in slip (frictionless)	N
P^*	Dimensionless load on one asperity, $P^* = P / L_C$	
r	Radius of the asperity tip	m
r_1	Imaginary cell half length	m
r_p	Dimple radius	m
r_{corr}	Cross-correlation coefficient	
R	Radius of curvature	m
s	Laplace transform parameter	
s	Spatial coordinate along the tape centerline	m
s_0	Startpoint of the domain	
s_1	Point where the tape first contacts the guide	
s_2	Point where the tape comes off the guide	
s_3	Endpoint of the domain	
ds	Length of infinitesimal tape element	m
Δs	Spatial grid stepsize	m

S	Tape edge contact area	m^2
S_p	Dimple area density	
S^E	Compliance matrix	m^2N^{-1}
t	Time	s
Δt	Time stepsize	s
$\boldsymbol{t}$	Unit vector of tape tension	
T	Magnitude of (local) tape tension	N
T_1	"Tight-side" tension	N
T_2	"Slack-side" tension	N
dT	Infinitesimal tape tension change	N
ΔT	Tape tension change	N
$\boldsymbol{T}$	Tape tension vector	
u_1	Actuation force of voice coil motor	N
u_2	Actuation force of PZT micro-actuator	N
U	Tape speed	ms^{-1}
v	Output voltage of acoustic emission sensor	V
v_c	Induced voltage	V
$\boldsymbol{v}$	Unit vector of shear force	
V	Magnitude of shear force	N
$\boldsymbol{V}$	Shear force vector	
w	Width of tape	m

x, y, z	Cartesian coordinate system	
r, φ, z	Cylindrical coordinate system	
x , y	Global coordinates	m
y_{sh}	Position of the servo head	m
y_{st}	Position of the servo track	m
y_{edge}	Position of the tape edge	m
y_{var}	Servo track variability	m
x^* , y^*	Local coordinates	m
X , Y	Dimensionless global coordinates, $X = x / r_p$, $Y = y / r_p$	
X^*, Y^*	Dimensionless local coordinate, $X^* = x^* / r_p$, $Y^* = y^* / r_p$	
Y	Yield strength	Nm^{-2}
α	Angular coordinate	RAD
$d\alpha$	Increment of angular coordinate	RAD
α_{az}	Reel azimuth angle	RAD
α^*	Spacing at which head/tape contact begins	m
β	Asperity load factor	
β^*	Pressure required force zero spacing between the head and the tape	Nm^{-2}
γ	Over-relaxation parameter	
Γ	Local non-dimensional tape tension (= P^*) $\Gamma = P_{asp} / L_C$	

Γ_2	Dimensionless "slack-side" tension	
δ	Dimensionless minimum tape/guide spacing, $\delta = c / 2r_p$	
ε	Dimple aspect ratio, $\varepsilon = h_p / 2r_p$	
$\boldsymbol{\varepsilon}$	Strain vector	
ζ	Amplitude ratio	
η	Asperity density	
θ	Wrap angle	RAD
λ	Flow parameter, $\lambda = 3\mu_a U / 2r_p p_a$	
λ_a	Mean free path of air under atmospheric conditions	m
μ	(Isotropic) friction coefficient	
μ_a	Air viscosity	$Nm^{-2}s$
μ_φ	Friction coefficient in the circumferential direction	
μ_z	Friction coefficient in the z-direction	
ν	Poisson's ratio	
ν	Ratio of the friction coefficients in the circumferential and vertical direction, $\nu = \mu_\varphi / \mu_z$	
ρ	Tape density	kgm^{-3}
σ	Stress, Stress wave	Nm^{-2}
$\boldsymbol{\sigma}$	Stress vector	
σ_s	Standard deviation of asperity summit heights distribution	m

τ	Variable of integration	
τ	Shear stress	Nm^{-2}
Φ	Magnetic flux	Wb
ψ	Plasticity index	
ψ	Slope of tape with respect to a plane perpendicular to the z-axis	RAD
ω	Rotational frequency	$RADs^{-1}$
ω_C	Critical interference of a single asperity at yield inception	
ω_n	Natural frequency of tape element	Hz
ω_r	Rotational frequency of tape reel	Hz

LIST OF FIGURES

LIST OF TABLES

ACKNOWLEDGEMENTS

First of all, I would like to thank my advisor Professor Frank E. Talke for his continuous support and advice, which significantly contributed to the successful completion of this dissertation. Professor Talke encouraged me to pursue a Ph.D., and I could not have imagined having a better advisor and mentor. Professor Talke has been more than just a Ph.D. advisor and for that I would like to express my special gratitude and thanks.

Next, I would like to thank Dr. Ryan Taylor for introducing me into magnetic tape technology. His effort and helpfulness definitely gave me a head-start on my research project. Furthermore, I want to express my gratitude to the faculty and students I have worked with over the course of my Ph.D. study at the University of California, San Diego. In particular Maik Duwensee, Aravind Murthy, Ralf Brunner, John Xu, Paul Yoon and Yu-Chen Wu, who helped in various aspects of my research. Special thanks to Professor Raymond de Callafon and Matthew Graham for the valuable discussions and help on the design of the dual stage actuator head.

I also would like to express my appreciation to machinist Jack Philhower and to electronics-wizard Ray Descoteaux, who helped me with the realization of experimental set-ups, and to Betty Manoulian and Iris Villanueva for the help with administrative matters.

Furthermore, I wish to thank Professor Izhak Etsion from the Israel Institute of Technology in Haifa, Israel. I very much admire his dedication, patience and drive. I appreciate his help and advice inside as well as outside the lab. The help of Professor Etsion's company Surface Technologies Ltd. in providing laser surface texturing is also greatly acknowledged.

Finally I would like to thank my parents Wim Raeymaekers and Luce Vanderhauwaert who persistently supported me mentally and financially throughout my study career and also encouraged my move to the U.S.A.

Chapter 2, in part, is a reprint of the material as it appears in "Non-Contact Tape Tension Measurement and Correlation of Lateral Tape Motion and Tape Tension Transients", Raeymaekers B., Taylor R.J., Talke F.E., Microsystem Technologies, 2006. The dissertation author was the primary investigator and author of this paper.

Chapter 3, in part, is a reprint of the material as it appears in "Characterization of Tape Edge Contact Force with Acoustic Emission", Raeymaekers B., Talke F.E., Journal of Vibration and Acoustics Transactions of the ASME, 2007. The dissertation author was the primary investigator and author of this paper.

Chapter 4, in part, is a reprint of the material as it appears in "Lateral Motion of an Axially Moving Tape on a Cylindrical Guide Surface", Raeymaekers B., Talke F.E.,

Journal of Applied Mechanics Transactions of the ASME, 2007. The dissertation author was the primary investigator and author of this paper.

Chapter 4, in part, has been submitted for publication in "Attenuation of Lateral Tape Motion Due to Frictional Interaction with a Cylindrical Guide", Raeymaekers B., Talke F.E., Tribology International, 2007. The dissertation author was the primary investigator and author of this paper.

Chapter 5, in part, is a reprint of the material as it appears in "The Influence of Operating and Design Parameters on the Magnetic Tape/Guide Friction Coefficient", Raeymaekers B., Etsion I., Talke F.E., Tribology Letters, 2007. The dissertation author was the primary investigator and author of this paper.

Chapter 6, in part, is a reprint of the material as it appears in "Enhancing the Tribological Performance of the Magnetic Tape/Guide Interface by Laser Surface Texturing", Raeymaekers B., Etsion I., Talke F.E., Tribology Letters, 2007. The dissertation author was the primary investigator and author of this paper.

Chapter 6, in part, has been submitted for publication in "A Model for Magnetic Tape/Guide Friction Reduction by Laser Surface Texturing", Raeymaekers B., Etsion I., Talke F.E., Tribology Letters, 2007. The dissertation author was the primary investigator and author of this paper.

VITA

2002	Industrieel Ingenieur Electromechanica (ing.), Katholieke Hogeschool St. Lieven, Ghent, Belgium
2004	Burgerlijk Ingenieur Werktuigkunde-Electrotechniek (ir.), Vrije Universiteit Brussel, Brussels, Belgium
2004	Belgian American Educational Foundation Fellow and Francqui Foundation Fellow
2004-2007	Research Assistant and Teaching Assistant, University of California, San Diego, USA
2005	Master of Science, University of California, San Diego, USA
2007	Doctor of Philosophy, University of California, San Diego, USA

PUBLICATIONS

Journal Papers:

A1. Raeymaekers B, Taylor RJ, Talke FE, 2006, Non-Contact Tape Tension Measurement and Correlation of Lateral Tape Motion and Tape Tension Transients; *Microsystem Technologies, Vol. 12(4), pp. 814 - 821*

A2. Raeymaekers B, Etsion I, Talke FE, 2007, The Influence of Operating and Design Parameters on the Magnetic Tape/Guide Friction Coefficient; *Tribology Letters, Vol. 25(2), pp. 161 - 171*

A3. Raeymaekers B, Etsion I, Talke FE, 2007, Enhancing Tribological Performance of the Magnetic Tape/Guide Interface by Laser Surface Texturing; *Tribology Letters*, *Vol. 27(1), pp. 89 - 95*

A4. Raeymaekers B, Talke FE, 2007, Lateral Motion of an Axially Moving Tape on a Cylindrical Guide Surface; *Journal of Applied Mechanics T ASME,* in press

A5. Raeymaekers B, Talke FE, 2007, Characterization of Tape Edge Contact with Acoustic Emission; *Journal of Vibration and Acoustics T ASME*, in press

A6. Raeymaekers B, Etsion I, Talke FE, 2007, A Model for Magnetic Tape/Guide Friction Reduction by Laser Surface Texturing; *Tribology Letters,* in press

A7. Raeymaekers B, Talke FE, 2007, Attenuation of Lateral Tape Motion Due to Frictional Interaction with a Cylindrical Guide; submitted to *Tribology International*, under review

A8. Raeymaekers B, Lee DE, Talke FE, 2007, A Study of the Brush/Rotor Interface of a Homopolar Motor using Acoustic Emission; submitted to *Tribology International*, under review

A9. Raeymaekers B, Graham MR, de Callafon RA, Talke FE, 2007, Design of a Dual Stage Actuator Tape Head with High-Bandwidth Track Following Capability; to be submitted to *IEEE T Magnetics*

A10. Raeymaekers B, Talke FE, 2007, Measurement and Sources of Lateral Tape Motion: A Review; to be submitted to *Journal of Tribology T ASME*

Conference Papers:

B1. Raeymaekers B, Taylor RJ, Talke FE, Correlation of Lateral Tape Motion and Tape Tension Transients; *Proceedings of Information Storage and Processing Systems (ISPS) Conference, Santa Clara, CA (USA), 28-29 June 2005*

B2. Raeymaekers B, Talke FE, The Use of Acoustic Emission for Detection of Tape Edge Contact; *Proceedings of Micromechatronics for Information and Precision Equipment (MIPE) Conference, Santa Clara, CA (USA), 21-23 June 2006*

B3. Raeymaekers B, Etsion I, Talke FE, Influence of Operation Conditions on Tape/Guide Friction; *Proceedings of ASME/STLE International Joint Tribology Conference, San Antonio, TX (USA), 23-25 October 2006*

B4. Raeymaekers B, Talke FE, The Effect of Friction between a Cylindrical Guide and Magnetic Tape on Lateral Tape Motion; *Proceedings of AUSTRIB 06 Conference, Brisbane, Australia, 3-6 December 2006*

B5. Lee DE, Raeymaekers B, Talke FE, In-Situ Monitoring of the Brush/Rotor Interface in a Homopolar Motor with Acoustic Emission; *Proceedings of AUSTRIB 06 Conference, Brisbane, Australia, 3-6 December 2006*

B6. Raeymaekers B, Graham MR, de Callafon RA, Talke FE, Design of a Dual Stage Actuator Tape Head with High-Bandwidth Track Following Capability; *Proceedings of Information Storage and Processing Systems (ISPS) Conference, Santa Clara, CA (USA), 18-20 June 2007*

B7. Raeymaekers B, Etsion I, Talke FE, Reducing the Magnetic Tape/Guide Friction Coefficient by Laser Surface Texturing: Experimental Analysis; *Proceedings of ASME/STLE International Joint Tribology Conference, San Diego, CA (USA), 22-24 October 2007*

B8. Raeymaekers B, Etsion I, Talke FE, A Model for the Magnetic Tape/Guide Interface with Laser Surface Texturing; *Proceedings of ASME/STLE International Joint Tribology Conference, San Diego, CA (USA), 22-24 October 2007*

Patents:

C1. Raeymaekers B, Etsion I, Talke FE, Tape Guiding System and Method, *US Provisional Patent #60/909,832*

C2. Raeymaekers B, Talke FE, New Tape Drive Head Design, *US Provisional Patent #60/916,485*

ABSTRACT OF THE DISSERTATION

Sliding Contacts and the Dynamics of Magnetic Tape Transport

by

Bart Raeymaekers

Doctor of Philosophy in Engineering Sciences (Mechanical Engineering)

University of California, San Diego, 2007

Professor Frank E. Talke, Chair

Professor David J. Benson, Co-Chair

Lateral tape motion (LTM) is the motion of a tape perpendicular to the tape transport direction. It is a problem in magnetic tape recording technology that limits the track density on a tape. To reduce LTM, it is important to characterize the main sources of LTM in tape transports. In this dissertation, the effect of tape edge contact as well as tape tension transients on LTM is investigated. An optical non-contact tension sensor is developed and a correlation between LTM and tension transients is observed. Additionally, a method based on acoustic emission is established to measure tape edge contact. Tape edge contact is observed to cause high frequency LTM, and the magnitude of the impact is shown to be function of the tape pack size.

The dynamics of a tape as it moves over a cylindrical guide are studied theoretically and validated experimentally. Good agreement between theory and experiments is observed. In the experimental analysis, the tape/guide friction coefficient is observed to be function of different operating and design parameters. A model for the friction coefficient between a tape and a cylindrical guide is presented and evaluated with experimental data.

Finally, the use of laser surface texturing (LST) for improved tape guiding is proposed and investigated both experimentally and numerically. LST guides are observed to create an air bearing at low tape speeds and thus reduce the transition speed between boundary lubrication and full fluid lubrication. Additionally, the design of a dual stage actuator tape head for increased bandwidth track-following is introduced, as a means to enable increased track density on a tape for future high performance tape drives.

1. Introduction

1.1 Application and standards

Although magnetic tape recording might seem an old-fashioned technique in the present day storage market dominated by hard disk drives, it is still very much used. Magnetic tape has kept its leadership position in terms of cost per gigabyte with respect to other storage media and therefore remains the primary choice for backup/restore and mass data storage applications. Hundreds or thousands of tape cartridges can be arranged in automated tape libraries to provide fast data access. In addition, it is more reliable to archive data on magnetic tape than on any of its competitors [1.1]. Typically, data can be stored for up to 30 years on a magnetic tape, provided that the ideal temperature and humidity is maintained.

Two magnetic tape recording technologies exist: helical scan recording and linear tape recording, illustrated in Fig. 1.1 a) and Fig. 1.1 b), respectively.

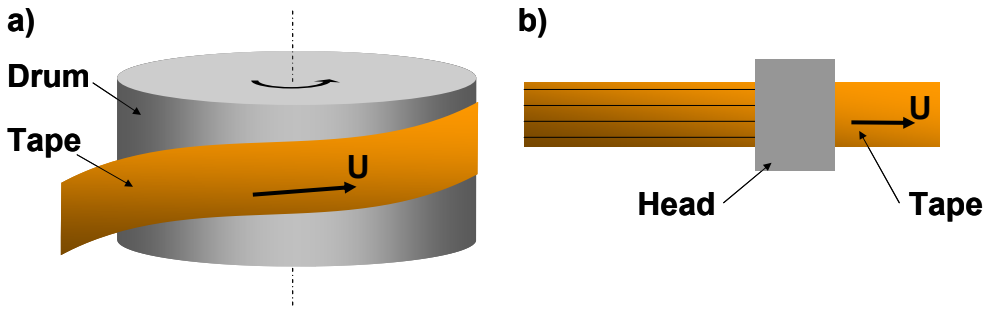

Fig. 1.1: Magnetic tape recording: a) helical scan recording and b) linear recording

In helical scan recording, the recording heads are mounted on a cylindrical drum, which rotates under a specific azimuth angle relative to the tape. The tracks on the magnetic tape are written under the same azimuth angle as the read/write heads are oriented. Helical scan technology was primarily used in video recorders (VCR). Mass data storage and back-up/restore applications, on the other hand, mainly use linear tape recording technology. The research presented in this dissertation is concerned with linear tape recording systems. More specifically, it addresses mechanics and design problems of tape drives operating under the Linear Tape Open (LTO) format, a standard that was introduced in 1998 [1.2].

Currently, the two main standards in linear tape recording are Quantum's (Super) Digital Linear Tape ((S)DLT) and the Linear Tape Open (LTO) format, introduced in 1998 by an industry consortium that consisted of IBM, Hewlett-Packard (HP) and Seagate (now Quantum). A rather small player in the linear tape recording market is Sony's Advanced Intelligent Tape (AIT).

LTO is a so-called "open format", meaning that users have the choice of multiple sources of tape drives and media cartridges [1.2]. The compatibility between the different products and generations (back-compatibility) of the LTO-technology is guaranteed. Currently, two types of the LTO format are commercially available. LTO-Accelis provides fast data-access but does not give high storage capacity. LTO-Ultrium, on the other hand, provides high storage capacity but comes with slow data access time. The LTO format exists in three generations: GEN 1 offers tape cartridges with a

capacity of 100 Gigabyte (GB), GEN 2 offers cartridges with a capacity of 200 GB and GEN 3, which was first released in 2005, comes with a cartridge capacity of 400 GB. LTO tape cartridges allow a 2:1 data compression, which virtually doubles the storage capacity of a cartridge.

1.2 Working principle

Fig. 1.2 shows the magnetization B versus the magnetic field strength H, for a ferro-magnetic material, also known as the magnetic hysteresis loop [1.3].

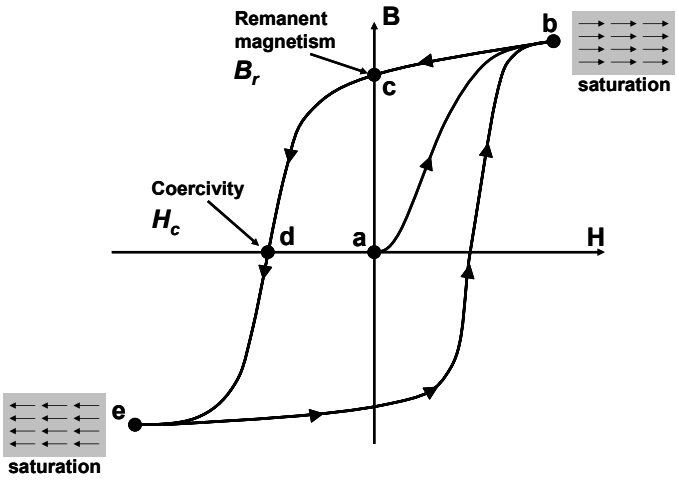

Fig. 1.2: Magnetic hysteresis loop

Ferromagnetic materials consist of regions where the electrons have the same spin. These regions of micro-magnetism are called islands. When the ferromagnetic specimen is not exposed to a magnetic field, the islands are magnetically orientated in an arbitrary direction with respect to one another. The vector sum of the magnetic orientation of the different islands is almost zero. When an external magnetic field of strength H is

applied on the ferromagnetic specimen, the islands align with the direction of the applied magnetic field. Starting at point *a* in Fig. 1.2 and increasing the magnetic field strength H, the islands of the ferromagnetic specimen align with the applied magnetic field until saturation is reached (point *b* in Fig. 1.2). Maximum magnetization is now obtained since all magnetic islands are lined up with one another, i.e., the magnetization vectors of the individual islands point in the same direction. After reducing the external magnetic field strength to zero (point *b* to *c* in Fig. 1.2), the specimen remains magnetized. A permanent magnet has been built, characterized by a distinct magnetization B_r, the so-called "remanent magnetism". It is the remanent magnetism that enables magnetic storage.

Applying an external magnetic field of increasing strength, but in the opposite direction of the previously applied field (point *d* to *e* in Fig. 1.2), results in an alignment of the islands with the applied field, until a new saturation point is reached (point *e* in Fig. 1.2). Now, all islands are aligned with one another in the opposite sense compared to point *b*. Again increasing the field strength in the original direction until saturation is reached (point *b* in Fig. 1.2) closes the "magnetic hysteresis loop". The negative field strength H_c, which results in zero magnetization, is called coercivity (point *d* in Fig. 1.2). The coercivity is therefore the magnitude of the magnetic field that needs to be applied to neutralize the remanent magnetism B_r. Hence, in magnetic recording the coercivity could be thought of as a measure of archival capability of the magnetic medium.

Fig. 1.3 illustrates the working principle of magnetic tape recording. A coil with N_c windings of total length l_c is wound around a magnetic core. A write current I_c flows through the coil and creates a magnetic field of strength H given by

$$H = \frac{N_c I_c}{l_c} \tag{1.1}$$

A so-called fringe field is created perpendicular to this magnetic field of strength *H*, in the plane of the magnetic tape. This fringe field magnetizes the ferromagnetic coating of the tape and, thus, a bit can be recorded. By creating a relative motion between the tape and the write head, a bit stream can be recorded on the magnetic tape. This recording process is referred to as "inductive recording". When moving the inductive head over a previously recorded bit pattern, the magnetization will induce a voltage in the coil according to Faraday's law:

$$v_c = -N_c \frac{d\Phi}{dt} \tag{1.2}$$

where v_c is the induced voltage and Φ is the magnetic flux. t represents the time. Hence, the previously recorded bit pattern can be reproduced by the read head.

A magneto-resistive (MR) read head consists of a small stripe of permalloy, which changes its resistance in the vicinity of a magnetic field, depending on the strength and direction of the field. Hence, a previously recorded bit pattern can be reproduced by monitoring the resistance change of the permalloy in the MR head. An MR head detects weaker magnetic signals and thus allows for smaller bits, or equivalently, higher storage density, and is faster than an inductive recording head.

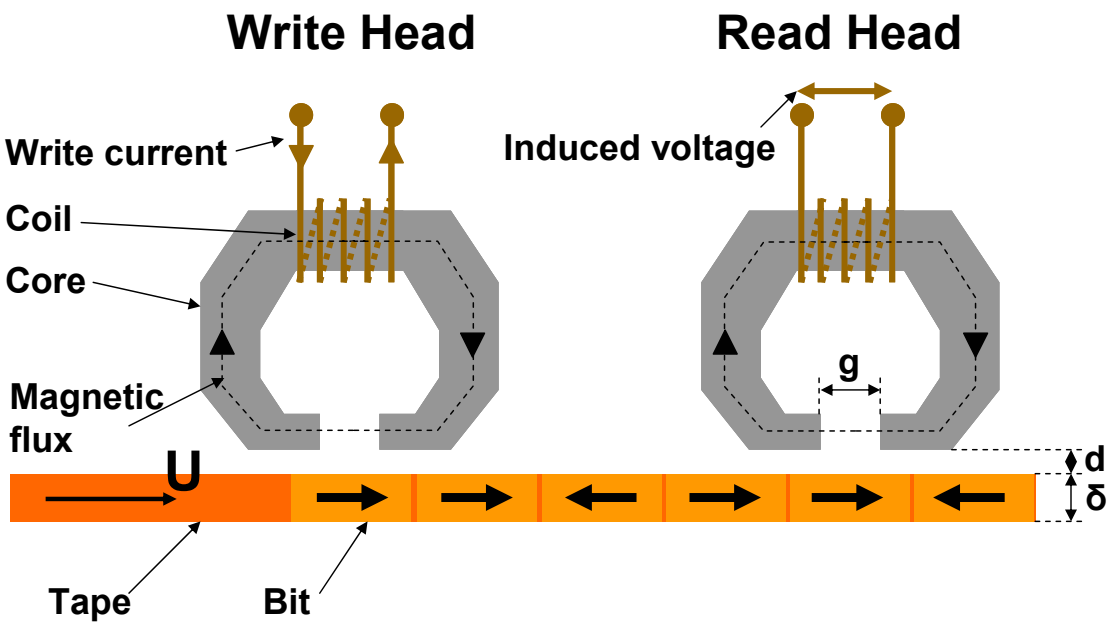

Fig. 1.3: Principle of magnetic tape recording

The magnetic coupling between the read/write head and the magnetic tape is not perfect due to a small air gap that separates both. The Wallace equation relates the induced voltage $v_c(x)$ to the tape/head separation (for sine wave recording) [1.4].

$$v_c(x) = -\beta \cos(kx) e^{-kd} \left[\frac{1 - e^{-k\delta}}{k\delta} \right] \left[\frac{\sin(kg)}{kg/2} \right] \tag{1.3}$$

where β is a proportionality constant, k is the wave number, δ is the medium thickness, d is the magnetic spacing and g is the head gap width. The Wallace spacing loss factor e^{-kd} indicates that the induced voltage $v_c(x)$ decreases exponentially with increasing magnetic spacing d.

1.3 Tape drive

Fig. 1.4 shows a picture of a typical LTO tape drive (GEN 3). The data cartridge contains a supply reel. The tape (+/- 700 m) is wound on the supply reel in the data cartridge and loaded in the tape drive through the data cartridge slot. The tape moves over rollers (rotary) and/or guides (stationary) which create the tape path and guide the tape at the correct wrap angle over the magnetic read/write head before it is wound on the take-up reel. The magnetic read/write head enables the data exchange; data can be written on the tape, or information can be read from the tape.

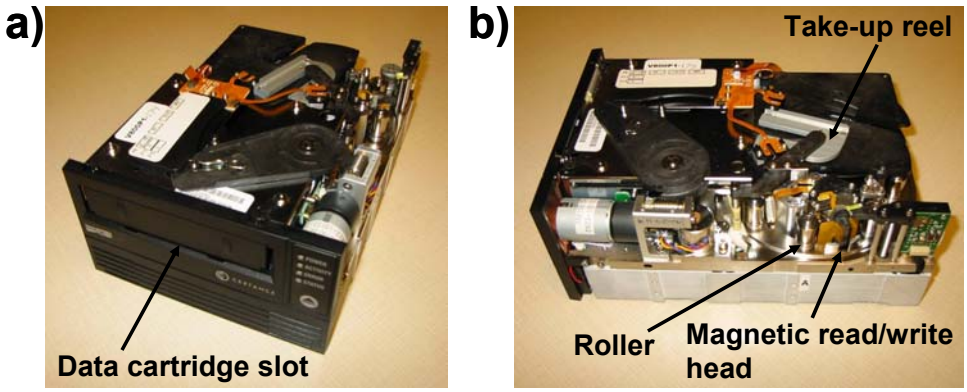

Fig. 1.4: LTO tape drive (GEN 3)

1.4 Tape/head interface and servo loop

1.4.1 Tape/head interface

Fig. 1.5 shows a CAD-model of a typical tape head. The tape is guided over the air bearing surface. The read/write heads are mounted inside the slot in the middle of the

air bearing surface. The tape head is mounted on a voice coil motor (VCM), which is controlled by a servo loop. The VCM enables adjusting the lateral (vertical) position of the read/write heads. Alignment and stiffness of the moving assembly is obtained by means of a leaf spring at the top-side of the tape head.

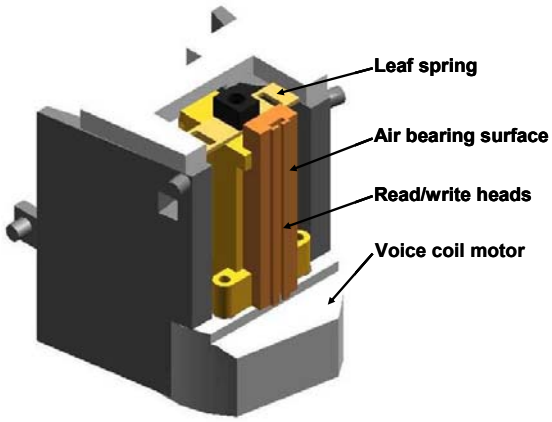

Fig. 1.5: LTO Tape head

Fig. 1.6 a) shows a close-up of the air bearing surface. The slot in which the read/write heads are mounted is clearly visible. The read/write head modules are 8 or 16 channel devices which span approximately one quarter of the tape width at a time. Fig. 1.6 b) shows an eight-channel read/write head module. The eight read/write transducers are enclosed by a servo track reader at both ends. Two read/write head modules are positioned face-to-face in the air bearing slot. This allows reading/writing in both tape directions, i.e., from and towards the supply reel [1.5].

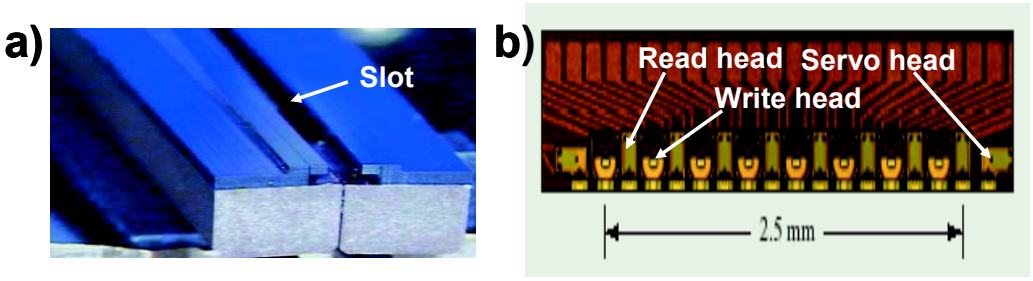

Fig. 1.6: a) Detail of the air bearing surface and b) Read/write head module (source: IBM)

State-of-the-art read heads are of the giant magneto-resistor (GMR) type. GMR heads, like MR heads, consist of a ferromagnetic alloy or a permalloy such as $Ni_{20}Fe_{80}$ [1.6]. The electrical resistivity of the permalloy changes when it is placed in the vicinity of a magnetic field, depending on the strength and direction of the field. The change in electrical resisitivity can then be related to the change in magnetization associated with a previously recorded bit pattern.

The tape/head interface can be modeled as a foil bearing. The behavior of a tape flying over a read/write head has been investigated extensively [1.7 – 1.10]. Lacey and Talke [1.11-1.12] introduced an optimized finite difference algorithm based on the "staggered grid" approach, which yields fast convergence by introducing "artificial stiffness" in the calculation. This method will be explained in further detail in chapter 5.

1.4.2 Servo loop

LTO tape drives use a timing based servo [1.13]. The servo actuator controls the lateral position of the tape head and attempts to follow the lateral displacement of the

tape (see 1.7 Lateral tape motion). The servo controller receives the necessary information about the lateral position of the tape from servo data and positions the read/write head accordingly. The servo information is written on the tape as servo tracks located between regular data tracks. If the tape moves laterally with a frequency higher than the servo actuator bandwidth, the lateral movement cannot be followed by the actuator and read/write errors may occur.

Fig. 1.7 shows a magnification of an LTO tape segment. A number of data tracks and a single servo track are indicated in the figure. A servo track consists of a nearly triangular shaped magnetic servo pattern. A voltage pulse is generated each time a servo mark is detected by the servo head. The time between two pulses can be related to the distance x between two servo marks, if the tape speed is known. With the distance x known, the lateral position of the tape relative to the fixed servo head can be determined, given the shape of the servo pattern. The distance x can thus only be associated with a unique 'cross-track position', i.e., with a unique lateral position of the tape [1.13].

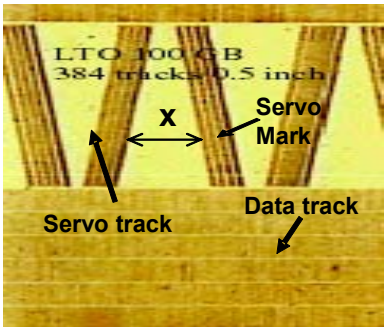

Fig. 1.7: Enlarged view of data and servo track on a tape, made visible by magnetic force microscopy (MFM) (source: IBM)

1.5 Channel and format

Fig 1.8 shows the structure of a 12.7 mm (½ inch) wide LTO tape. An LTO tape consists of four data bands and five servo bands. A separate servo band is positioned adjacent to each side of a data band. The active part of the tape head spans a quarter of the tape, i.e., the width of one data band plus the width of the two servo bands on either side of the data band (+/- 3.175 mm (+/- 0.125 inch)) [1.2].

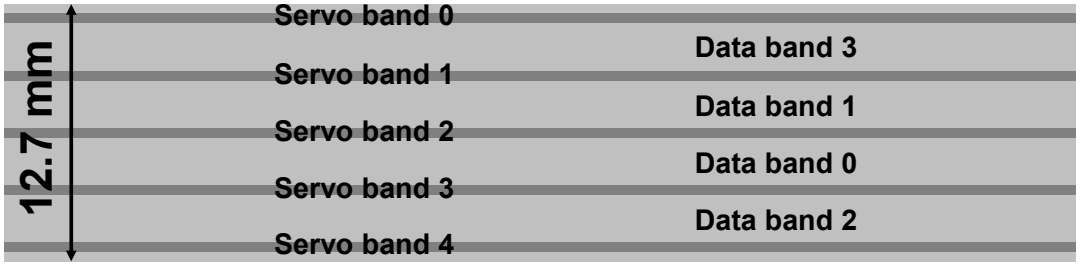

Fig. 1.8: LTO tape structure

Fig. 1.9 schematically shows the structure of a data band and a servo band at large magnification. Each data band consists of eight sub-bands and each sub-band contains a number of tracks (the number is depending on the generation of LTO).

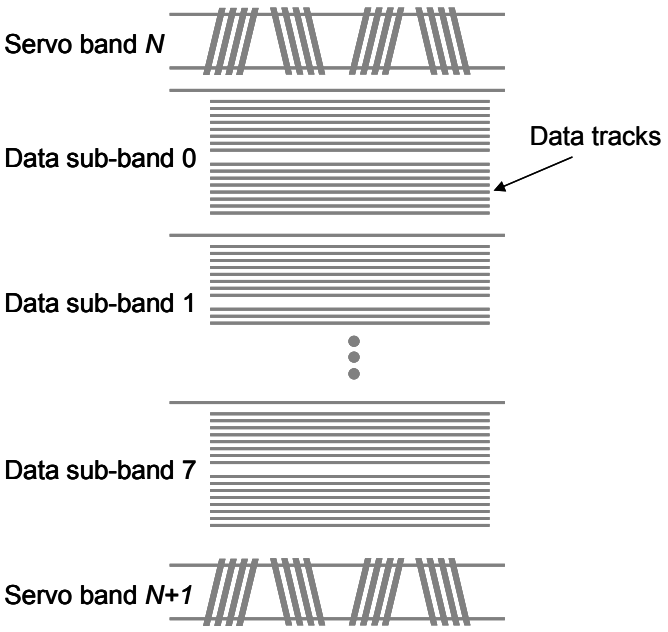

Fig. 1.9: LTO sub data band structure

Each sub-band is written using the so-called "linear serpentine" technique. The "linear serpentine" technique is illustrated in Fig. 1.10 and works as follows: the tape moves back and forth longitudinally while the head is moved up and down laterally, thereby writing multiple distinct tracks in a certain sub-band. Eight different tracks can be written at one time (with an eight-channel read/write head), one track in each data sub-band. Once a data band is full the head is moved to another section of the tape, i.e., to another data band. The numbering of the tracks in Fig. 1.10 shows which tracks are written simultaneously [1.2].

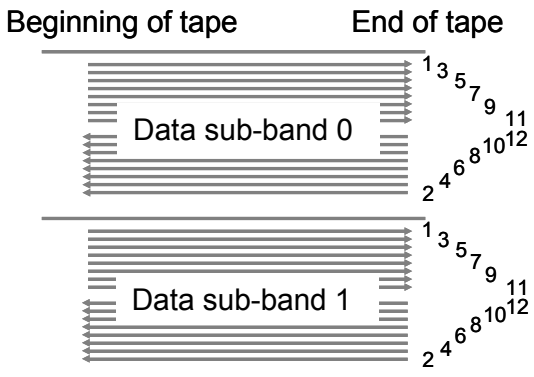

Fig. 1.10: LTO sub data band structure

1.6 Tape media

1.6.1 Recording density

The areal recording density is defined as the product of the linear bit density and the track density. The areal density has increased steadily over time [1.1], as shown in Fig. 1.11. Table 1.1 summarizes key facts for current commercially available LTO products and advanced research demonstrations by IBM [1.1, 1.2, 1.15, 1.16]. The cartridge capacity is given in Gigabytes, track density in tracks per inch, linear bit density in kilobits per inch and areal density in Gigabit per square inch. The tape and track widths are given in millimeters. The state-of-the-art commercially available product is the LTO Gen 3 drive.

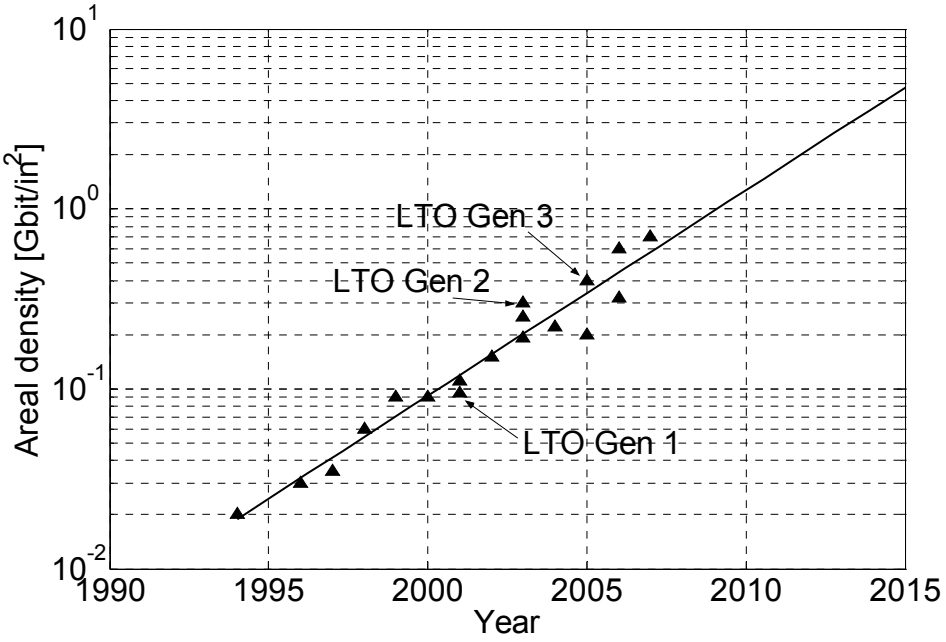

Fig. 1.11: Evolution of the areal density

Table 1.1: Linear Tape Open key numbers

	LTO Gen 1	LTO Gen 2	LTO Gen 3	1 TB demo	8 TB demo
Cartridge capacity [GByte]	100	200	400	1000	8000
Track density [tpi]	768	1024	1408	2432	15000
Linear bit density [kbpi]	124	188	220	313	445
Areal density [Gb/in²]	0.095	0.193	0.308	0.761	6.675
Tape width [mm]	12.7	12.7	12.7	12.7	12.7
Track width [mm]	0.0275	0.0202	0.014	0.0082	0.0015

From Table 1.1, we observe that the increase in areal density between LTO Gen 1 and Gen 2 was mainly obtained by increasing the linear bit density. Between LTO Gen 2 and Gen 3, both an increase in linear bit density and track density contributed to the increase in areal density. It is apparent that significant improvements in the areal density

could be made by increasing the track density even further, as shown by both the 1 Terabyte (TB) and 8 TB demonstrations by IBM Research [1.14, 1.15]. However, increasing the track density is restricted by the tape mechanics as the flexible medium moves through the tape path.

It is important to increase the areal density without reducing the signal to noise ratio (SNR). In other words, the grain size of tape media should be decreased as the recording density is increased. In this case, the number of particles per bit, which determines the SNR, remains constant while the area per bit decreases. A substantial effort has been devoted to achieving a smaller grain size and a higher packing density of the grains for traditional metal particulate (MP) coated media [1.17 - 1.20].

1.6.2 Metal particulate versus metal evaporated tape

LTO tape cartridges use 9 μm thick metal particulate (MP) tape. Fig. 1.12 shows an MP tape sample where the individual layers are visualized. MP tape consists of a polyethylene naftalate (PEN) or polyethylene teraftalate (PET) substrate (+/- 6 μm), coated with a mixture of metal particles and binder material (100 nm), on a non-magnetic underlayer. A back coating minimizes adhesion between the magnetic coating and the backside of the tape, when wound on a reel.

The metal particles are nano-sized particles with a cobalt-iron alloy core with a passivation shell composed of oxidized compounds of the core material [1.21]. The

magnetic coating of MP tape also contains abrasive particles for recording head cleaning.

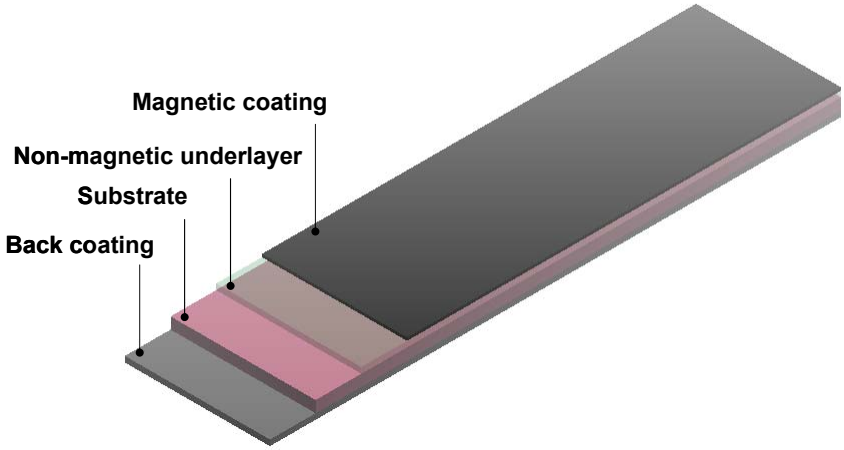

Fig. 1.12: Metal particulate tape

Metal evaporated (ME) tape is manufactured by evaporating cobalt on a polymer (PET) substrate in a vacuum chamber. Cobalt has a higher coercivity than metal particles and is therefore more desirable from an "archival" point of view. An increased coercivity can retain magnetic data for a longer period of time. The substrate as well as the back coating and non-magnetic underlayer are analogous to the MP tape. However, a top-layer such as diamond like carbon (DLC) is deposited on top of the evaporated magnetic layer to increase the durability of the magnetic coating. Fig. 1.13 shows an ME sample where the individual layers are visualized. The tribological characteristics of both MP and ME tape will be explained in detail further in this work.

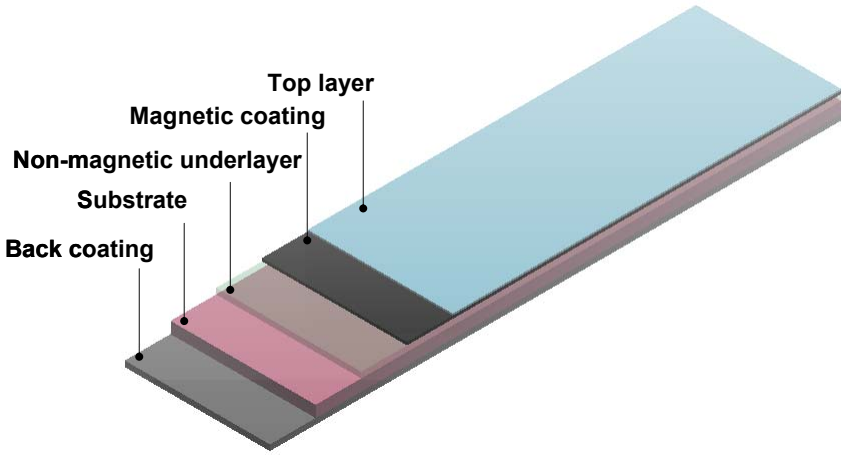

Fig. 1.13: Metal evaporated tape

The use of different magnetic layers, such as sputtered CoCrPt coatings [1.22] and Barium-Ferrite particulate media has also been proposed in the literature [1.23].

1.7 Lateral tape motion

1.7.1 Definition

The track density that can be achieved on a magnetic tape is limited by the dynamics of the moving tape. The time-dependent, in-plane displacement of the magnetic tape, perpendicular to the tape transport direction, is defined as lateral tape motion (LTM) [1.1].

A servo loop controls the lateral position of the magnetic read/write head actuator and compensates for the lateral displacement of the tape, up to a limited bandwidth

[1.15]. The bandwidth of the actuator is mainly limited by the actuator mass and available power [1.1]. LTM with a frequency higher than the bandwidth of the servo actuator (typical cut-off frequency = 0.75-1 kHz) [1.24] is generally referred to as high frequency LTM and can cause track misregistration between the read/write head and a previously written track. Hence, LTM limits the maximum track (recording) density that can be achieved [1.14, 1.24, 1.25]. It is generally observed that a lateral displacement on the order of ten percent of the width of a track causes read/write errors [1.26]. This implies that for the state-of-the-art LTO Gen 3 drive, three times the standard deviation (3σ) of the high frequency LTM must be smaller than 1.4 µm (some sources even report on using 6σ [1.1]). For the case of the 8 TB demo, 3σ of the high frequency LTM must even be smaller than 0.15 µm.

To illustrate the above considerations about the amplitude of LTM with respect to the track width, we have high pass filtered a typical LTM signal from an LTO Gen 1 drive (tape speed = 4 m/s, tape tension = 1 N) using different cut-off frequencies ranging from 0 to 3 kHz. We have summarized the results in Table 1.2.

Table 1.2: Lateral tape motion versus cut-off frequency

Cut-off frequency [kHz]	σ_s [µm]	$3\sigma_s$ [µm]	$6\sigma_s$ [µm]
0	27.87	83.61	167.22
0.5	0.44	1.32	2.64
1.0	0.18	0.54	1.08
1.5	0.1	0.3	0.6
2.0	0.06	0.18	0.36
2.5	0.05	0.15	0.3
3.0	0.04	0.12	0.24

From Table 1.1, we find a track width of 27.5 μm for LTO Gen 1. Hence, 3σ of the LTM must be smaller than 2.75 μm, to avoid track misregistration. Servo actuators for LTO Gen 1 drives typically have a bandwidth of 500 Hz, thus from Table 2 we find that the 3σ value of the LTM, which cannot be followed by the servo actuator (>500 Hz), is equal to 1.32 μm. In this case, it is unlikely that LTM will cause read/write errors, since 1.32 μm < 2.75 μm. Even when using 6σ [1.1], 2.64 μm < 2.75 μm. In the case of the 8 TB demo, we conclude from Table 2 that if the head servo actuator would be able to follow LTM up to 3 kHz, it would be possible to accommodate a 1.5 μm track width, since 3σ of the high frequency LTM is smaller than 0.15 μm (10% of the track width). However, state-of-the-art servo actuators only offer bandwidths up to 1 kHz.

To increase the track density, two approaches could be followed. First, the amplitude of the LTM could be reduced to satisfy the track misregistration requirement, i.e., 3σ of the high frequency LTM amplitude must be smaller than 10% of the track width. Secondly, the bandwidth of the servo actuator could be increased to improve the track-following capability. Higher LTM frequencies typically have smaller amplitude. Thus, by increasing the bandwidth of the actuator, the cut-off frequency will be higher and the amplitude of the high-frequency LTM, which cannot be tracked by the servo actuator, will be smaller (and thus 3σ too). Smaller high-frequency LTM would enable narrower track widths and thus higher track density.

1.7.2 Measurement

A number of different methods to measure the lateral displacement of magnetic tape has been reported in the literature. The most common method to measure LTM is the use of an optical edge probe [1.25, 1.27]. Fig. 1.14 a) illustrates the concept of the optical edge probe. A light beam emitted through light transmitting fibers is deflected 90 degrees by a prism. The path of the light beam is partially obstructed by the tape, before the remaining light is again deflected into the receiving fibers by a second prism. The amount of light "seen" by the receiving fibers is thus a measure for the lateral position of the tape [1.28].

A similar method has been reported using infrared light instead of light in the visible light range [1.29, 1.30]. This method uses an optical switch, which is much cheaper than an optical edge probe. These optical techniques are easily applicable, allow LTM measurements at any position along the tape path and yield repeatable results. Both optical techniques, however, incorporate the imperfections of the tape edge in the measured LTM signal. Factory slit tape edge is not perfectly straight [1.31]. The edge has local imperfections such as cracks and tears, which may grow in time as a result of tape edge wear. Hence, a small part of the measured LTM is due to the imperfectly slit tape edge. However, most imperfections are smaller than the lateral displacement of the tape and therefore the optical methods still yield reliable results.

An alternative to the optical LTM measurement is to use the position error signal (PES) [1.32]. Fig. 1.14 b) illustrates the PES-method. The position of the servo head is indicated by $y_{sh}(t)$, while the position of the servo track is denoted by $y_{st}(t)$. In addition, $y_{edge}(t)$ indicates the position of the tape edge and $y_{\mathrm{var}}(t)$ is the so-called servo track variability, defined as the difference between the servo track position and the tape edge position, $y_{var}(t) = y_{st}(t) - y_{edge}(t)$. The $PES(t)$ is defined as the difference between the servo head position and the servo-track position, $PES(t) = y_{sh}(t) - y_{st}(t)$. The PES yields a reliable measure for the LTM at the read/write head, but can only be determined at the read/write head. However, the LTM derived from the PES incorporates the geometric imperfections (non-straightness) of the servo track. Hence, the LTM measurement is mainly dependent on the "straightness" of the servo track. Using system identification methods, it is possible to separate the effect of servo track variability and the effect of the LTM on the PES [1.32].

Most recently, a method based on the magnetic read-back signal has been proposed [1.26] as illustrated in Fig. 1.14 c). The magnetic read element is smaller than the track width. When the read head is positioned in the middle of the data track, the read-back voltage is maximal. The deviation of the magnetic read head position from the middle of the data track y_m, is a linear function of the read-back voltage (between certain boundaries). Hence, the read-back voltage can be used as a measure for the LTM. This LTM is independent of tape edge quality or the straightness of the servo track, but is now dependent on the straightness of the data track. LTM during data writing cannot be

assumed zero. The LTM while writing the data is on the same order of magnitude as the LTM while reading the data. Thus, the LTM derived from the read-back signal consists of both the contribution of LTM while writing the data and the contribution of LTM while reading the data.

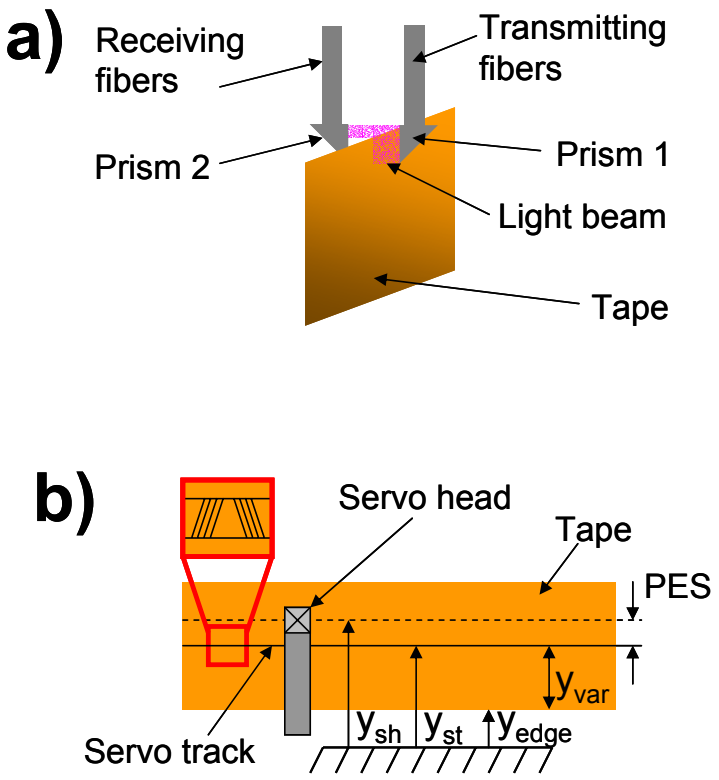

Fig. 1.14: LTM measurement a) fotonic edge sensor, b) PES signal and c) magnetic signal

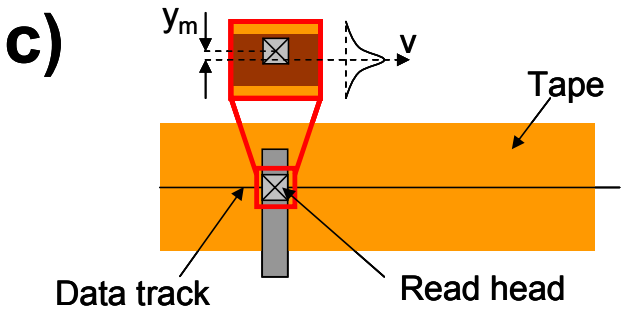

Fig. 1.14 continued: LTM measurement a) fotonic edge sensor, b) PES signal and c) magnetic signal

1.7.3 Sources of LTM

The main sources of lateral tape motion are due to the run-out of tape reels and tape rollers [1.16], tape tension transients due to torque changes in the supply and take-up reel motors [1.14] and contact between the tape edge and a flange (roller or reel) [1.15].

Commercial tape drives use rolling-element bearings. Imperfections and manufacturing tolerances cause run-out of the bearings. The run-out consists of repeatable run-out occurring at the frequency of rotation and a non-repeatable run-out [1.24]. The sum of both repeatable and non-repeatable run-out components is defined as the total indicated run-out (TIR). Taylor and Talke [1.30] measured the axial run-out of a roller (TIR) and the LTM close to that roller and found a maximum correlation of 81% between both signals, when band pass filtered between 0.4 and 1.7 kHz. After applying a perfluoropolyether lubricant on the roller surface, the maximum correlation between the axial roller run-out and the LTM decreased to 41%. It was also found that in the case of a smooth roller, the correlation coefficient between the LTM and the axial

run-out measurement was lower than in the case of a grooved roller. Grooved rollers eliminate the air bearing (hydrodynamic lubrication) and therefore increase the frictional interaction between the roller and the tape. These experimental results suggest that frictional coupling between tape and roller in combination with axial roller run-out, significantly contributes to LTM. The two other main LTM sources, as mentioned above, will be discussed in detail in chapter 2 and 3 of this dissertation.

1.8 Dissertation outline

This dissertation consists of three parts, each of which containing two chapters. The first part (chapters 2 and 3) of the dissertation deals in detail with two primary sources of lateral tape motion, namely tape tension transients and tape edge contact. The second part (chapters 4 and 5) investigates the fundamentals of the dynamics of the magnetic tape and the frictional interaction of the tape with a cylindrical guide. The final part (chapters 6 and 7) presents improvements, which can be implemented to reduce lateral tape motion in tape drives and lead to an increase in track density.

Chapter 2 presents the design of a non-contact, optical tension sensor. The sensor was then used to investigate the effect of tape tension transients on LTM. Chapter 3 shows how LTM is affected by tape edge contact. A novel approach based on acoustic emission was used to measure impacts between a moving tape and the flange of a tape guide. After calibrating the acoustic emission signal, the impact force between tape and flange was determined. The influence of tape drive operating conditions as well as

design parameters on tape edge contact was studied. A one dimensional model was developed to predict the magnitude of tape/flange impact. The model fits the experimental data well.

Since a tape translates over tape drive components (such as cylindrical guides), it is crucial to understand the dynamics of the tape as well as the frictional interaction between a polymeric tape and a metal guide. Chapter 4 is concerned with the mechanics of lateral motion of an axially moving tape on a cylindrical guide surface. The effects of lateral bending stiffness and friction force are studied and the attenuation of lateral tape motion as a function of the guide radius and friction coefficient is determined. Chapter 5 introduces a model for the friction coefficient between a tape and a guide. The model allows the investigation of the effect of various parameters such as sliding speed, tape tension, surface roughness, material properties and guide and tape geometry on the magnetic tape/guide friction coefficient. The friction coefficient between a guide and a tape sample is also determined from experimental measurements as a function of these various parameters.

Chapter 6 presents a novel approach to tape guide design by using micro-textured guides. The micro-texture enhances the formation of an air bearing and hence reduces the friction coefficient and the transition speed between boundary lubrication and hydrodynamic lubrication. Chapter 7 analyses the design of a dual-stage actuator tape head with an increased bandwidth compared to state-of-the-art tape heads. A prototype was built and a dual-stage servo controller was developed.

1.9 References

[1.1] Information Storage Industry Consortium, 2005, Magnetic Tape Storage Roadmap

[1.2] Jacquette GA, 2003, LTO: A Better Format for Mid-Range Tape, IBM J. Res. & Dev., Vol. 47(4), pp. 429 - 444

[1.3] Bertram HN, 1994, Theory of Magnetic Recording, Cambridge University Press, New York

[1.4] Wallace RL, 1951, The Reproduction of Magnetically Recorded Signals, Bell Systems Tech. Journals, Vol. 30, pp. 1145 - 1173

[1.5] Biskeborn RG, Eaton JH, 2003, Hard-Disk-Drive Technology Flat Heads For Linear Tape Recording, IBM J. Res. & Dev., Vol. 47(4), pp. 385 - 400

[1.6] Bhushan B, 1996, Tribology and Mechanics of Magnetic Storage Devices, Springer Verlag, New York

[1.7] Stahl KJ, White JW, Deckert KL, 1974, Dynamic Response of Self-Acting Foil Bearings, IBM J. Res. & Dev., pp. 513 - 520

[1.8] Granzow GD, Lebeck AD, 1984, An Improved One-Dimensional Foil Bearing Solution, Trib. and Mech. of Mag. Storage Devices, STLE-SP16, Vol.1, pp. 54 - 58

[1.9] Heinrich J, Wadwa S, 1986, Analysis of Self-Acting Foil Bearings: A Finite Element Approach, Trib. and Mech. of Mag. Storage Devices, STLE-SP21, Vol.3, pp. 152 - 159

[1.10] Adams GG, 1989, A Novel Approach to the Foil Bearing Problem, Trib. and Mech. of Mag. Storage Devices, STLE-SP26, Vol.6, pp. 1 - 7

[1.11] Lacey C, Talke FE, 1990, A Tightly Coupled Numerical Foil Bearing Solution, IEEE T. Mag., Vol. 26(6), pp. 3039 - 3043

[1.12] Lacey C, Talke FE, 1992, Measurement and Simulation of Partial Contact at the Head/Tape Interface, J. Trib. T. ASME, Vol. 114, pp. 646 – 652

[1.13] Barrett RC, Klaassen EH, Albrecht TR, 1998, Timing-Based Track-Following Servo for Linear Tape Systems, IEEE T. Mag., Vol. 34(4), pp. 1872 - 1877

[1.14] Childers ER, Imaino W, Eaton JH, Jaquette GA, Koeppe PV, Hellman DJ, 2003, Six Orders of Magnitude in Linear Tape Technology: The One-Terabyte Project, IBM J. Res. & Dev., Vol. 47(4), pp. 471 - 482

[1.15] IBM Research Press Resources, 2006, IBM Researchers Set World Record in Magnetic Tape Data Density, http://domino.watson.ibm.com

[1.16] Dee RH, 2006, Magnetic Tape: The Challenge of Reaching Hard Disk Drive Data Densities on Flexible Media, MRS Bulletin, Vol. 31, pp. 404 - 408

[1.17] Sharrock MP, 2000, Recent Advances in Metal Particulate Recording Media: Toward the Ultimate Particle, IEEE T. Mag., Vol. 36(5), pp. 2420 - 2425

[1.18] Sekiguchi N, Kawakami K, Ozue T, Yamaga M, Onodera S, 2005, Examination of Newly Developed Metal Particle Media for >3 Gb/in² Recording in GMR-Based Tape Systems, IEEE T. Mag., Vol. 41(10), pp. 3235 - 3237

[1.19] Inaba H, Ejiri K, Masaki K, Kitahara T, 1998, Development of an Advanced Metal Particulate Tape, IEEE T. Mag., Vol. 34(4), pp. 1666 - 1668

[1.20] Richter HJ, Veitch RJ, 1996, MP Tape for High Density Digital Recording, J. Mag. Mag. Mat., Vol. 155, pp. 80 - 82

[1.21] Personal communication

[1.22] Lee HS, Laughlin DE, Bain JA, 2003, Recording Properties of CoCrPt Tape Media Sputter-Deposited at Room Temperature on Polymeric Substrates, J. Appl. Phys., Vol. 93(10), pp. 7783 - 7785

[1.23] Nagata T, Harasawa T, Oyanagi M, Abe N, Saito S, 2006, A Recording Density Study of Advanced Barium-Ferrite Particulate Tape, IEEE T. Mag., Vol. 42(10), pp. 2312 - 2314

[1.24] Richards DB, Sharrock MP, 1998, Key Issues in the Design of Magnetic Tape for Linear Systems of High Track Density, IEEE T. Mag., Vol. 34(4), pp. 1878 - 1882

[1.25] Taylor RJ, Strahle P, Stahl J, Talke FE, 2000, Measurement of Cross-Track Motion of Magnetic Tapes, J. Info. Storage Proc. Syst., Vol. 2, pp. 255 - 261

[1.26] Alfano AD, Bhushan B, 2006, New Technique for Monitoring Lateral Tape Motion Using a Magnetic Signal, Microsyst. Technol., Vol. 12, pp. 565 - 570

[1.27] Goldade AV, Bhushan B, 2003, Measurement and Origin of Edge Damage in a Linear Tape Drive, Tribol. Lett., Vol. 14, pp. 167 - 180

[1.28] MTI-2000 Fotonic Sensor Instruction Manual, 2000, Mechanical Technology Inc. (Latham, NY, USA)

[1.29] Raeymaekers B, Taylor RJ, Talke FE, 2006, Non-Contact Tape Tension Measurement and Correlation of Lateral Tape Motion and Tape Tension Transients, Microsyst. Technol., Vol. 12(4), pp. 814 - 821

[1.30] Taylor RJ, Talke FE, 2005, Investigation of Roller Interactions with Flexible Tape Medium, Tribol. Int., Vol. 38, pp. 599 - 605

[1.31] Goldade AV, Bhushan B, 2004, Tape Edge Study in a Linear Tape Drive with Single Flanged Guides, J. Mag. Mag. Mat., Vol 271, pp. 409 - 430

[1.32] Jose J, Taylor RJ, de Callafon RA, Talke FE, 2005, Characterization of Lateral Tape Motion and Disturbances in the Servo Position Error Signal of a Linear Tape Drive, Tribol. Int., Vol. 38, pp. 625 - 632

2. Non-contact tape tension measurement and correlation of lateral tape motion and tape tension transients

2.1 Introduction

Lateral Tape Motion (LTM) is measured using optical tape edge sensors [2.1]. High frequency lateral tape motion is a key problem in tape technology, since it limits the maximum achievable track density in a tape drive [2.2]. Tape tension transients are one of the most important sources of high frequency LTM [2.3-2.5]. Fig. 2.1 a) shows a typical unfiltered LTM signal while Fig. 2.1 b) shows the same signal after high pass filtering at 500 Hz. We observe that the unfiltered signal shows a lateral displacement on the order of 60 μm while the high frequency components are on the order of 2 μm.

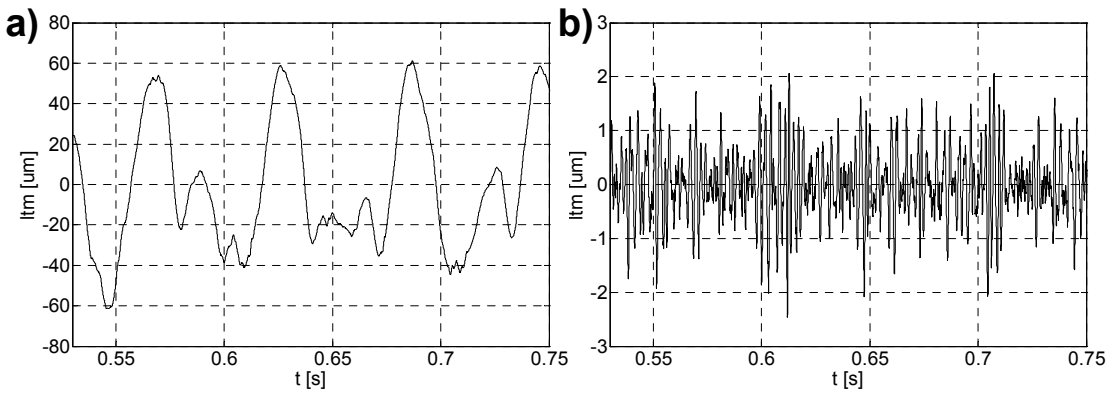

Fig. 2.1: Lateral Tape Motion versus time

The effect of tape tension transients on high frequency LTM is currently not well understood. It is apparent, however, that tape tension transients lead to transverse motion of the tape in the wide span between supports due to tape curvature [2.6]. Tape tension in a tape drive is generally measured using pressure transducers [2.7]. However, the bandwidth of these sensors is limited to below 100 Hz and improved tension sensing devices are necessary to investigate the relationship between tension changes and high frequency LTM.

Smith and Sievers [2.8] attempted to measure tape tension changes using a commercial flutter meter and the digital read-back signal of a tape drive. The difference between write and read-back signal with respect to 'bit distance', was used to provide information regarding tape tension. The Smith-Sievers method is illustrated in Fig. 2.2 a). The "bit distance" when writing is indicated by a length x, while the "bit distance" when reading is denoted by a length $x+dx$. The difference in length dx is due to a change in tape tension. This approach is correct, only if the velocity of the tape drive is constant or if velocity changes in time during writing and reading are the same. Boyle and Bhushan [2.9] investigated lateral tape motion as a result of an impact on the tape. Tape tension, however, was not measured. Imaino developed a non-contact method to measure tension in a magnetic tape [2.10]. The tension in the tape is created by a known weight of mass m. A pulsed laser was used to photo-acoustically generate an anti-symmetric Lamb wave within the tensioned tape sample, as shown in Fig. 2.2 b). The out-of-plane motion created by this wave was detected with a Laser Doppler Velocimeter (LDV). The "time of flight" of the acoustic wave and the known separation

d, between the pulsed laser and the LDV yield the propagation velocity of the wave. The Rayleigh Lamb wave equation [2.11] in combination with the experimentally measured wave propagation speed yields the tape tension when the flexural stiffness of the tape is known.

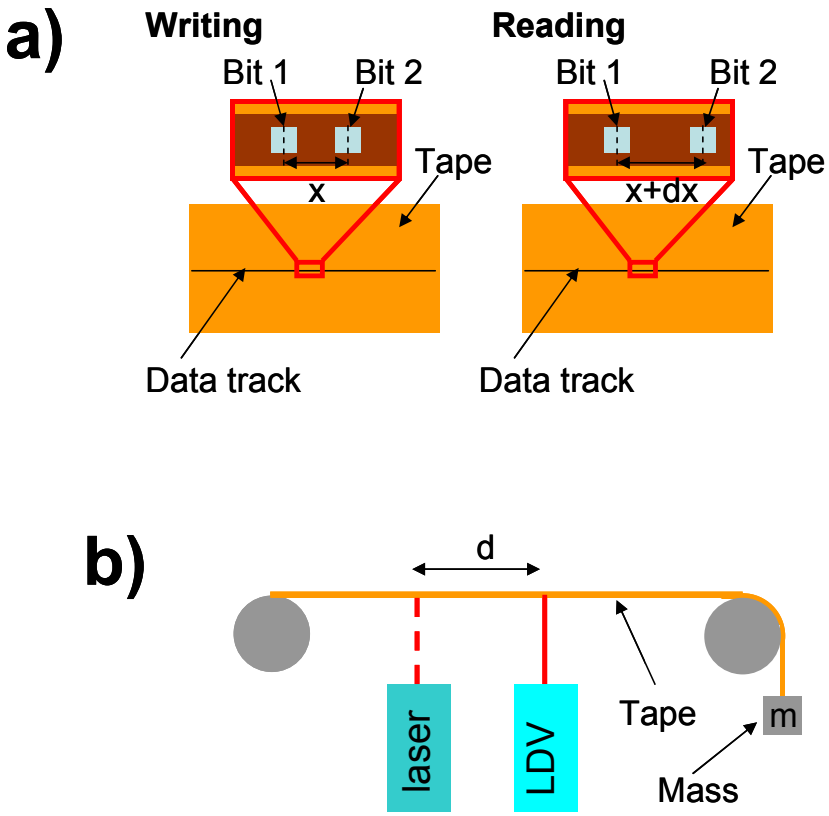

Fig. 2.2: Non-contact tape tension measurement a) Smith and Sievers and b) Imaino

In this chapter, an optical non-contact high bandwidth tension sensor for magnetic tape is developed and the correlation between lateral tape motion (LTM) and tape

tension transients is investigated. The use of an optical light reflection method similar to the one described here was first proposed by Jim Eaton [2.12].

2.2 Tension sensor

The concept of a non-contact tension measurement uses the following approach. A tape moves over a solid surface that contains an edge. The solid edge can be created by adding an edge element in the tape path or by using the side of the magnetic head as a solid edge. The latter is shown in Fig. 2.3. A laserbeam is directed at the magnetic tape surface as it moves over the edge. The light reflected from the tape is captured by a photo cell. Since the radius of curvature of the tape over the edge of the solid surface decreases with increasing tape tension, the divergence of the reflected light bundle increases with increasing tension, i.e., the amount of light seen by the photo cell is a function of the tape tension. Thus, measurement of the change of light reflected from a tape surface can be used as a measure of the tension change in the tape.

The principle of the optical tension measurement is illustrated in Fig. 2.3 a) and b). At low tension T_1 (Fig. 2.3 a)), the reflected light beam diverges less than at high tension T_2 (Fig. 2.3 b)). The method is independent of the 'sharpness' of the edge and the type of tape.

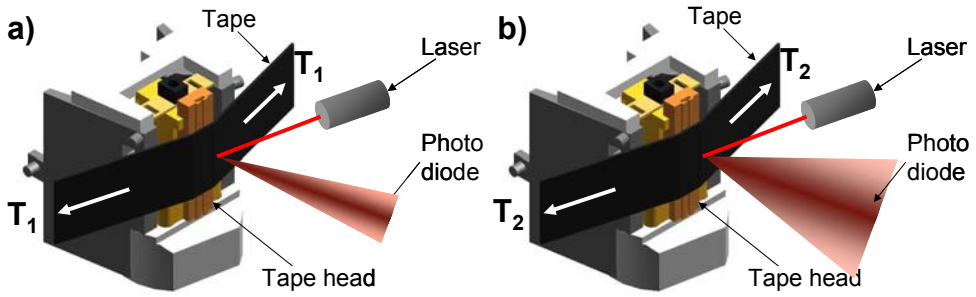

Fig. 2.3 a) Divergence of the light beam as a result of a) tension T_1 and b) tension T_2

A typical calibration curve of the photo cell voltage versus the tape tension is shown in Fig. 2.4. The entire tension deviation range encountered in a tape drive is contained within the linear range of calibration. The sensor has to be calibrated for each type of tape due to different reflectivity of each tape and for each magnetic read/write head due to variation in the head contour.

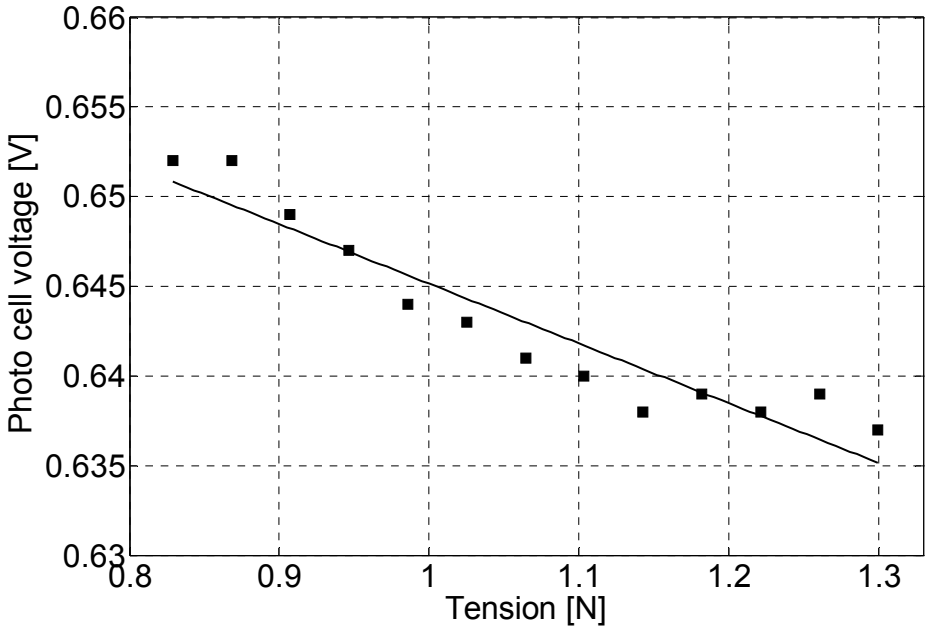

Fig. 2.4 Typical calibration curve

2.3 “Artificial” disturbance

To investigate the correlation between dynamic tension changes and LTM changes, the following approach was used. An eccentric tape pack was first created by inserting a thin rod into the tape pack during winding. Using this eccentric pack, large tension disturbances were created in the tape at the reel rotation frequency. Fig. 2.5 shows a schematic of the test set-up used. The tape path was configured with an actual tape head to simulate a commercial tape drive. A smooth roller was positioned before and after the tape head to insure a proper wrap angle. An LTM edge sensor [2.1] was positioned in close proximity of the head to measure the lateral displacement of the tape. The tension sensor was directed at the edge of the head. Tape speed was set at 4 m/s and a nominal tape tension of 1 N was used. The “artificial” disturbance created a tension disturbance of about 0.5 N.

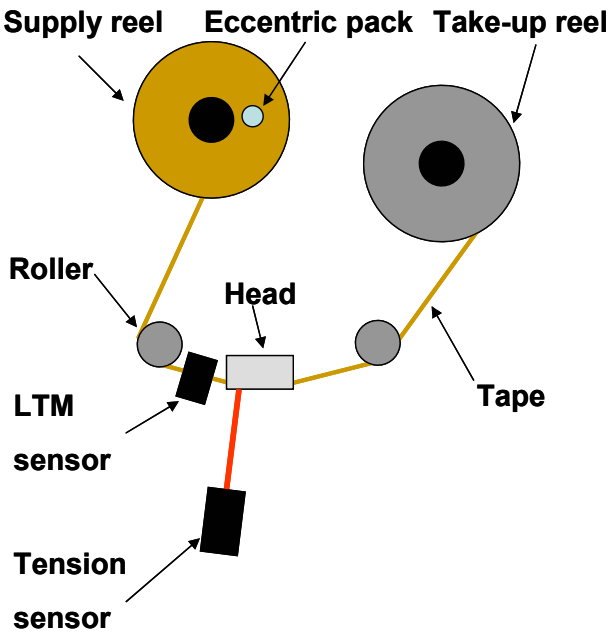

Fig. 2.5 Schematic of test-set up

2.4 Results

Fig 2.6 a) shows the LTM signal and the tension changes versus time. A magnification of a short section of Fig. 2.6 a) is depicted in Fig. 2.6 b), and in Fig. 2.6 c) the cross-correlation coefficient r_{corr} between tension change and LTM signal is calculated as

$$r_{corr}[n] = \frac{1}{2N+1} \sum_{m=-N}^{N} f_1[m+n] f_2[n] \qquad (2.1)$$

where f_1 and f_2 are the two signals to be correlated and the data set is of length $2N$. We observe that the maximum correlation between tension change and LTM is approximately 40 %.

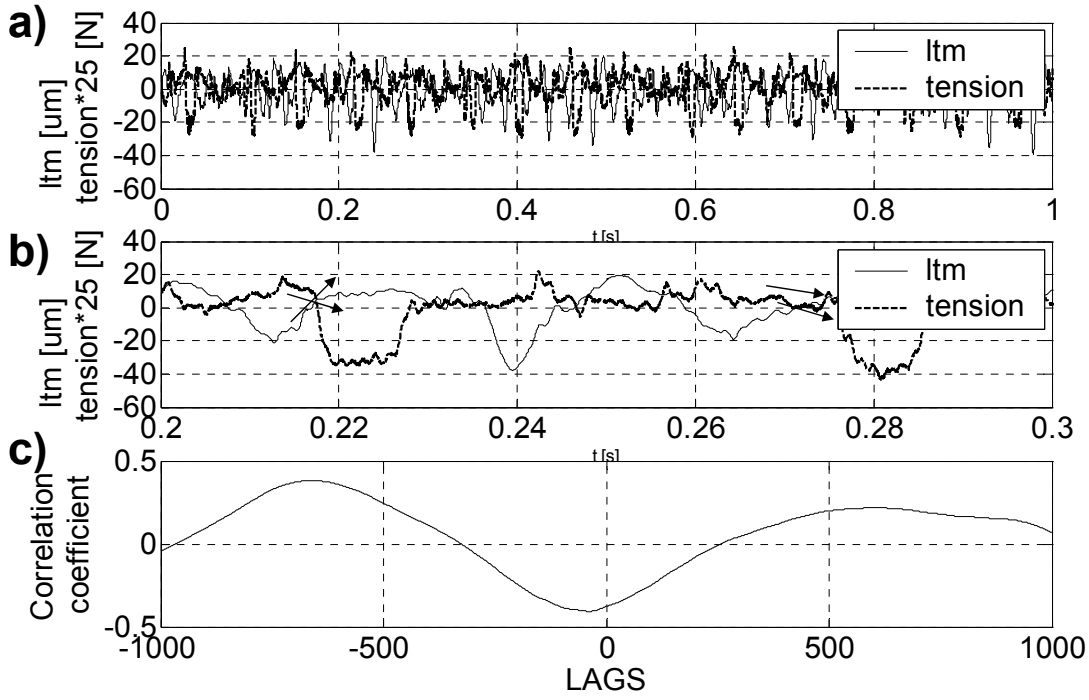

Fig. 2.6 LTM and tension, artificial disturbance

From the curves shown in Fig. 2.6 b), we observe that an increase in tape tension always causes a change in LTM. The direction of this change is sometimes towards larger LTM values and sometimes towards smaller LTM values. The same behavior is observed if the tape tension is decreased, i.e., a tension decrease always causes a change in LTM, but this change can be towards larger or smaller LTM values as pointed out by the arrows in Fig. 2.6 b). Hence, four different cases must be taken into account when considering the correlation between tension changes and LTM changes:

1. Tension increases, tape moves down
2. Tension increases, tape moves up
3. Tension decreases, tape moves down

4. Tension decreases, tape moves up

From the above considerations, it is apparent that the correlation between the absolute values of the tension and LTM signal must be investigated rather than the correlation of the actual signals. The use of absolute values is justified since we are interested in the relationship between tension transients and LTM changes regardless of their direction. In other words, we are primarily interested in investigating whether tension changes induce LTM changes; the direction of these changes is immaterial.

Fig. 2.7 shows the correlation between the absolute values of both the tension changes and the LTM changes for the data shown in Fig. 2.6. We observe a direct relationship between tension change and LTM. This is further supported by the increase of the maximum correlation coefficient between the two signals (63 %), which is higher than the correlation coefficient between the actual signals (40 %). Thus, we conclude that tension changes cause LTM changes.

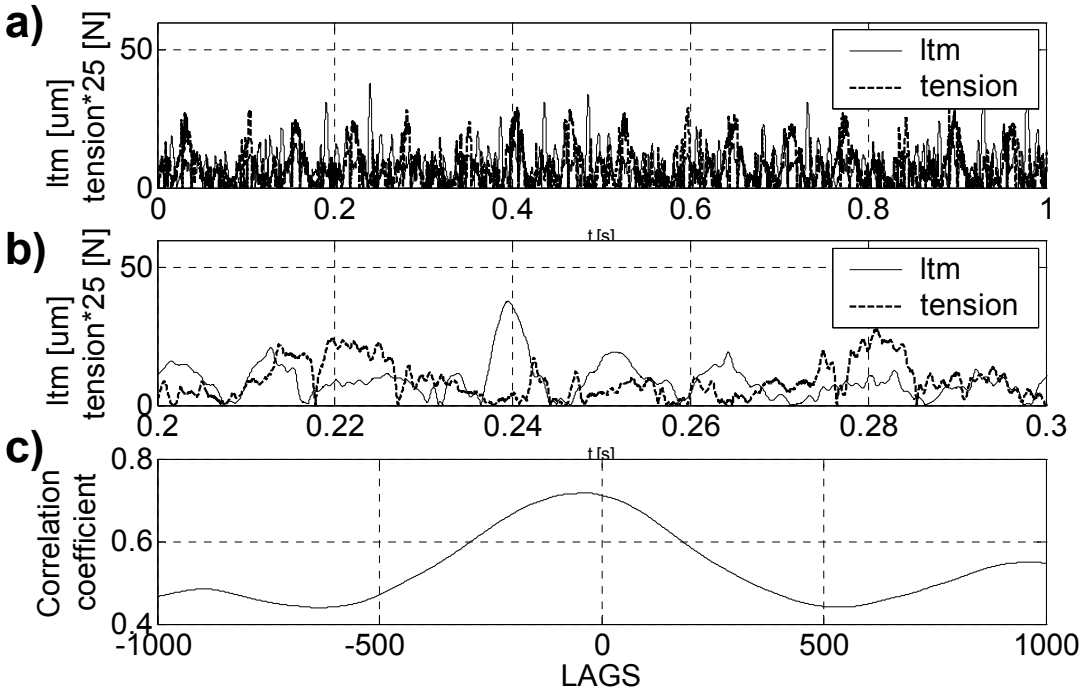

Fig. 2.7 Artificial disturbance, absolute values

2.5 Natural disturbance

The "artificial" disturbance was used to amplify the effect of tension transients in order to get a first indication of the interaction between LTM changes and tension transients. In a commercial tape drive, however, the tension disturbances are much smaller than those created with the eccentric pack. In order to see the effect of small tension transients, we used the same test set-up as displayed in Fig. 2.5 but now with a regular tape pack, without eccentricity, and thus without the large tension disturbance. Fig. 2.8 and Fig. 2.9 show the results from this test.

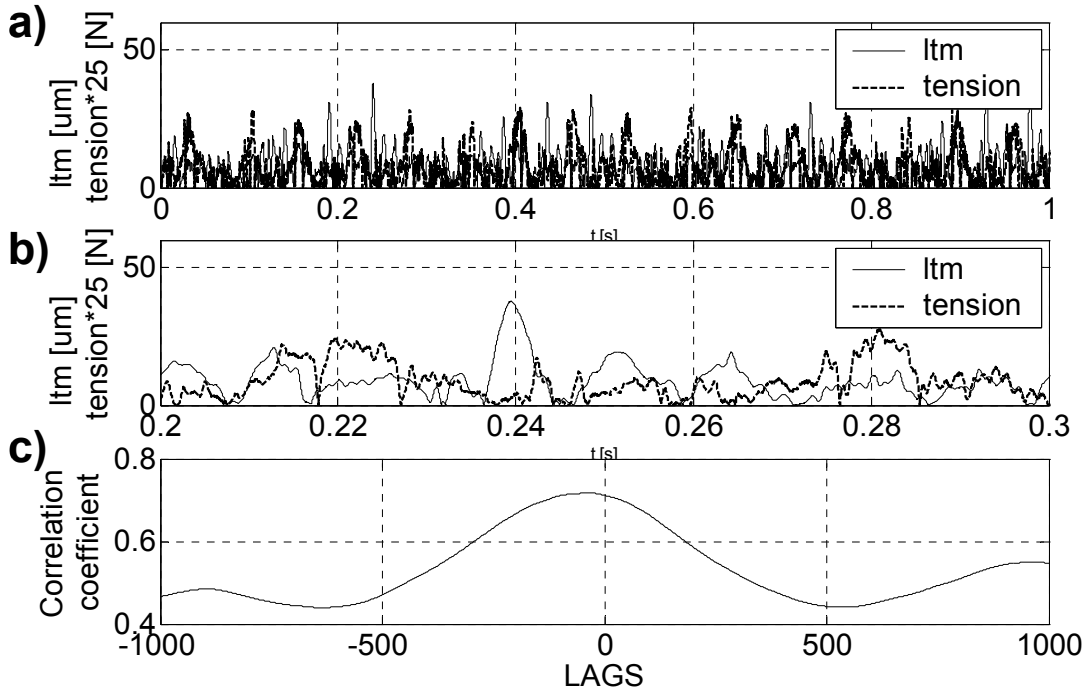

Fig. 2.8 Tension and LTM, natural disturbance

In Fig 2.8 a), the LTM signal and the tension changes are shown. A magnification of a short section of Fig. 2.8 a) is depicted in Fig. 2.8 b). In Fig. 2.8 c) the correlation coefficient between tension changes and the LTM signal is plotted. We observe that the maximum correlation between the tension change signal and LTM is now only 30 %, significantly smaller than with the artificial disturbance previously investigated.

Fig. 2.9 shows the correlation between the absolute values of both the tension change signal and the LTM change signal for the data shown in Fig. 2.7. We again observe a direct relationship between the tension change and the LTM. The maximum correlation between the two signals is now 67 %, which is on the same order of

magnitude than with the artificial disturbance. Thus, the results support our earlier conclusion that tension changes cause LTM changes.

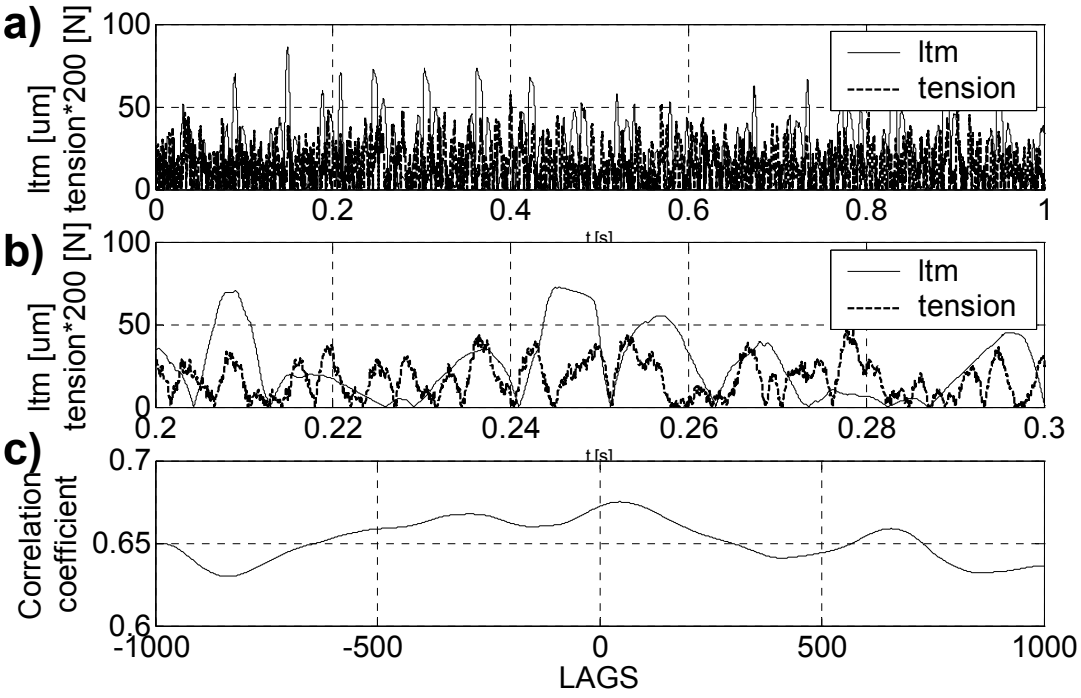

Fig. 2.9 Natural disturbance, absolute values

2.6 Dependence of LTM on tension transient frequency

In order to study the frequency dependency of the correlation between lateral tape motion and tape tension transients, frequency bands of 400 Hz were defined and the data was band pass filtered between these bands. The maximum correlation coefficient between tension changes and LTM changes was calculated for each frequency band and plotted for both the case of an artificial disturbance and the case of a natural disturbance (Fig. 2.10 and Fig. 2.11).

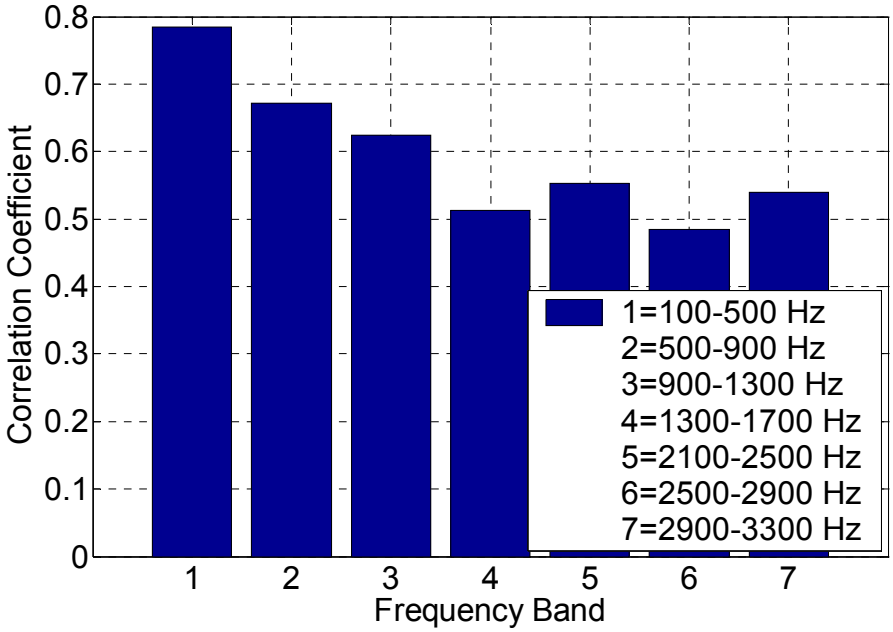

Fig. 2.10 Frequency study with an artificial disturbance

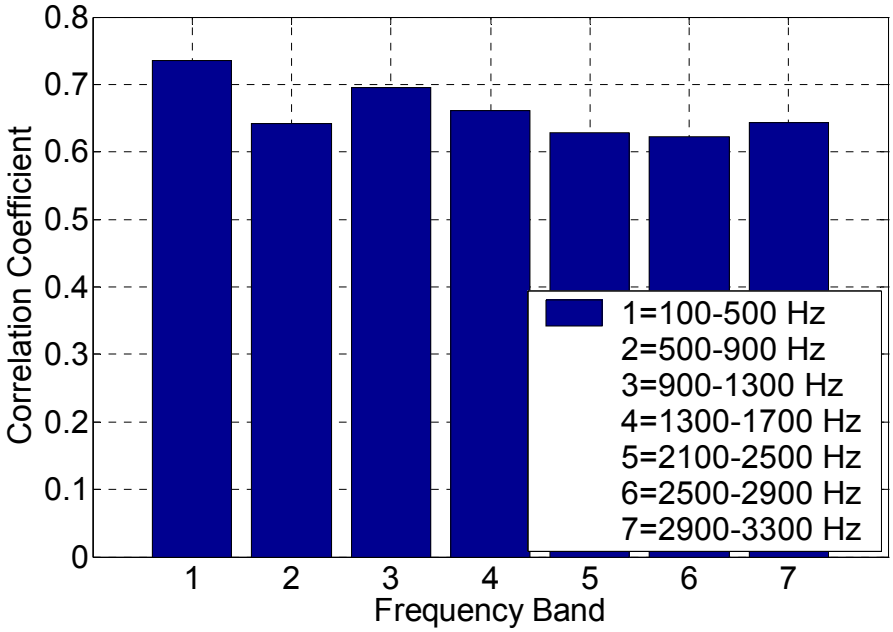

Fig. 2.11 Frequency study with a natural disturbance

We observe from Fig. 2.10 and Fig. 2.11 that the maximum correlation between tension changes and LTM changes decreases with increasing frequency. This trend is likely related to the effect of tape inertia: as the frequencies of tension changes increase, the tape should react faster to those changes. However, the reaction of the tape is limited by its inertia, and thus, the correlation between tension changes and LTM changes as a function of frequency decreases.

2.7 Discussion

The reason why tension changes cause LTM changes seems to be related to the straightness of the tape. If one edge of a tape is shorter than the other, the tape is curved [2.6]. Curvature can be characterized by the radius of curvature, denoted as R in Fig.

2.12. In the tape industry, tape curvature is often referred to as the deviation of tape from straightness and is defined as the maximum deviation h_R over a unit length (generally taken to be one meter of tape length [2.6], as shown in Fig. 2.12).

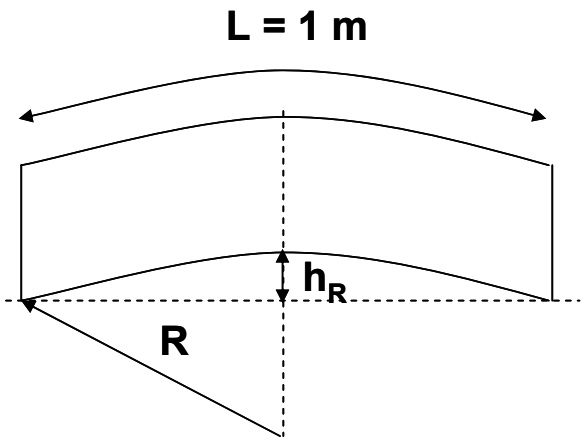

Fig. 2.12: Tape curvature

Hu et al. [2.7] examined the case of a curved tape segment and noted that a tension gradient will develop across the tape width as a result of uneven stretching. Bhushan [2.6] concluded that uneven tension across the tape width can cause tape vibrations over the guide bearings. Our experimental results showed that a correlation exists between tape tension transients and LTM, although no prediction could be made about the direction of the motion resulting from a tension transient. Therefore, it is interesting to characterize the direction of the tape motion with respect to tape curvature and to determine the stress distribution across the tape width.

Fig. 2.13 shows the four cases that influence the correlation between tension transients and LTM. Fig. 2.13 a) shows a positive curvature while Fig 2.13 b) shows a negative curvature. Both the effects of tension increase and decrease are illustrated. If tension increases for a positive curvature, the tape straightens out. This causes the tape to move upwards. If the tension decreases the opposite is true, i.e., the tape moves downwards. If tension increases for a negative curvature the tape will straighten out, causing a downward lateral tape displacement. A tension decrease will cause the tape to move upwards.

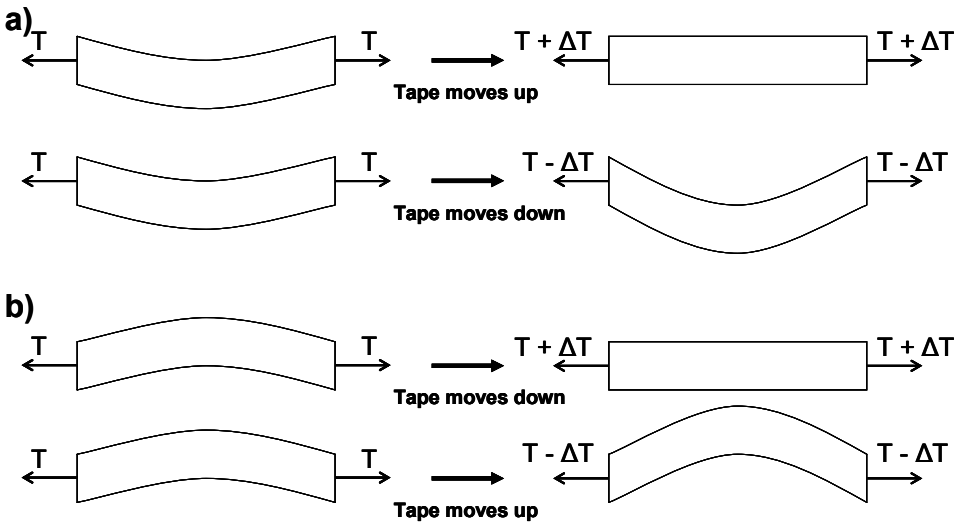

Fig. 2.13: Tape motion as a result of tension transients

By applying tension at both ends of the tape segment, the curved tape is pulled straight. The tension in the tape, however, will not be uniform but characterized by a gradient along the cross-track direction. We can model the tape as a static beam, which is depicted in Fig. 2.14, representing a tape segment.

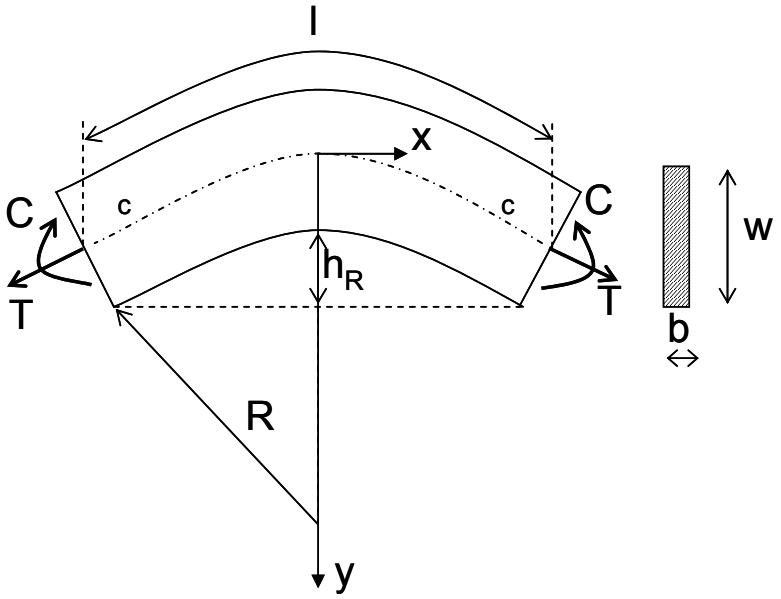

Fig. 2.14: Tape segment

The radius of curvature R is defined as

$$R = \frac{l^2}{8h_R} - \frac{h_R}{6} \tag{2.2}$$

where h_R denotes the absolute curvature of the tape segment with length l [2.13]. Since h_R is much smaller than R ($\frac{R}{h_R} >> 10$), we can assume a linear stress distribution [2.14]. The resulting stress distribution in the tape is shown in Fig. 2.15 and consists of two parts; a constant part due to the nominal tension T applied by the tape drive on the tape and a linear part due to the straightening of the curved tape.

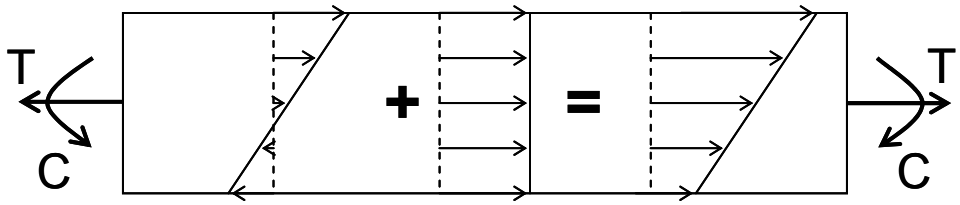

Fig. 2.15: Non-uniform stress distribution

The resulting stress distribution in the tape can hence be written as

$$\sigma_x = \frac{Cy}{EI} + \frac{T}{A} \text{ [2.13]}, \tag{2.3}$$

where $A = b \times w$, the cross-sectional area of the tape and y is the vertical coordinate, with $y = 0$ defined as the center line (*cc*) of the tape. $I = \frac{bw^3}{12}$ is the area moment of the tape cross section. The Young's modulus E is on the order of 9 GPa [2.15]. The bending moment C can be calculated as follows.

$$C = \int_{-\frac{w}{2}}^{\frac{w}{2}} \sigma_x y dA \tag{2.4}$$

$$C = 2\int_{0}^{\frac{w}{2}} \frac{T}{A} b h_R dy \tag{2.5}$$

where $\sigma_x = \frac{T}{A}$ and $y = h_R$ if we assume the curvature to be constant in the lateral direction. Solving (2.5) and substituting the result in (2.3) finally yields the resulting stress distribution as a function of y:

$$\sigma_x = \frac{T h_R y}{EI} + \frac{T}{A} \tag{2.6}$$

Once the curvature of the tape is known along the length of the tape (h_R), the direction of the lateral tape displacement (direction of LTM) can be obtained from Fig. 13. The resulting stress distribution can be calculated from (2.6).

As new tape systems are developed, thinner tapes would allow an increase in the tape windings per cartridge, and therefore a greater capacity per cartridge. However, thinner tapes require increased attention to the stress distribution and the inherent parameters governing the bending stiffness and system tension considerations. If the same nominal tension T would be applied to thinner tape, the internal stresses would increase. The second factor in eq. (2.6) would increase because the cross-sectional area A becomes smaller. Additionally, since I will decrease, the bending stiffness EI will decrease and the first factor in eq. (2.6) will increase too. Making tape thinner thus

affects both the constant and the linear part of the stress distribution along the tape width. It is thus apparent that tension transients and LTM will become increasingly important in future high performance tape drives.

2.8 Conclusion

A non-contact optical method was implemented to measure tape tension and study the effect of tension changes on lateral tape motion. Based on our experimental results, the following conclusions can be drawn:

1. The measurement of the change in reflected light intensity from a tape surface due to a tension variation is a viable method to study the effect of tension change on LTM.
2. A sound correlation exists between the absolute values of tension change and the lateral tape displacement signal.
3. Tape curvature from the slitting process coupled with tension changes from the drive system causes lateral motion of the tape.

2.9 Acknowledgements

Chapter 2, in part, is a reprint of the material as it appears in “Non-Contact Tape Tension Measurement and Correlation of Lateral Tape Motion and Tape Tension Transients”, Raeymaekers B., Taylor R.J., Talke F.E., Microsystem Technologies, 2006. The dissertation author was the primary investigator and author of this paper.

2.10 References

[2.1] Taylor RJ, Strahle P, Stahl J, Talke FE, 2000, Measurement of Cross-Track Motion of Magnetic Tapes, J. Info. Storage Proc. Syst., Vol. 2, pp. 255 - 261

[2.2] Richards DB, Sharrock MP, 1998, Key Issues in the Design of Magnetic Tapes for Linear Systems of High Track Density, IEEE T. Mag., Vol. 34(4), pp. 1878 - 1882

[2.3] Elrod HG, Eshel A, 1965, Theory of Infinitely Wide Perfectly Flexible Self Acting Foil Bearing, J. Basic Eng. T. ASME, Vol. 87(4), pp. 831 - 835

[2.4] Taylor RJ, Talke FE, 2005, Investigation of Roller Interactions With Flexible Tape Medium, Tribol. Int., Vol. 38, pp. 599 - 605

[2.5] Hansen WS, Bhushan B, 2005, Effects of Operating Speed and Tension and Sources of Lateral Tape Motion in a Linear Tape Drive, J. Magn. Magn. Mater., Vol. 293, pp. 826 - 848

[2.6] Bhushan B, 1992, Mechanics and Reliability of Flexible Magnetic Media, Springer Verlag, New York.

[2.7] Hu PY, Hollman W, 1984, Tension Gradient Measurement of Magnetic Tape, IEEE T. Mag., Vol. 20(5), pp. 921 – 923

[2.8] Smith DP, Sievers JA, 1985, Spatially Coherent Longitudinal Vibrations in Magnetic Tape, Tribol. Mech. Magn. Storage Syst., Vol. 2, pp. 80 – 86

[2.9] Boyle JM, Bhushan B, 2005, Vibration Response due to Lateral Tape Motion and Impulse Force in a Linear Tape Drive, Microsyst. Technol., Vol. 11, pp. 48 - 73

[2.10] Imaino W, 2004, Photoacoustic Determination of Tension in Magnetic Tape, Microsyst. Technol., Vol. 10, pp. 334 - 337

[2.11] Rayleigh JWS, 1894, The Theory of Sound, The Macmillan Company, London

[2.12] Personal communication

[2.13] Bronstein IN, 2004, Handbook of Mathematics, Springer Verlag, Berlin/ Heidelberg

[2.14] Timoshenko S, 1970, Strength of Materials, Van Nostrand Reinhold Company

[2.15] Bhushan B, Tao Z, 2004, Mechanical, Hygroscopic, and Thermal Properties of Metal Particle and Metal Evaporated Tapes and Their Individual Layers, J. Appl. Polymer Sci. Vol. 92, pp. 1319 - 1345

3. Characterization of tape edge contact with acoustic emission

3.1 Introduction

Tape edge contact is one of the primary sources of lateral tape motion (LTM). Researchers in the past have investigated various aspects related to tape edge contact. Lakshmikumaran and Wickert studied edge buckling of imperfectly guided webs and developed a "free sliding" model and an "edge guided" model for web buckling [3.1]. Wang, Taylor and Talke investigated the relationship between LTM and tape edge wear by applying a force on the tape edge using a tapered cantilever spring from a hard disk drive suspension [3.2]. They concluded that tape wear increases with increasing tape edge contact force. Doyle experimentally determined the contact force during the transverse impact of plates using strain gauges. This technique is not applicable, however, when dealing with thin magnetic tape [3.3]. The effect of tape edge contact on edge quality and tape wear has also been studied. Goldade and Bhushan found that tape edge contact can damage the tape edge, creates debris and negatively affects tape guiding [3.4, 3.5]. Bhushan, Hinteregger and Rogers optimized edge guiding mechanisms by decreasing friction and improving thermal conductivity and hence reducing the guiding forces [3.6]. Taylor and Talke examined contact between magnetic tape and a reel and studied the effect of tape edge contact on LTM. They also investigated the cause of the so-called stack-shift phenomenon and its relationship to LTM [3.7]. Little published information exists regarding the magnitude of contact

forces during tape edge/flange contact. Since tape edge wear and LTM are related to the magnitude of the tape edge contact force [3.2, 3.7], this information is desirable for the design of future high performance tape drives. This chapter tries to fill the above gap and focuses on the characterization and quantification of tape edge contact between a tape edge and the flange of a roller by means of acoustic emission (AE) techniques.

3.2 Acoustic emission

On a micro-scale, deformation is characterized by dislocations. The movement of dislocations generates transient elastic stress waves, referred to as acoustic emission (AE) [3.8]. Elastic stress waves propagate from a source as plane or spherical waves. The stress waves are picked up by the AE sensor and converted into a voltage proportional to the magnitude of the AE energy [3.9]. In this investigation, an AE sensor is used as a flange instead of an actual flange on a roller. When the tape makes contact with the flange which is replaced by the sensor, a voltage is generated. This voltage is analyzed and used as an indicator of the type and strength of contact occurring as a function of design parameters of the tape edge/roller flange interface.

The impact force $f_{imp}(t)$ can be calculated from the stress σ in the tape/flange contact area S by

$$f_{imp}(t) = \int_S \sigma dS \tag{3.1}$$

The output voltage $v(t)$ of the AE sensor can be related to the impact force $f_{imp}(t)$ by the convolution

$$v(t) = \int_0^t g_{imp}(t-\tau) f_{imp}(\tau)\, d\tau \tag{3.2}$$

where g is the transfer function and τ is the variable of integration. Calculating the Laplace transform from eq. (3.2) yields

$$V(\omega) = G_{imp}(\omega) * F_{imp}(\omega) \tag{3.3}$$

where $V(\omega)$ is the output voltage, $G(\omega)$ is the transfer function, $F_{imp}(\omega)$ is the impact force and ω represents the frequency. After rearranging eq. (3.3), we obtain

$$F_{imp}(\omega) = \frac{V(\omega)}{G_{imp}(\omega)} \tag{3.4}$$

If $G_{imp}(\omega)$ is known in eq. (3.4), $F_{imp}(\omega)$ can be calculated from $V(\omega)$. In order to find the transfer function $G_{imp}(\omega)$, calibration of the AE sensor is necessary.

3.3 Calibration

To determine the magnitude of the contact force between the tape edge and a flange, the AE sensor was first calibrated by means of the "ball drop method" [3.10]. This method has been used previously for the analysis of slider/disk impacts in hard disk drive research [3.11, 3.12]. Fig. 3.1 illustrates the calibration procedure. A steel ball is dropped from different heights h_d on a load cell which measures the impact force during contact (Fig. 3.1 a)). Next, a steel ball is dropped from different heights h_d on

the AE sensor and the maximum output voltage is measured (Fig 3.1 b)). To insure that the impact of the steel ball occurs at the same position for all experiments, a small tube has been used to guide the ball. Correlating the load cell (force) data and the AE (voltage) data, the relationship between AE voltage and impact force was established (Fig 3.1 c) [3.3]. The ball drop calibration method must be interpreted with care since the impact of a steel ball on an AE transducer results in a different contact situation from that of a tape edge and an AE transducer. Therefore, the ball drop calibration only gives an estimate of the impact force, rather than an exact value. Basic information can be obtained, however, for the characteristics of tape edge contact with the roller flange.

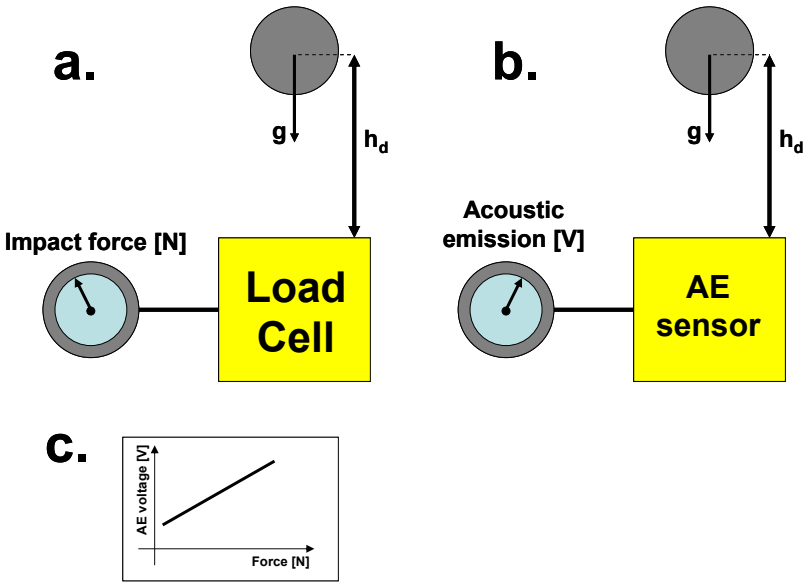

Fig. 3.1: "Ball drop method" calibration procedure

The calibration experiment was repeated five times and the results were averaged over all repetitions. In Fig. 3.2, the averaged value of the AE voltage corresponding to a certain impact force is indicated by a black dot. The upper and lower error bars denote the maximum and minimum value, respectively. The dashed line represents the best linear fit for the calibration curve obtained with the "ball drop method". The analytical equation for the linear calibration curve is shown in the figure. The square of the correlation coefficient, r_{corr}^2, was calculated to be 0.96.

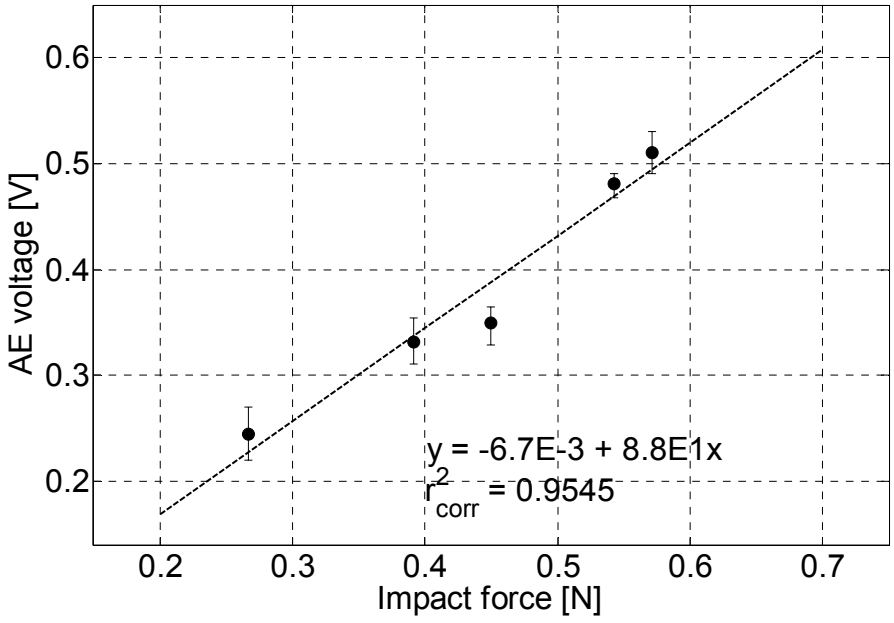

Fig. 3.2: Impact force calibration curve

3.4 Detection of tape/flange contact

Fig. 3.3 shows the experimental set-up used to study contact between a tape and the flange of a roller.

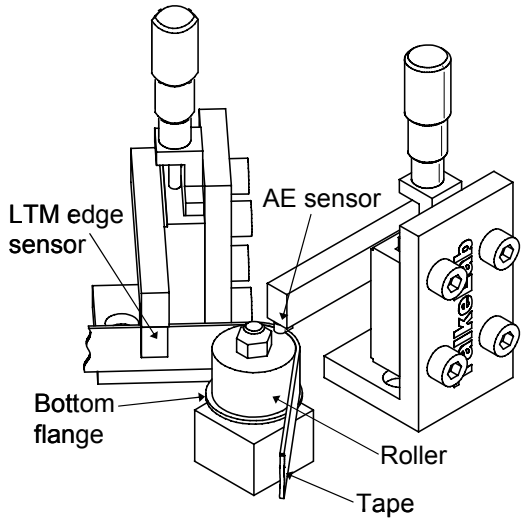

Fig. 3.3: Experimental set-up

Magnetic tape from the supply reel is guided over a smooth roller with a bottom flange, before being wound on the take-up reel. The wrap angle θ was set to be 60 degrees. This tape path is the most fundamental and easiest path to investigate. The AE sensor is positioned above the roller and acts as an "artificial flange". An LTM edge sensor is positioned over the tape to measure LTM.

Fig. 3.4 a) shows the measured values of LTM versus time. Fig. 3.4 b) shows the LTM signal versus time, after high-pass filtering at 1 kHz while Fig. 3.4 c) shows the root mean square (rms) impact force between the tape and the flange, also as a function

of time. The rms impact force is derived from the rms AE voltage and is thus related to the energy content of the AE signal [3.9].

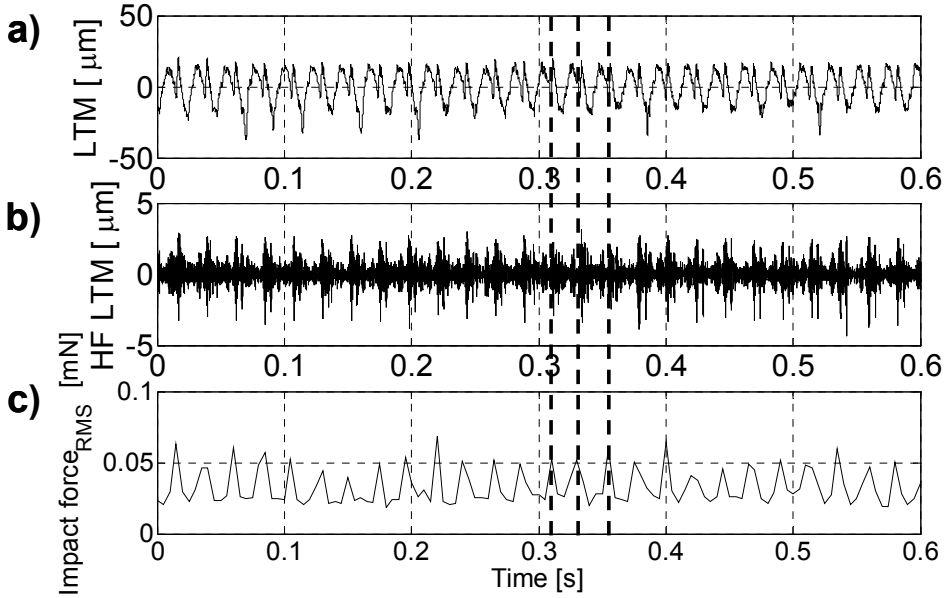

Fig. 3.4: a) LTM, b) 1 kHz high pass filtered LTM and c) rms impact force, versus time

Fig. 3.4 reveals that high frequency LTM bursts (Fig. 3.4 b)) occur at the same time when impact occurs between the tape and the flange denoted by the peaks in the rms impact force (Fig. 3.4 c)). It is thus apparent that contact between tape and roller flange causes high frequency LTM, as emphasized by the three vertical dashed lines. We note that the rms impact force never reaches zero, due to background noise in the AE measurement.

Fig. 3.5 a) shows the rms tape edge impact force, while Fig. 3.5 b) depicts the time frequency analysis of the LTM. In the time frequency analysis, a darker color denotes a higher magnitude for a particular frequency component. It is again observed that peaks in the rms impact force occur at the same instant as peaks in the time frequency signal of the lateral tape motion, which is emphasized by the three vertical dashed lines. Furthermore, Fig. 3.5 b) reveals that the high frequency components of LTM, caused by tape edge contact, predominantly occur in the 1 - 2 kHz range.

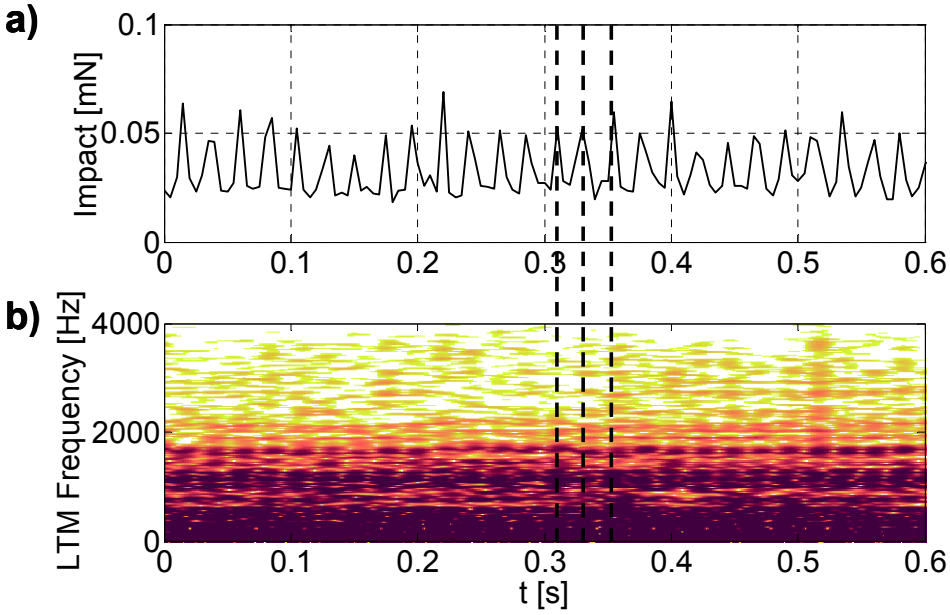

Fig. 3.5: a) rms impact force versus time b) time frequency analysis of LTM

After establishing the usefulness of AE probes in monitoring tape edge contact, the influence of the tape speed, tape tension and the supply pack diameter (whether the reel is full or empty) on tape/flange contact was investigated. Fig. 3.6 shows the average impact force versus the diameter of the supply reel tape pack (position). The background noise level for a stationary tape is indicated by the dotted line.

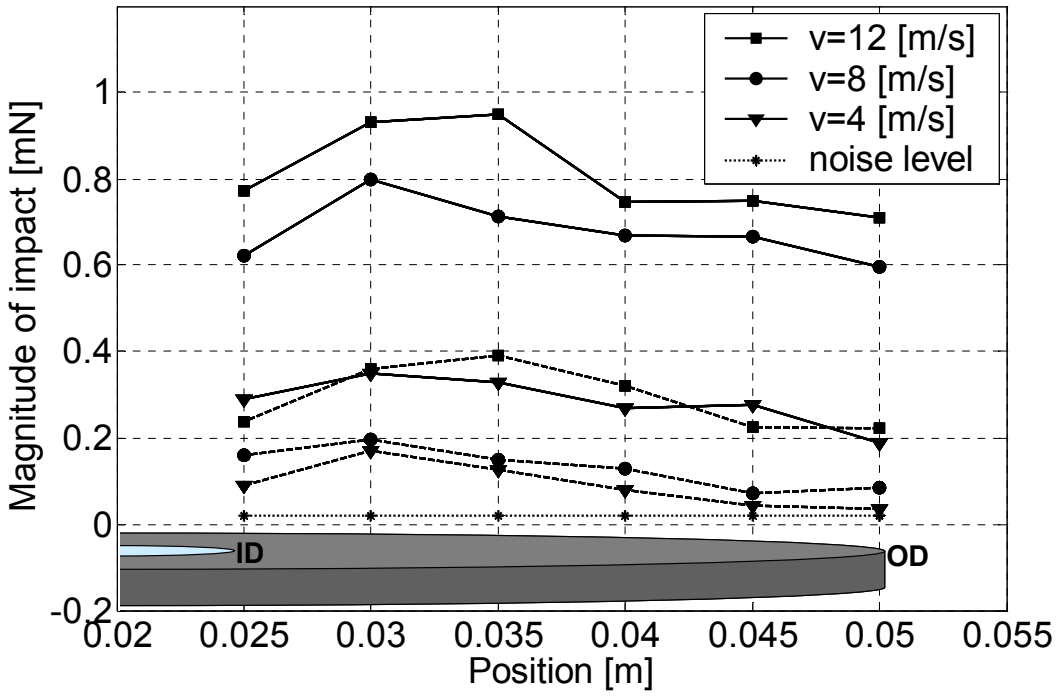

Fig. 3.6: Experimentally measured average impact force versus supply reel tape pack size, for a nominal tape tension of 1 N (solid lines) and 2 N (dashed lines) and for different tape speeds

The impact force was averaged over one second of data. Hence, the magnitude as well as the frequency of the impacts is taken into account. Fig. 3.6 indicates that the average impact force reaches a maximum when the tape reel diameter is halfway

between an empty and a full tape reel. It also becomes clear that the impact force increases with increasing tape speed and decreasing tape tension.

A tape reel is misaligned due to manufacturing and assembly tolerances for a given azimuth angle α_{az}, as shown in Fig. 3.7. Therefore, the tape is leaving the rotating reel with a periodic lateral displacement. The amplitude of this lateral displacement A_{az} depends on the diameter D, i.e., the position of the tape pack on the supply reel and the azimuth angle α. It can be expressed as

$$A_{az} = \left(D\alpha_{az}/2\right)\cos\left(2Ut/D\right) \tag{3.5}$$

where U represents the constant linear tape speed and t represents the time. A full pack (outer diameter) causes the largest lateral displacement, while an empty pack (inner diameter) causes the smallest lateral displacement.

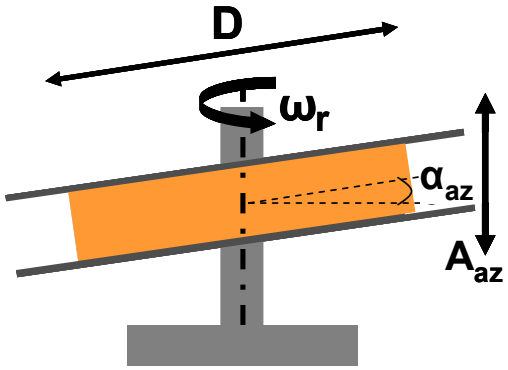

Fig. 3.7: Tape reel misalignment

To keep the tape speed constant, it is necessary that the rotational frequency $\omega_r = 2U / D$ of the tape reel is changed continuously while the pack changes its size. Thus, the frequency of impact between tape edge and a roller flange increases for a decreasing pack size, since the rotational speed of the decreasing pack size must increase. The effect of the increasing lateral displacement amplitude A_{az} versus decreasing rotational frequency ω_r for increasing pack diameter D, oppose each other with respect to the magnitude of the impact force. For an increasing pack diameter, the magnitude of the impact force will increase, while its frequency of occurrence decreases. Averaging the impact force over a certain time span (1 s in Fig. 3.6), results in a maximum of the contact force at the middle diameter of the tape reel.

3.5 Impact between tape edge and flange

The tape/flange impact can be modeled as a forced, single degree of freedom, mass spring system with "dry" friction. Since the direction of the friction force is always opposite to the direction of motion, the friction force is a piecewise constant function with respect to time. Fundamental research on so-called "impact oscillators" has been performed by Senator, who investigated the stability of periodic motions of a forced system [3.13]. Shaw and Holmes pointed out that a single degree of freedom non-linear oscillator can result in harmonic, sub-harmonic or chaotic motion [3.14]. Brach describes an impact model where the stiffness of the spring is suddenly increased by several orders of magnitude to simulate an impact [3.15]. Fig. 3.8 a) shows the physical

system of a tape sliding over a roller while Fig. 3.8 b) illustrates the mathematical model used to simulate the physical system.

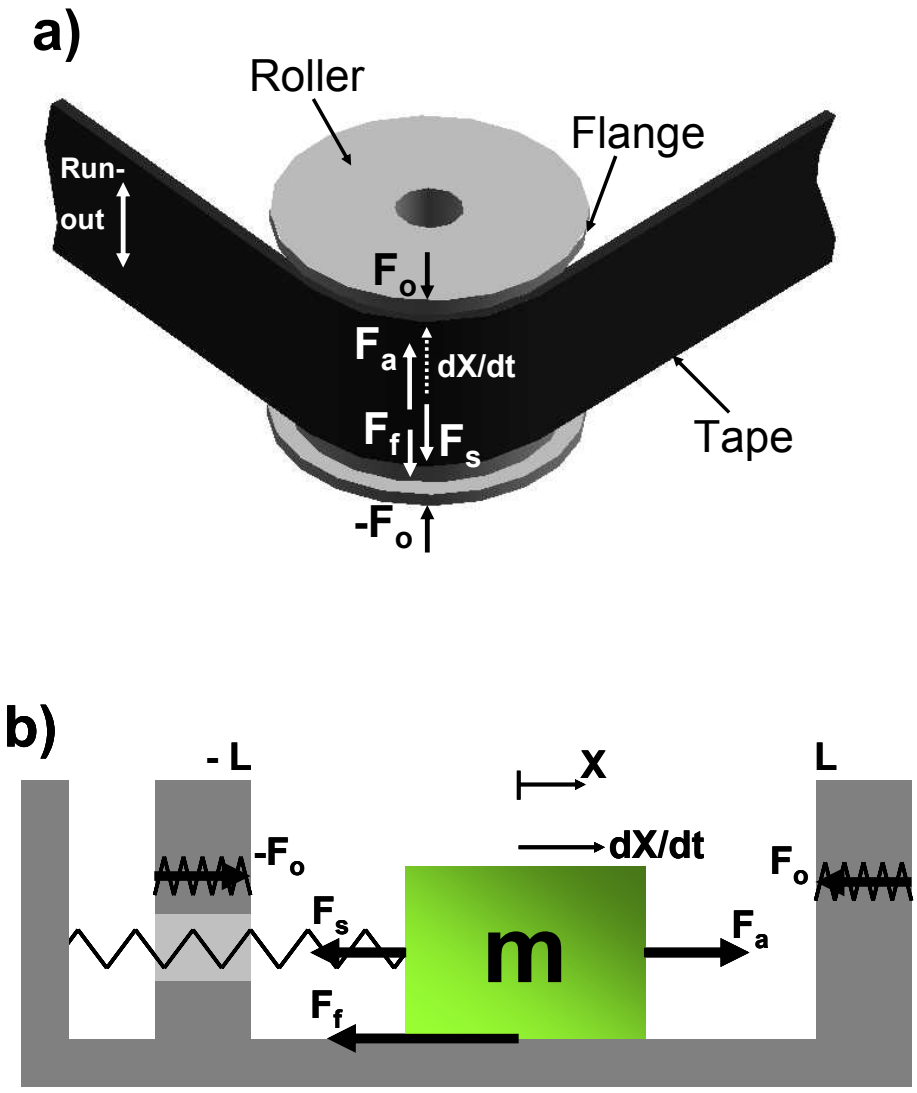

Fig. 3.8: a) Physical model and b) mathematical model

A point mass, representing the tape, is connected with a spring to a fixed base and slides over the surface that represents the roller, thereby creating a piecewise constant friction force F_f, opposite to the direction of the lateral tape motion dx/dt. The spring with effective tape stiffness k, introduces a force F_s. Furthermore, the mass m is actuated by a harmonic force F_a, representing the reel run-out that forces the tape to move up and down when coming off the supply pack. Both flanges of the roller are represented by springs with a stiffness k_0, which is several orders of magnitude higher than the effective tape stiffness k. These springs come into play when the tape edge, modeled by the point mass m, reaches the position L of the flange. They require a large force F_0 to be compressed, i.e., the springs simulate an impact. When the tape edge does not touch a flange, the spring k_0 is not present in the model. It is assumed that tape buckling does not occur in our model.

The equation of motion is given by

$$m\frac{d^2x}{dt^2} + kx + \mu N sign\left(\frac{dx}{dt}\right) = F_a \cos\omega_r t - k_0 H\left\{x^2 - L^2\right\}\left(x - L\right) \tag{3.6}$$

where x represents the position of the tape on the roller and L represents the position of the flanges. Since the tape of finite width w is represented as a point mass, x represents the clearance between the tape edge and the flanges. Furthermore, $k = m\omega_n^2$ is the effective stiffness of the tape (lateral bending stiffness). The natural frequency of the tape is ω_n and m represents the tape mass. The friction coefficient is μ and N is

the normal force acting on the tape. F_a is the amplitude and ω_r is the frequency of the applied harmonic force while t represents the time. The sign of the friction force is determined by the sign of the lateral velocity $\frac{dx}{dt}$. H is the Heaviside step function and introduces the spring with stiffness k_0 and corresponding force F_0 in the model, when the tape edge touches a flange.

Non-dimensionalization of eq. (3.6) with

$$X = x/L,\ \Lambda = t\omega_n,\ F = F_a/\left(mL\omega_n^2\right) = F_a/\left(kL\right) \text{ and } K = k_0/k \tag{3.7}$$

yields

$$\frac{d^2X}{d\Lambda^2} + X + sign\left(\frac{dX}{d\Lambda}\right)\frac{\mu N}{kL} = F\cos\left(\frac{\omega_r}{\omega_n}\right)\Lambda - KH\left\{X^2 - 1\right\}\left(X - 1\right) \tag{3.8}$$

In eq. (3.8), the linear tape transport speed enters the model through the rotational frequency ω_r of the supply reel. Since $\omega_n = \sqrt{\frac{k}{m}}$, the effective stiffness k has to be determined. Fig. 3.9 a) shows the relationship between maximum deflection $d_{\max}$ and applied force F_p, when the tape is considered to be an elastic beam of length l (Euler-Bernoulli). It can be found that [3.16]

$$\frac{F_p}{d_{\max}} = \frac{48EI}{l^3} = k \tag{3.9}$$

where E represents the Young's modulus and I denotes the area moment of the cross section of the tape. Fig. 3.9 b) shows the calculation of the belt-wrap force N as a result of the tension T in the tape. N is normal to the guide surface, indicated by the local normal force dN in Fig. 3.9 b).

$$N = 2T\sin\left(\theta/2\right) \tag{3.10}$$

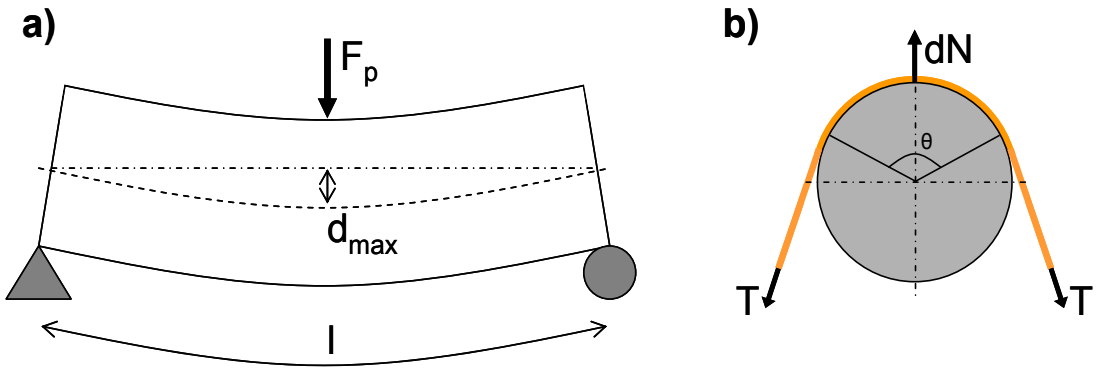

Fig. 3.9: a) Effective tape stiffness and b) belt-wrap force

The effect of tape tension and supply pack diameter on the average impact force was studied. Different tension values change the value of the normal force (see eq. (3.10)). The axial run-out at a certain tape pack diameter is simulated by the harmonic force applied on the tape. In recent studies, the variation of tape reel run-out with tape pack diameter was investigated. Lee and Wickert developed a model for predicting the stress and displacement fields within a magnetic tape pack and emphasized the importance of non-uniform stress and displacement in a tape pack with respect to tape cartridge design [3.17]. Poorman investigated the deformation of LTO cartridge reels under tape pack

stresses and found that the flange taper can change significantly as a result of packing stresses [3.18].

In our experiment, the axial run-out of the supply reel was measured with a dial indicator at different radial positions for the corresponding supply pack diameters, i.e., the pack diameter was adjusted to a desired radial position and the axial run-out at that position was measured. The measurement was repeated five times and the results were averaged over all tests. The results for the averaged axial run-out versus radial position (pack diameter) are presented in Fig. 3.10.

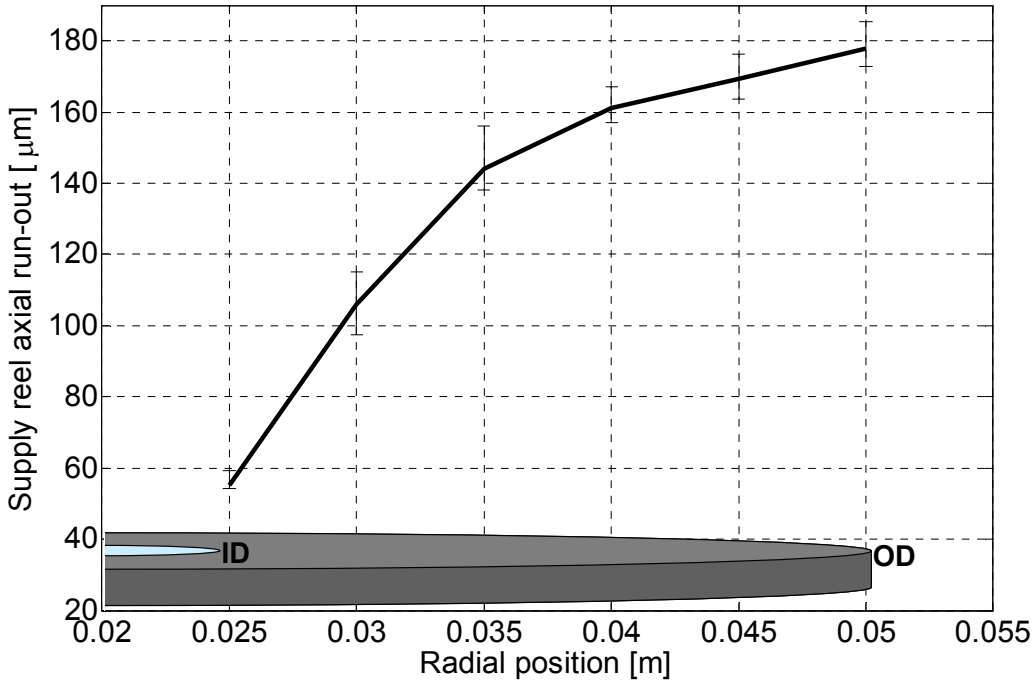

Fig. 3.10: Axial run-out of supply reel for different pack diameters

Fig. 3.10 shows that the axial run-out increases with increasing pack diameter (radial position), from about 60 μm at the inner diameter to almost 180 μm at the outer diameter. In our simulation, the harmonic forcing function F_a was calculated as the product of the measured run-out and the effective tape stiffness k. The following parameters were used: tape width $w = 0.0127$ m, tape thickness = 9 μm, Length $l = 0.01$ m, Young's modulus and density of magnetic tape (PET substrate) $E = 7$ GPa and $\rho = 1370\,\text{kg/m}^3$, respectively. The ratio of the flange stiffness versus the tape stiffness, $K = k_0 / k$ was chosen to be 10^4. The position of the flange $L = 0.001$ m and the wrap angle θ = 60 degrees. Assuming a typical friction coefficient of $\mu = 0.2$ [3.19, 3.20] and using the fourth order Runge Kutta method, we solved eq. (3.8) for the following initial conditions:

$$X = 0.95 \tag{3.11}$$

$$\frac{dX}{d\Lambda} = 0 \tag{3.12}$$

Fig. 3.11 shows the simulation results for the average impact force, calculated from the simulated $F_0(t)$, averaged over 1 s.

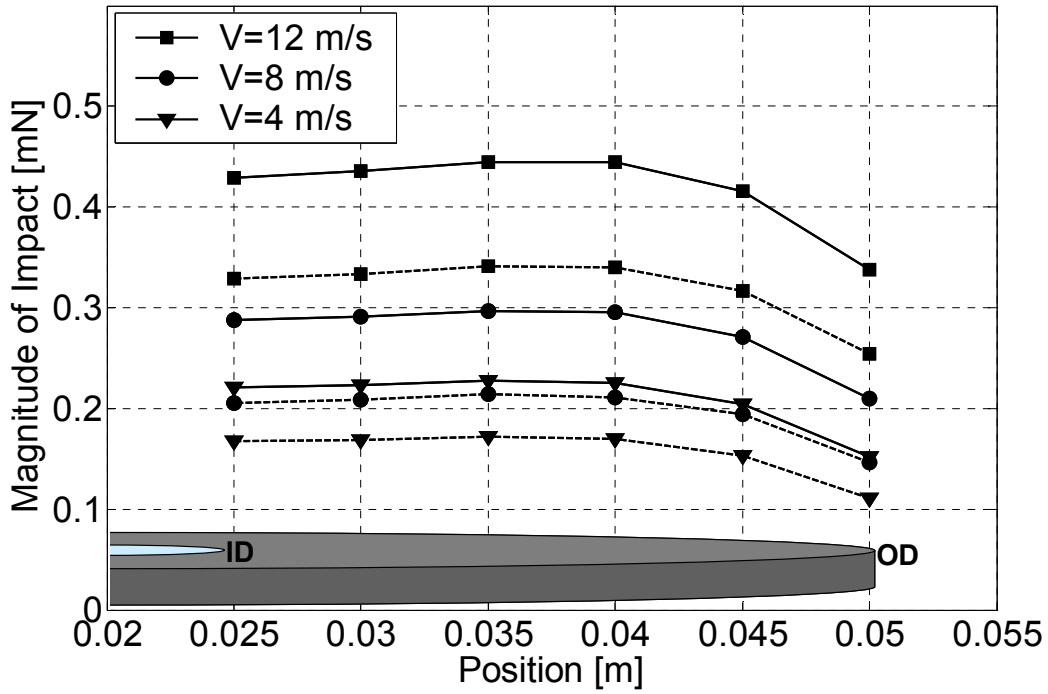

Fig. 3.11: Simulated average impact force versus supply reel tape pack size, for a nominal tape tension of 1 N (solid lines) and 2 N (dashed lines) and for different tape speeds

Fig. 3.11 shows the same trends as in Fig. 3.6 which displayed the experimental results. The one-dimensional model is only a crude approximation of the real phenomenon, which is three dimensional. Although the numerical values are not exactly matching the experimentally measured results, they are on the same order of magnitude and the simplified model captures the trends well.

Fig. 3.12 shows additional simulation results, displaying the effect of tape speed, tape tension and the wrap angle on the magnitude of the tape/flange impact with respect to the pack radius (position). Since the tension as well as the wrap angle enter the model

through the normal force N (see eq. (3.10)), their effect can be evaluated by investigating the effect of $T\sin(\theta/2)$ on the magnitude of the average impact force.

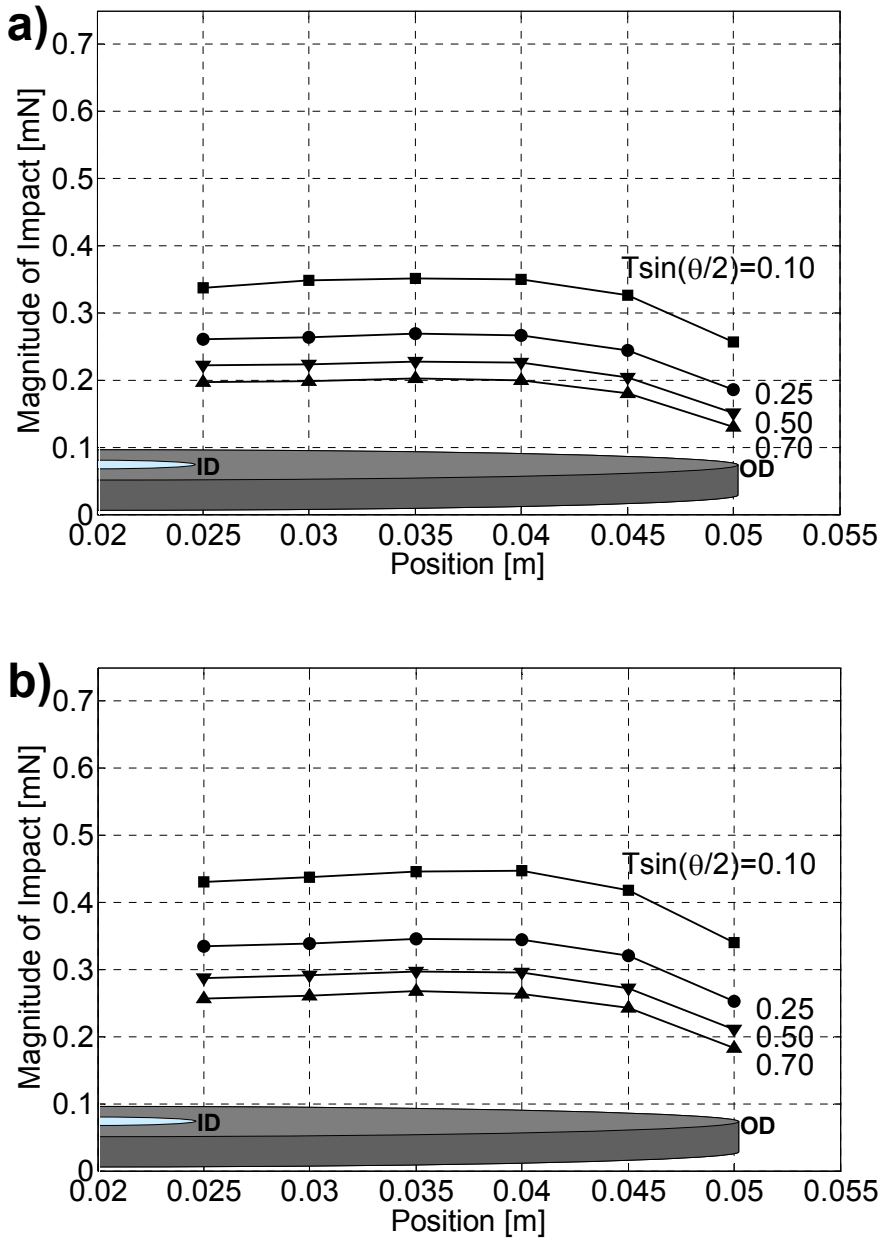

Fig. 3.12: Simulated average impact force versus supply reel tape pack size, for different values of *Tsin(θ/2)* and for a tape speed of a) 4 m/s, b) 8 m/s and c) 12 m/s

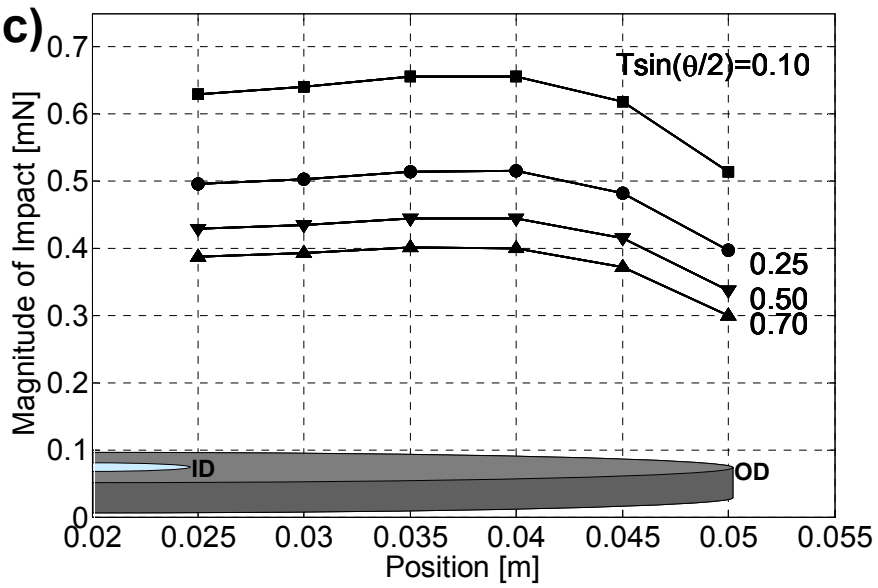

Fig. 3.12 continued: Simulated average impact force versus supply reel tape pack size, for different values of *Tsin(θ/2)* and for a tape speed of a) 4 m/s, b) 8 m/s and c) 12 m/s

We observe from Fig. 3.12 that increasing $T\sin(\theta/2)$ reduces the impact force between roller flange and tape. Increasing $T\sin(\theta/2)$ implies increasing the tape tension T or the wrap angle θ. The average impact force is higher for increasing tape speeds. In addition, Fig. 3.12 reveals that regardless of the tape speed, the impact for $T\sin(\theta/2)=0.1$ is almost double the value for $T\sin(\theta/2)=0.7$. This result is especially interesting when considering reduced nominal tape tension to accommodate thinner tapes. On the other hand, increasing the wrap angle decreases the average impact force, but also increases the contact surface between tape and roller and the friction that acts on the tape will increase accordingly. Friction will dissipate energy and hence, the average magnitude of the impact between tape and flange will be smaller.

Fig. 3.12 also illustrates that increasing tape speed increases the average magnitude of the impact. However, the effect of speed appears to be less than the effect of $T\sin(\theta/2)$. The combination of low tension and small wrap angle will yield the highest average impact forces. This effect is amplified for increasing tape speeds. Increasing tension and wrap angle, on the other hand, decreases the magnitude of the tape/flange contact.

3.5 Discussion

Tape edge contact is a significant problem in achieving track densities beyond 40 tracks/mm (1000 tracks per inch (tpi)). Impacts between tape and roller or guide flanges induce LTM in the 1-2 KHz frequency range in the tape path. This is the frequency range beyond the bandwidth of the head servo actuator, i.e., the servo system is incapable of following such high frequency lateral vibrations of the tape which can lead to track misregistration.

As tape manufacturers tend to use thinner tape to increase the volumetric storage density of a tape cartridge, the problem of tape edge contact might manifest itself more. It was observed that lower nominal tape tensions result in increasingly more severe tape flange impacts. Thinner tape implies the use of a lower nominal tension since the stress in the tape has to remain constant. Hence, thinner tape might yield more severe tape edge contact. This conclusion is in agreement with eq. (3.9). If the tape becomes

thinner, the moment of inertia I decreases and the effective stiffness constant in the simulation becomes smaller, resulting in more severe impact.

Higher storage densities also imply higher data transfer rates. Thus, higher tape speeds will be necessary in future tape drive designs. Hence, LTM originated from tape flange contact will gain in importance since we found out that tape speed will increase the average magnitude of the tape flange impact drastically.

3.6 Conclusion

From our investigation it can be concluded that:

1. Acoustic emission is a useful technique to monitor and characterize tape edge contact.
2. Tape edge contact induces undesirable high frequency lateral tape motion, predominantly in the 1 – 2 kHz region.
3. The maximum of impact force between the flange of a roller and a tape edge was observed to occur for a half full tape reel.
4. The magnitude of the impact force increases for increasing tape speed and decreases for increasing tension.
5. The magnitude of the impact force decreases for increasing wrap angles as a result of the increased friction due to the increased contact surface between tape and roller.

6. Although the one-dimensional “impact oscillator” model simplifies the tape flange contact problem drastically, it predicts the influence of operating and design parameters on tape/flange impact well.

3.7 Acknowledgements

Chapter 3, in part, is a reprint of the material as it appears in “Characterization of Tape Edge Contact Force with Acoustic Emission”, Raeymaekers B., Talke F.E., Journal of Vibration and Acoustics Transactions of the ASME, 2007. The dissertation author was the primary investigator and author of this paper.

3.8 References

[3.1] Lakshmikumaran AV, Wickert JA, 1998, Edge Buckling of Imperfectly Guided Webs, J. Vib. Acoust. T. ASME, Vol. 120, pp. 346 - 352

[3.2] Wang JH, Taylor RJ, Talke FE, 2003, Lateral Motion and Edge Wear of Magnetic Tapes, Trib. Int., Vol. 36, pp. 423 - 431

[3.3] Doyle JF, 1987, Determining the Contact Force During the Transverse Impact of Plates, Exp. Mech., Vol. 21(1), pp. 68 - 72

[3.4] Goldade AV, Bhushan B, 2004, Tape Edge Study in a Linear Tape Drive with Single-Flanged Guides, J. Mag. Mag. Mat., Vol. 271, pp. 409 - 430

[3.5] Goldade AV, Bhushan B, 2003, Measurement and Origin of Tape Edge Damage in a Linear Tape Drive, Tribol. lett., Vol. 14(3), pp. 167 - 180

[3.6] Bhushan B, Hinteregger HF, Rogers AEE, 1994, Thermal Considerations for the Edge Guiding of Thin Magnetic Tape in a Longitudinal Tape Transport, Wear, Vol. 171, pp. 179 - 193

[3.7] Taylor RJ, Talke FE, 2005, High Frequency Lateral Tape Motion and the Dynamics of Tape Edge Contact, Microsyst. Technol., Vol. 11, pp. 1166 - 1170

[3.8] Yan T, Jones BE, 2000, Traceability of Acoustic Emission Measurements Using Energy Calibration Methods, Meas. Sci. and Technol., Vol. 11, pp. L9 - L12

[3.9] Clough RB, 1987, The Energetics of Acoustic Emission Source Characterization, Materials Evaluation, Vol. 45, pp. 556 - 563

[3.10] Hsu NN, Breckenridge FR, 1981, Characterization and Calibration of Acoustic Emission Sensors, Materials Evaluation, Vol. 39, pp. 60 - 68

[3.11] Knigge B, Talke FE, 2000, Contact Measurement Using Acoustic Emission Analysis and System Identification Methods, Tribol. Int., Vol. 33, pp. 639 - 646

[3.12] Matsumoto M, Iida A, Hamaguchi T, 1993, Measurement of Slider/Disk Collision Forces Using Acoustic Emission Source Wave Analysis, Tribol. T., Vol. 36(4), pp. 736 - 740

[3.13] Senator M, 1970, Existence and Stability of Periodic Motions of a Harmonically Forced Impacting System, J. Acoust. Soc. Am., Vol. 47(5) (part 2), pp. 1390 - 1397

[3.14] Shaw SW, Holmes PJ, 1983, A Periodically Forced Piecewise Linear Oscillator, J. Sound Vibr., Vol. 90(1), pp. 129 - 155

[3.15] Brach RM, 1991, Mechanical Impact Dynamics – Rigid Body Collisions, John Wiley & sons, New York

[3.16] Popov EG, 1999, Engineering Mechanics of Solids, Prentice Hall, Upper Saddle River

[3.17] Lee YM, Wickert JA, 2002, Width-Wise Variation of Magnetic Tape Pack Stresses, J. Appl. Mech. T. ASME, Vol. 69, pp. 358 - 369

[3.18] Poorman P, 2005, LTO Cartridge Reel Deflection Under Tape Packing Stresses, Microsyst. Technol., Vol. 11, pp. 1154 - 1157

[3.19] Broese van Groenou A, 1991, Tribology of Magnetic Storage Systems: a Short Review, J. Mag. Mag. Mat., Vol. 95, pp. 289 - 312

[3.20] Raeymaekers B, Etsion I, Talke FE, 2007, The Influence of Operating and Design Parameters on the Magnetic Tape/Guide Friction Coefficient, Tribol. Lett. Vol. 25(2), pp. 161-171

4. Lateral motion of an axially moving tape on a cylindrical guide surface

4.1 Introduction

In commercial tape drives and tape manufacturing equipment, tape is guided over rollers and guides which interact with the tape surface through frictional contact. Rollers and guides in tape drives are typically small in diameter, on the order of tens of mm, due to stringent space constraints in a tape drive. On the other hand, rollers and guides in tape manufacturing process equipment can be much larger in diameter, since spatial constraints are less important.

Several researchers have studied the dynamic behavior and vibrations of a moving web between rollers. Swope and Ames [4.1] characterized and analyzed the oscillation of a string that is being wound on a bobbin. In their analysis, they assumed a perfectly flexible string without lateral bending stiffness and derived and solved the governing equations. Norwood [4.2] studied the shape of a tape positioned over a magnetic head. He investigated tape structural properties and pointed out the importance of bending stiffness in modeling the head/tape interface. Shelton and Reid [4.3] studied the lateral dynamics of a moving web and derived the differential equations for the lateral dynamic motion of a massless, moving web [4.4]. Wickert and Mote [4.5] studied the vibration and stability of an axially moving continuum with the equations of motion cast in a canonical state space form. Young and Reid [4.6] investigated the lateral and

longitudinal motion of a moving web and concluded that the lateral and longitudinal web dynamics are critical with respect to web edge alignment. Lee and Mote [4.7] investigated the transverse motion of a translating tensioned Euler-Bernoulli beam moving at constant velocity between two supports using a fourth order model. Garziero and Amabili [4.8] studied the effect of damping on the lateral vibration of an axially moving tape. The tape was modeled as a string, i.e., bending stiffness was neglected and only the lateral vibrations were investigated. Benson [4.9] used Euler-Bernoulli beam theory to predict the lateral motion of a long warped web that is transported between two rollers. Yerashunas et al. [4.10] modeled a web as a viscoelastic beam under axial tension. This model treats the web position between rollers as a function of both space and time. However, the lateral displacement of the web guided over a roller was not investigated.

The effect of guides on the lateral tape motion in a tape path has been studied by only a few researchers. Ono [4.10] described the lateral displacement of an axially moving string on a cylindrical guide surface. Bending stiffness was not included in his model. He showed that the lateral motion is governed by a second order differential equation similar to that for one dimensional heat flow. More recently, O'Reilly and Varadi [4.11] studied the dynamics of a closed loop of inextensible string which is undergoing an axial motion and of which one point is in contact with a singular supply of momentum. Taylor and Talke [4.12] investigated the interactions between rollers and flexible tape and showed that friction between the tape and the roller affects the lateral displacement of tape.

In this chapter the lateral motion of magnetic tape as it moves over a stationary guide has been studied. The effect of bending stiffness has been included, since the area moment of the tape for the transverse direction is very large. Bending stiffness is the major difference between a simplified string model and an actual magnetic tape. In addition, the effect of tape/guide friction and guide radius on the attenuation of lateral tape motion has been studied. Finally, the difference in the tape path for a string and a tape as a function of bending stiffness is evaluated.

4.2 Theoretical study

The area moment of a tape bent around the $\boldsymbol{e}_r$ direction is very large compared to the area moment for bending around the $\boldsymbol{k}$-axis. Thus, shear forces must be taken into account in describing the lateral bending stiffness of the tape. In Fig. 4.1, a section of tape is shown as it moves over a cylindrical guide surface. Vector $\boldsymbol{M}$ denotes the position of a point on the centerline of the tape between boundary points s_1 and s_2 in a fixed cylindrical coordinate system $r\varphi z$ with unit vectors $\boldsymbol{e}_r, \boldsymbol{e}_\varphi, \boldsymbol{k}$.

We made the following simplifying assumptions:

1) The magnitude of the friction force is proportional to the normal force, $F_f = \mu N$.

2) The lateral tape motion is sufficiently small so that only the first-order terms of the lateral displacement and its derivatives with respect to space or time must be retained.

3) Deformation of the tape is assumed small in the lateral direction (ψ small). Bernoulli-Euler assumptions are employed.

4) The tape moves at a constant speed U. Hence, $\partial U / \partial s = 0$.

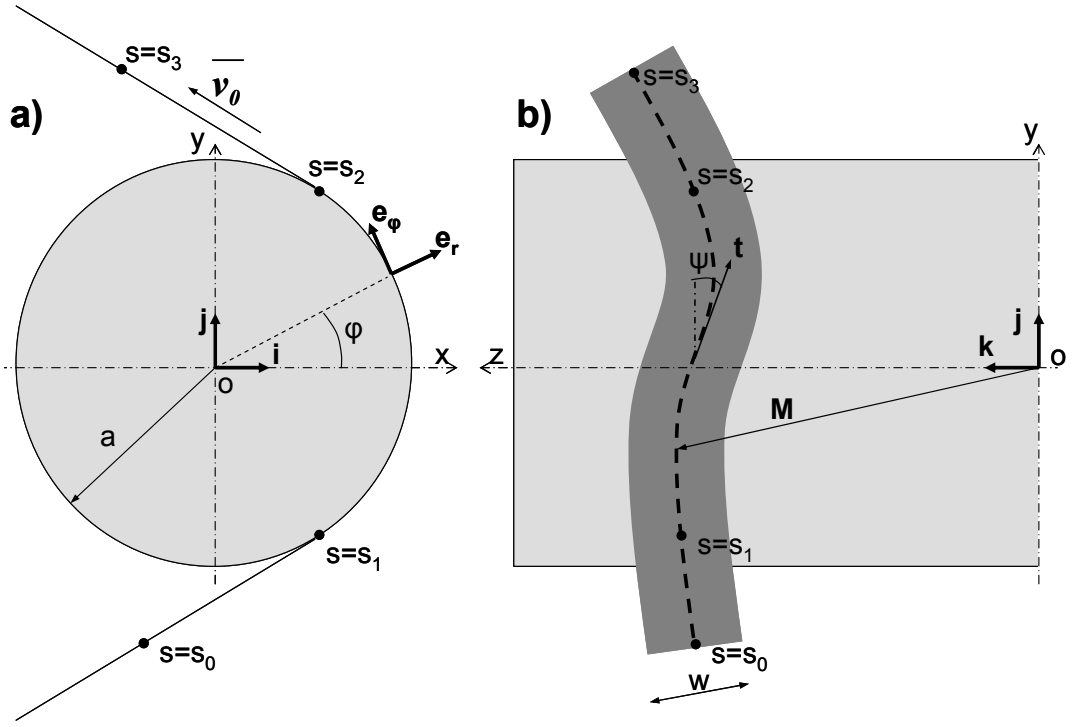

Fig. 4.1: Tape on a cylindrical guide

The forces acting on a small tape element ds are the tension force $\boldsymbol{T}$, the normal force $\boldsymbol{N}$, the friction force $\boldsymbol{F}_f$ and the shear force $\boldsymbol{V}$. Expressing $d\boldsymbol{T}$, $\boldsymbol{N}$ and $\boldsymbol{F}_f$ in r, φ, z coordinates, we obtain

$$d\boldsymbol{T}(s) = \left[-Ta\left(\frac{\partial \varphi}{\partial s}\right)^2 ds \right]\boldsymbol{e}_r + \left[\left(\frac{\partial T}{\partial s} a \frac{\partial \varphi}{\partial s} + Ta\frac{\partial^2 \varphi}{\partial s^2} \right) ds \right]\boldsymbol{e}_{\varphi} + \left[\left(\frac{\partial T}{\partial s}\frac{\partial z}{\partial s} + T\frac{\partial^2 z}{\partial s^2} \right) ds \right]\boldsymbol{k} \tag{4.1}$$

$$\boldsymbol{N} = N\boldsymbol{e}_r \text{, and} \tag{4.2}$$

$$\boldsymbol{F}_f = -\frac{Na}{U}\mu_\varphi\left[\frac{\partial\varphi}{\partial t}+U\frac{\partial\varphi}{\partial s}\right]\boldsymbol{e}_{\boldsymbol{\varphi}} - \frac{N}{U}\mu_z\left[\frac{\partial z}{\partial t}+U\frac{\partial z}{\partial s}\right]\boldsymbol{k} \tag{4.3}$$

In addition $d\boldsymbol{V}$ can be shown to be (appendix)

$$d\boldsymbol{V}(s) = \left[2EI\frac{\partial^5 z}{\partial s^5}ds\right]\boldsymbol{e}_{\boldsymbol{\varphi}} - \left[EI\frac{\partial\varphi}{\partial s}\frac{\partial^4 z}{\partial s^4}ds\right]\boldsymbol{e}_r - \left[EI\frac{\partial\varphi}{\partial s}a\frac{\partial^3 z}{\partial s^3}\left(\frac{\partial z}{\partial s}+\frac{\partial\varphi}{\partial s}\right)ds\right]\boldsymbol{k} \tag{4.4}$$

Using equilibrium of forces, we have

$$\rho w ds\frac{d^2\boldsymbol{M}}{dt^2} = d\boldsymbol{T} + \boldsymbol{F}_f + \boldsymbol{N} + d\boldsymbol{V} \tag{4.5}$$

Introducing (4.1), (4.2), (4.3) and (4.4) in (4.5), we obtain the following equations for the $\boldsymbol{e}_r$, $\boldsymbol{e}_{\boldsymbol{\varphi}}$ and $\boldsymbol{k}$ directions:

$\boldsymbol{e}_r$ direction:

$$\begin{aligned}&\rho w ds\left\{a\left(\frac{\partial\varphi}{\partial t}\right)^2 + 2aU\frac{\partial\varphi}{\partial s}\frac{\partial\varphi}{\partial t} + aU^2\left(\frac{\partial\varphi}{\partial s}\right)^2\right\}\\ &= TA\left(\frac{\partial\varphi}{\partial s}\right)^2 ds - N + EI\frac{\partial\varphi}{\partial s}\frac{\partial^4 z}{\partial s^4}ds\end{aligned} \tag{4.6}$$

$\boldsymbol{e}_{\boldsymbol{\varphi}}$ direction:

$$\begin{aligned}&\rho w ds\left(a\frac{\partial^2\varphi}{\partial t^2} + 2aU\frac{\partial^2\varphi}{\partial t\partial s} + a\frac{\partial\varphi}{\partial s}\frac{\partial U}{\partial t} + aU^2\frac{\partial^2\varphi}{\partial s^2}\right)\\ &= \left(\frac{\partial T}{\partial s}a\frac{\partial\varphi}{\partial s} + Ta\frac{\partial^2\varphi}{\partial s^2}\right)ds - \frac{\boldsymbol{N}}{U}\mu_\varphi\left(a\frac{\partial\varphi}{\partial t} + aU\frac{\partial\varphi}{\partial s}\right) + 2EI\frac{\partial^5 z}{\partial s^5}ds\end{aligned} \tag{4.7}$$

and $\boldsymbol{k}$ direction:

$$\rho w ds\left(\frac{\partial^2 z}{\partial t^2}+2U\frac{\partial^2 z}{\partial t\partial s}+U^2\frac{\partial^2 z}{\partial s^2}+\frac{\partial z}{\partial s}\frac{\partial U}{\partial t}\right)$$
$$=\left(\frac{\partial T}{\partial s}\frac{\partial z}{\partial s}+T\frac{\partial^2 z}{\partial s^2}\right)ds-\frac{N}{U}\mu_z\left(\frac{\partial z}{\partial t}+U\frac{\partial z}{\partial s}\right)-EIa\frac{\partial\varphi}{\partial s}\frac{\partial^3 z}{\partial s^3}\left(\frac{\partial z}{\partial s}+\frac{\partial\varphi}{\partial s}\right)ds \tag{4.8}$$

Substituting (4.6) in (4.8), (4.7) in (4.8), and since U is constant, the local stress change in the tape is negligible and the LTM is sufficiently small, we can assume that $\frac{\partial\varphi}{\partial t}=\frac{\partial^2\varphi}{\partial t^2}=0$, $\frac{\partial^2(a\varphi)}{\partial s^2}=-\sin\psi\frac{\partial\psi}{ds}<<1$, $\frac{\partial z}{\partial s}=\sin\psi<<1$, $\frac{\partial(a\varphi)}{\partial s}=\cos\psi\cong 1$. We can neglect the inertia terms $\rho w U^2$ versus the tension T for a typical 9 μm thick magnetic tape (Mylar-PET) with $\rho=0.012$ kg/m², $w=12.7$ mm and a typical tape transport speed $U=4$ m/s and tension $T=1$ N. Hence, we obtain the equation of motion of an axially moving tape on a cylindrical guide surface as

$$-EI\frac{\partial^4 z}{\partial s^4}+T\frac{\partial^2 z}{\partial s^2}-\frac{\mu_z T}{a}(1-\nu)\frac{\partial z}{\partial s}-\frac{\mu_z T}{Ua}\frac{\partial z}{\partial t}=0 \tag{4.9}$$

$\nu=\mu_\varphi/\mu_z$ is the ratio of the friction coefficients in the circumferential and vertical direction, respectively. In eq. (4.9), the fourth order derivative represents the bending stiffness of the tape. If the bending stiffness is neglected, i.e., $I=0$, eq. (4.9) becomes identical to the equation of motion for a string derived by Ono [4.10]. Furthermore, if $\mu_\varphi=\mu_z$, eq. (4.9) becomes

$$-EI\frac{\partial^4 z}{\partial s^4}+T\frac{\partial^2 z}{\partial s^2}-\frac{\mu_z T}{Ua}\frac{\partial z}{\partial t}=0, \tag{4.10}$$

since $\nu = 1$ in this case. If $I = 0$ and $\mu_\varphi = \mu_z = 0$, than eq. (4.8) reduces to the following equation:

$$\frac{d^2 z}{ds^2} = 0 \tag{4.11}$$

The solution of this equation is a linear function of z in terms of s, i.e., the tape moves in a straight line over the guide between points s_1 and s_2. Since equation (4.9) is difficult to solve in closed form, numerical analysis is used.

4.3 Numerical solution

4.3.1 Discretization

Equation (4.9) can be rewritten in the form

$$A\frac{\partial^4 z}{\partial s^4} + B\frac{\partial^2 z}{\partial s^2} + C\frac{\partial z}{\partial s} + D\frac{\partial z}{\partial t} = 0 \tag{4.12}$$

with the coefficients A through D given by

$$A = -EI\,, \tag{4.13}$$

$$B = T \tag{4.14}$$

$$C = -\frac{\mu_z T}{a}\left(1-\nu\right) \tag{4.15}$$

$$D = \frac{\mu_z T}{Ua} \tag{4.16}$$

To solve equation (4.12), an implicit Euler finite difference scheme is implemented with central discretization in space and forward discretization in time [4.13, 4.14]. Eq. (4.12) thus becomes

$$A\left(\frac{z_{i+2}^{j+1}-4z_{i+1}^{j+1}+6z_i^{j+1}-4z_{i-1}^{j+1}+z_{i-2}^{j+1}}{\Delta s^4}\right)+B\left(\frac{z_{i+1}^{j+1}-2z_i^{j+1}+z_{i-1}^{j+1}}{\Delta s^2}\right)$$
$$+C\left(\frac{z_{i+1}^{j+1}-z_{i-1}^{j+1}}{2\Delta s}\right)+D\left(\frac{z_i^{j+1}-z_i^{j}}{\Delta t}\right)=0 \tag{4.17}$$

where Δs is the grid stepsize in space, and Δt is the grid stepsize in time. The indices i and j refer to space and time, respectively. Rearranging the terms in equation (4.17) gives

$$z_{i+2}^{j+1}\left(\frac{A}{\Delta s^4}\right)+z_{i+1}^{j+1}\left(\frac{-4A}{\Delta s^4}+\frac{B}{\Delta s^2}+\frac{C}{2\Delta s}\right)+z_i^{j+1}\left(\frac{6A}{\Delta s^4}-\frac{2B}{\Delta s^2}+\frac{D}{\Delta t}\right)$$
$$+z_{i-1}^{j+1}\left(\frac{-4A}{\Delta s^4}+\frac{B}{\Delta s^2}-\frac{C}{2\Delta s}\right)+z_{i-2}^{j+1}\left(\frac{A}{\Delta s^4}\right)=\frac{D}{\Delta t}z_i^{j} \tag{4.18}$$

In eq. (4.18), all terms on the left hand side are unknown, while the terms on the right hand side are known. Eq. (4.18) can be stated in matrix form as

$$[G][\boldsymbol{z}]=[\boldsymbol{b}] \quad , \tag{4.19}$$

where $[G]$ is a penta-diagonal matrix. The elements of the $[G]$ matrix from are given by

$$
\begin{aligned}
G_{i,i-2} &= \frac{A}{\Delta s^4} \\
G_{i,i-1} &= \frac{-4A}{\Delta s^4} + \frac{B}{\Delta s^2} - \frac{C}{2\Delta s} \\
G_{i,i} &= \frac{6A}{\Delta s^4} - \frac{2B}{\Delta s^2} + \frac{D}{\Delta t} \\
G_{i,i+1} &= \frac{-4A}{\Delta s^4} + \frac{B}{\Delta s^2} + \frac{C}{2\Delta s} \\
G_{i,i+2} &= \frac{A}{\Delta s^4}
\end{aligned}
\tag{4.20}
$$

The corresponding elements of the $[\boldsymbol{b}]$ vector are given by

$$
b_i^{j+1} = \frac{D}{\Delta t} z_i^j \tag{4.21}
$$

4.3.2 Tape path and boundary conditions

As illustrated in Fig. 4.1, the tape makes contact with the cylindrical guide at point s_1 and comes off the cylindrical guide at point s_2. We assume that the tape is wound on a reel with zero run-out at s_3, i.e., $z(s_3,t)=0$. At s_0, the lateral displacement $f_0(t)$ is assumed to be known from experimental measurements, i.e., $z(s_0,t)=f_0(t)$. In addition we postulate that the tape moves like a rigid body between s_0 and s_1 and s_2 and s_3, where it is not supported by the guide. The distances s_1s_2 and s_3s_4 are taken much shorter than the distance s_2s_3.

Thus,

$$
z(s) = z(s_1) + \frac{(s_1 - s)}{l_1}\left(f_0(t) - z(s_1)\right) \qquad \text{for } s_0 \le s \le s_1 \tag{4.22}
$$

$$z(s) = \frac{(s_3 - s)}{l_3} z(s_2) \qquad \text{for } s_2 \le s \le s_3 \tag{4.23}$$

where l_1 is the length of the tape between s_0 and s_1 and l_3 is the length of the tape between s_2 and s_3, respectively.

The solution of eq. (4.9) for the domain $s_1\ s_2$ requires four boundary conditions, two at $s = s_1$ and two at $s = s_2$. Since the displacement of the tape is known at $s = s_0$ and since we assume that the tape moves as a rigid body in the regions $s_0 \le s \le s_1$ and $s_2 \le s \le s_3$, the slope of the tape at $s = s_1$ must be equal to the slope at $s = s_0$ and the slope of the tape at $s = s_2$ must be equal to the slope at $s = s_3$. Thus,

$$l_1 \frac{\partial z}{\partial s} - \left(z - f_0(t)\right) = 0 \quad \text{at } s = s_1, \text{ and} \tag{4.24}$$

$$l_3 \frac{\partial z}{\partial s} + z = 0 \qquad \text{at } s = s_2 \tag{4.25}$$

In addition, the curvature at s_1 and s_2 has to be zero to insure a smooth tape path, i.e.,

$$\left.\frac{\partial^2 z}{\partial s^2}\right|_{s_1, s_2} = 0 \tag{4.26}$$

Eq. (4.18) and (4.26) yield

$$
\begin{aligned}
G_{s_1+1,s_1+3} &= \frac{A}{\Delta s^4} \\
G_{s_1+1,s_1+2} &= \frac{-4A}{\Delta s^4} + \frac{B}{\Delta s^2} + \frac{C}{2\Delta s} \\
G_{s_1+1,s_1+1} &= \frac{5A}{\Delta s^4} - \frac{2B}{\Delta s^2} + \frac{D}{\Delta t} \\
G_{s_1+1,s_1} &= \frac{-2A}{\Delta s^4} + \frac{B}{\Delta s^2} - \frac{C}{2\Delta s}
\end{aligned}
\tag{4.27}
$$

and the term on the right hand side becomes

$$
b_{s_1+1}^{j+1} = \frac{D}{\Delta t} z_{s_1+1}^{j} \tag{4.28}
$$

Applying the above boundary condition (4.26) at point s_2, we find the following result with the help of eq. (4.18)

$$
\begin{aligned}
G_{s_2-1,s_2} &= \frac{-2A}{\Delta s^4} + \frac{B}{\Delta s^2} + \frac{C}{2\Delta s} \\
G_{s_2-1,s_2-1} &= \frac{5A}{\Delta s^4} - \frac{2B}{\Delta s^2} + \frac{D}{\Delta t} \\
G_{s_2-1,s_2-2} &= \frac{-4A}{\Delta s^4} + \frac{B}{\Delta s^2} - \frac{C}{2\Delta s} \\
G_{s_2-1,s_2-3} &= \frac{A}{\Delta s^4}
\end{aligned}
\tag{4.29}
$$

The corresponding term on the right hand side becomes

$$
b_{s_2-1}^{j+1} = \frac{D}{\Delta t} z_{s_2-1}^{j} \tag{4.30}
$$

4.4 Experimental validation and effect of bending stiffness

4.4.1 Apparatus

To allow a comparison of numerical results with experimental data, the apparatus shown in Fig. 4.2 was used. The set-up consists of a tape moving from a supply reel to a take-up reel at $U = 4$ m/s over a cylindrical guide with a radius of $a = 10$ mm. The nominal tape tension $T = 1$ N. The run-out of the supply reel creates LTM in the tape path. A cut-out was provided on the cylinder for the placement of the lateral tape motion edge sensor [4.1] (LTM A in Fig. 4.2 a)), mounted on a linear microstage for vertical positioning. Additionally, we measured the LTM as close as possible to the point where the tape makes contact with the guide (LTM B in Fig. 4.2 b)) and used this as input (boundary condition), $z(s_0, t) = f_0(t)$, for our numerical model.

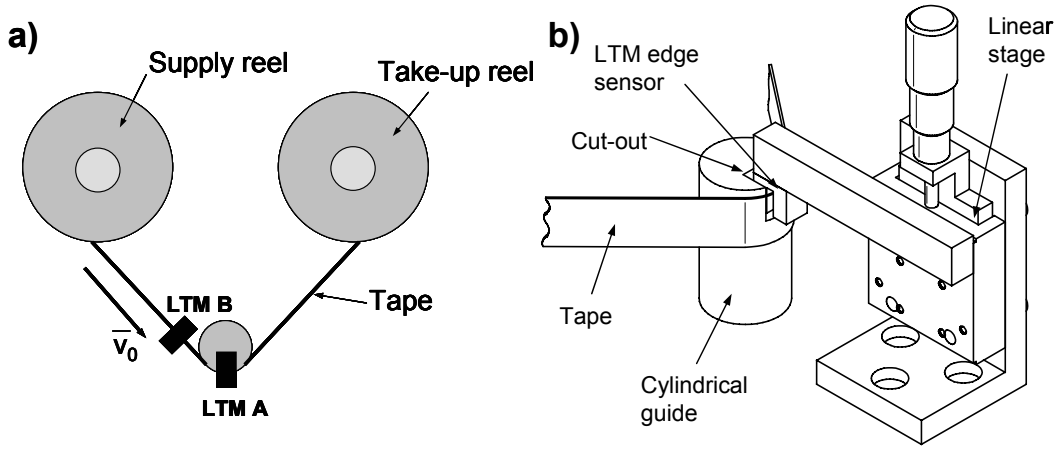

Fig. 4.2: Experimental apparatus to measure LTM on a cylindrical guide

4.4.2 Experimental results

We have compared the values of numerically calculated lateral tape motion in the middle of the cylindrical guide with experimentally measured LTM values at the same position. Fig. 4.3 a) shows simulated and experimentally measured values of lateral tape displacement in the middle of the cylindrical guide, while Fig. 4.3 b) shows the simulated and experimentally determined frequency spectrum at the same position. In our simulation we have used the following parameters: $E = 7$ GPa, $w = 12.7$ mm, $\rho = 0.012$ kg/m², $U = 4$ m/s, $a = 10$ mm, $T = 1$ N, $\nu = 1$ and tape thickness $b = 9$ μm, typical values for state-of-the-art magnetic tapes.

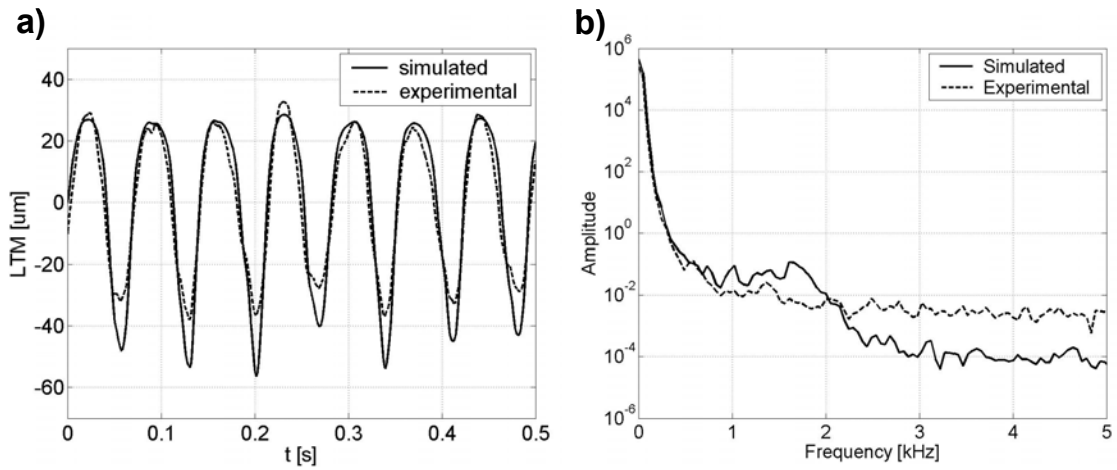

Fig. 4.3: Comparison of experimental measurements and numerical predictions in the midspan of the cylindrical guide a) in time domain and b) in frequency domain

From Fig. 4.3 we observe good agreement between experimental measurements and numerical results, especially in the low frequency region. The increased deviation

between experimental measurements and the numerical predictions for increasing frequencies is most likely related to the presence of the cut-out in the stationary guide for positioning of the lateral tape displacement sensor.

4.4.3 Tape versus string: the effect of bending stiffness

Fig. 4.4 shows a comparison of the numerically calculated frequency spectrum of a string and a tape at the mid point on the cylindrical guide for the present tape model with bending stiffness and for Ono's string model without bending stiffness. We observe that for a tape with bending stiffness, high frequency amplitudes are much stronger than in the case of a string, where bending stiffness is absent.

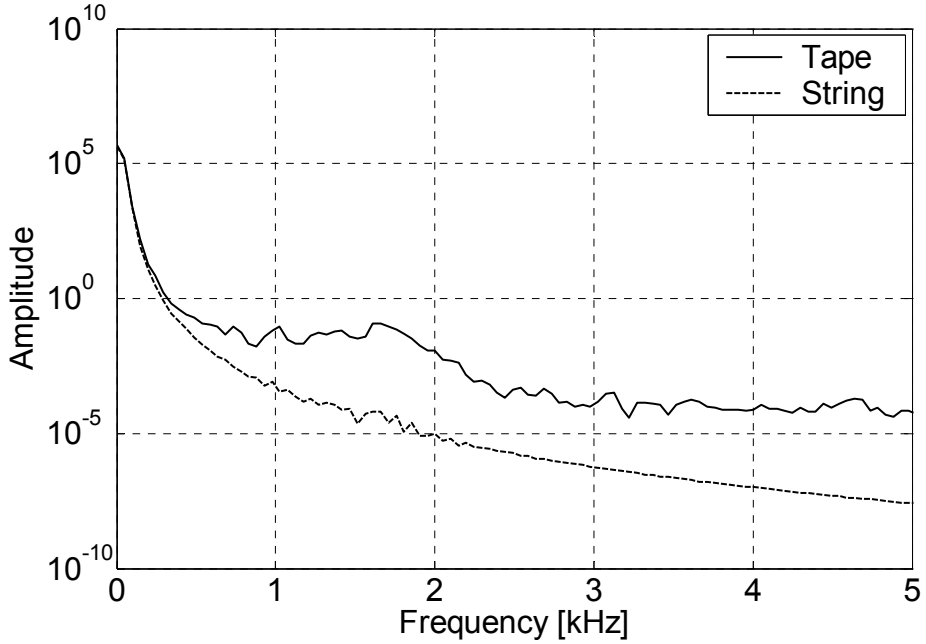

Fig. 4.4: Frequency spectrum for a tape and a string

The path of a tape with bending stiffness on a cylindrical guide is different from the path followed by a string. In Fig. 4.5, the instantaneous positions of a tape and a string are plotted as two dimensional projections over the cylindrical guide surface. Fig. 4.5 a) shows a typical trajectory of a tape and a string on a guide with a radius of 100 mm, while Fig. 4.5 b) shows the trajectory on a guide with a radius of 10 mm. The friction coefficient in both cases was assumed to be $\mu_\varphi = \mu_z = 0.2$. The instanteneous lateral displacement of the tape and string at $s = s_0$ was chosen to be 20 µm, while at $s = s_3$ the displacement was kept at 0 µm. Due to the order of magnitude difference between the two guide radii, we plotted Fig. 4.5 a) and b) using two different scales to allow proper comparison of the results. We observe that the trajectory of the tape deviates more from a straight line for a guide with a radius of 100 mm than for a guide with a radius of 10 mm. We also note that the path of the string deviates more from a straight line than the path of the tape.

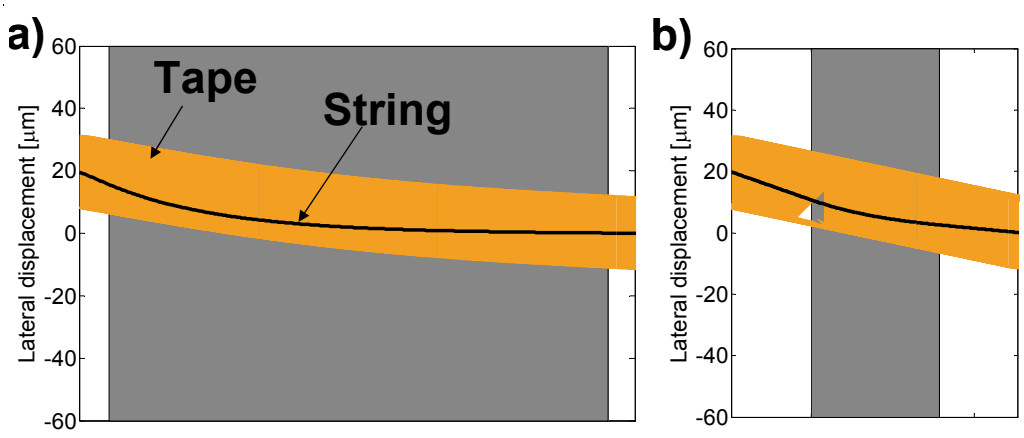

Fig. 4.5: Typical trajectory for tape and string for a guide with a) radius of 100 mm and b) radius of 10 mm. The friction coefficient is $\mu_\varphi = \mu_z = 0.2$

Fig. 4.6 shows the maximum displacement d that the tape trajectory deviates from a straight line, versus tape thickness, as a function of Young's modulus.

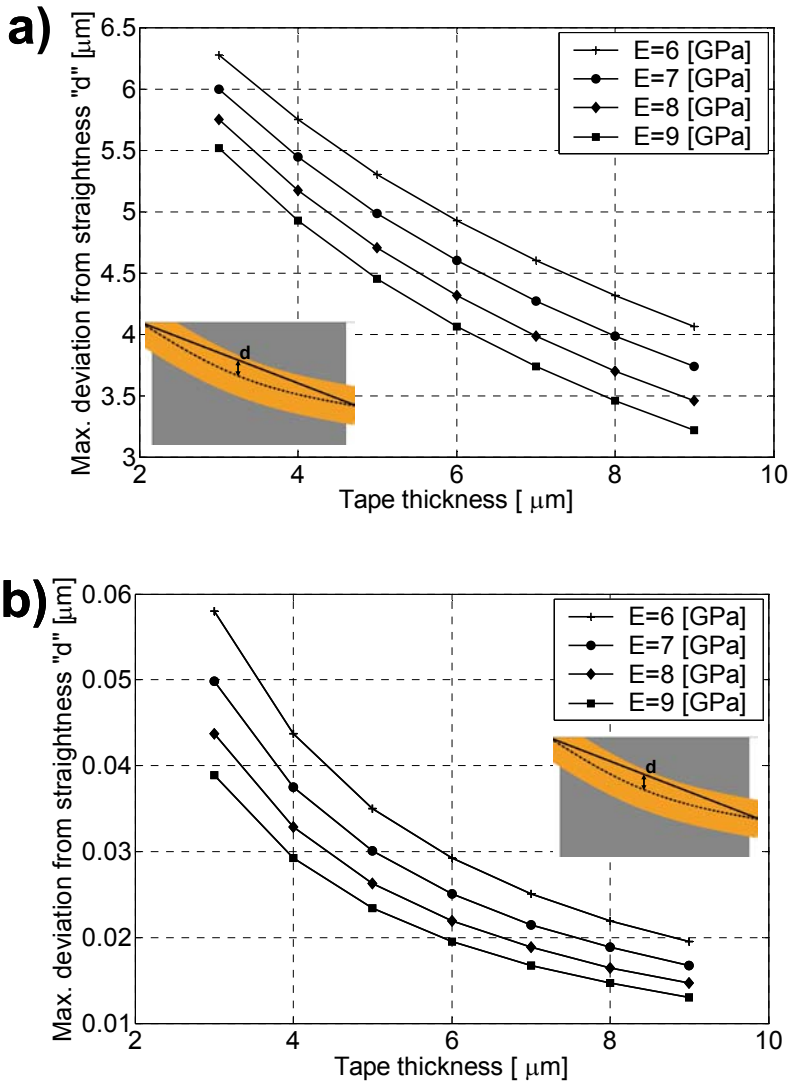

Fig. 4.6: Maximum deviation from straightness for a) a guide with radius 100 mm and b) a guide with radius 10 mm (s_0 = 20 μm and s_3 = 0 μm, $\mu_\varphi = \mu_z = 0.2$)

The results in Fig. 4.6 a) are for a cylindrical guide with a radius of 100 mm, while the results in Fig. 4.6 b) are for a cylindrical guide with a radius of 10 mm. Again, we note that the vertical plotting scale for both pictures is different. We observe that the maximum displacement d decreases with increasing Young's modulus and increasing tape thickness, i.e., d decreases with increasing bending stiffness. In addition, the maximum deviation d decreases with decreasing guide radius.

4.5 Effect of a guide in the tape path

4.5.1 Amplitude ratio

To characterize and quantify the effect of a tape guide on lateral tape motion, we have introduced the amplitude ratio ζ, defined by the output amplitude of the LTM (at point $s = s_2$) divided by the input amplitude (at point $s = s_1$), i.e.,

$$\zeta = \frac{LTM_{out}(f)}{LTM_{in}(f)} = \frac{z_{s_2}(f)}{z_{s_1}(f)} \tag{4.31}$$

The amplitude ratio ζ can be physically interpreted as a transfer function which gives information about the attenuation or amplification of LTM as a function of the frequency f. A normalized sine wave was used as input LTM (Fig. 4.7). By varying the frequency of the input LTM within a range of 0 to 10 kHz and simulating the output LTM, we have determined the amplitude ratio as a function of the frequency.

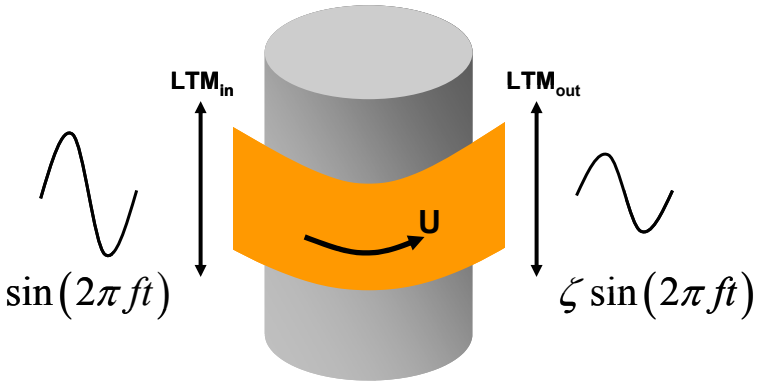

Fig. 4.7: Amplitude ratio

4.5.2. Simulation results

In the following section we have presented results for the case of a commercial tape drive, where guides are subject to tight space constraints, and where guide radii are typically on the order of 10 mm. In addition we have presented results for dimensions that are in line with those used in tape manufacturing process equipment, where guide radii of 100 mm are used.

The influence of the guide radius on the amplitude ratio ζ is depicted in Fig. 4.8 for a typical friction coefficient $\mu_\varphi = \mu_z = 0.2$, a wrap angle of 90 deg, a tape thickness of $b = 9$ µm, a tape speed $U = 4$ m/s and a nominal tape tension $T = 1$ N.

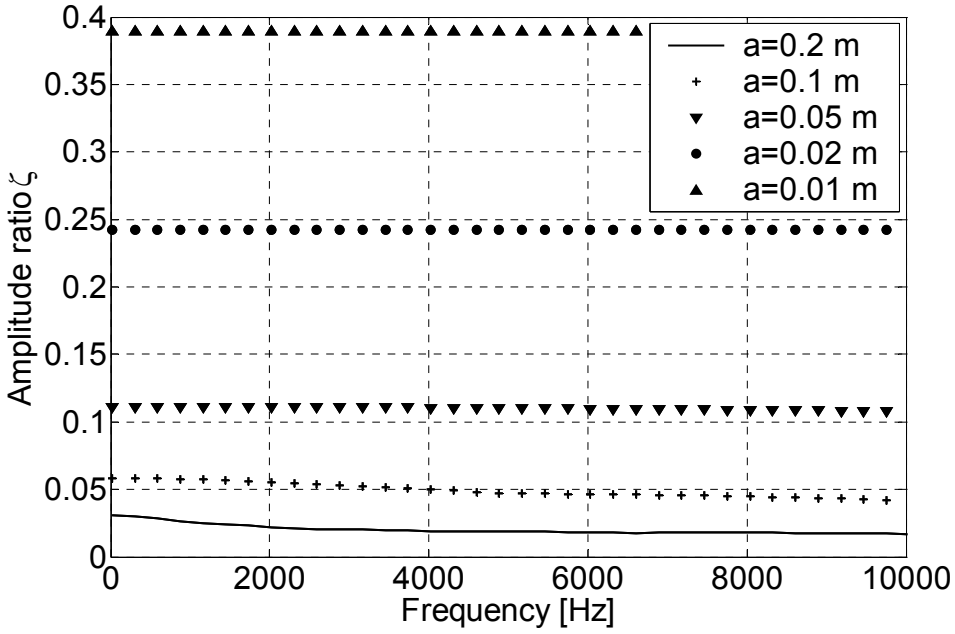

Fig. 4.8: Influence of the guide radius on the amplitude ratio as a function of frequency

We observe that the amplitude ratio is a strong function of the guide radius a. The reason for this is as follows. As the guide radius increases, the contact length between the magnetic tape and the guide increases. This causes an increased friction force which will dampen out lateral tape vibrations.

Fig. 4.9 shows the influence of the wrap angle on the amplitude ratio ζ for a friction coefficient $\mu_\varphi = \mu_z = 0.2$, a nominal tape tension of 1 N, a tape speed U = 4 m/s, a tape thickness b = 9 µm and a guide radius of 10 mm with a nominal tape tension T = 1 N.

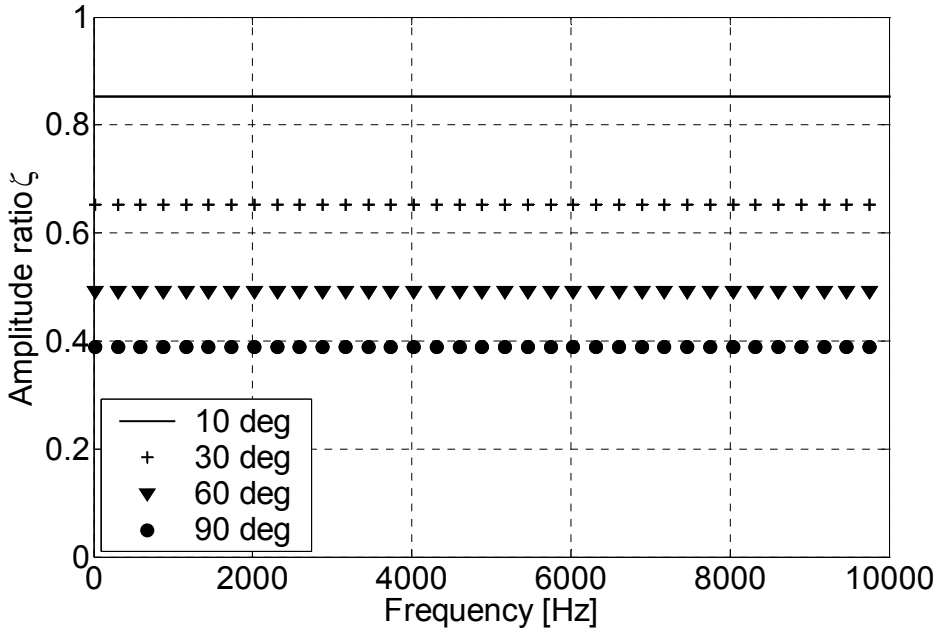

Fig. 4.9: Influence of the wrap angle on the amplitude ratio as a function of frequency

We observe that the amplitude ratio decreases with increasing wrap angle. Physically, the effect of increasing the wrap angle is similar to increasing the guide radius. Both parameters affect the tape/guide contact length. An increased contact length yields an increased friction and thus reduced LTM.

Fig. 4.10 shows the influence of the friction coefficient on the amplitude ratio ζ a) for a guide radius of 10 mm and b) for a guide radius of 100 mm. A wrap angle of 90 deg was maintained together with a nominal tape tension $T = 1$ N, a tape speed $U = 4$ m/s, a tape thickness $b = 9$ µm and a friction coefficient $\mu_\varphi = \mu_z = 0.2$.

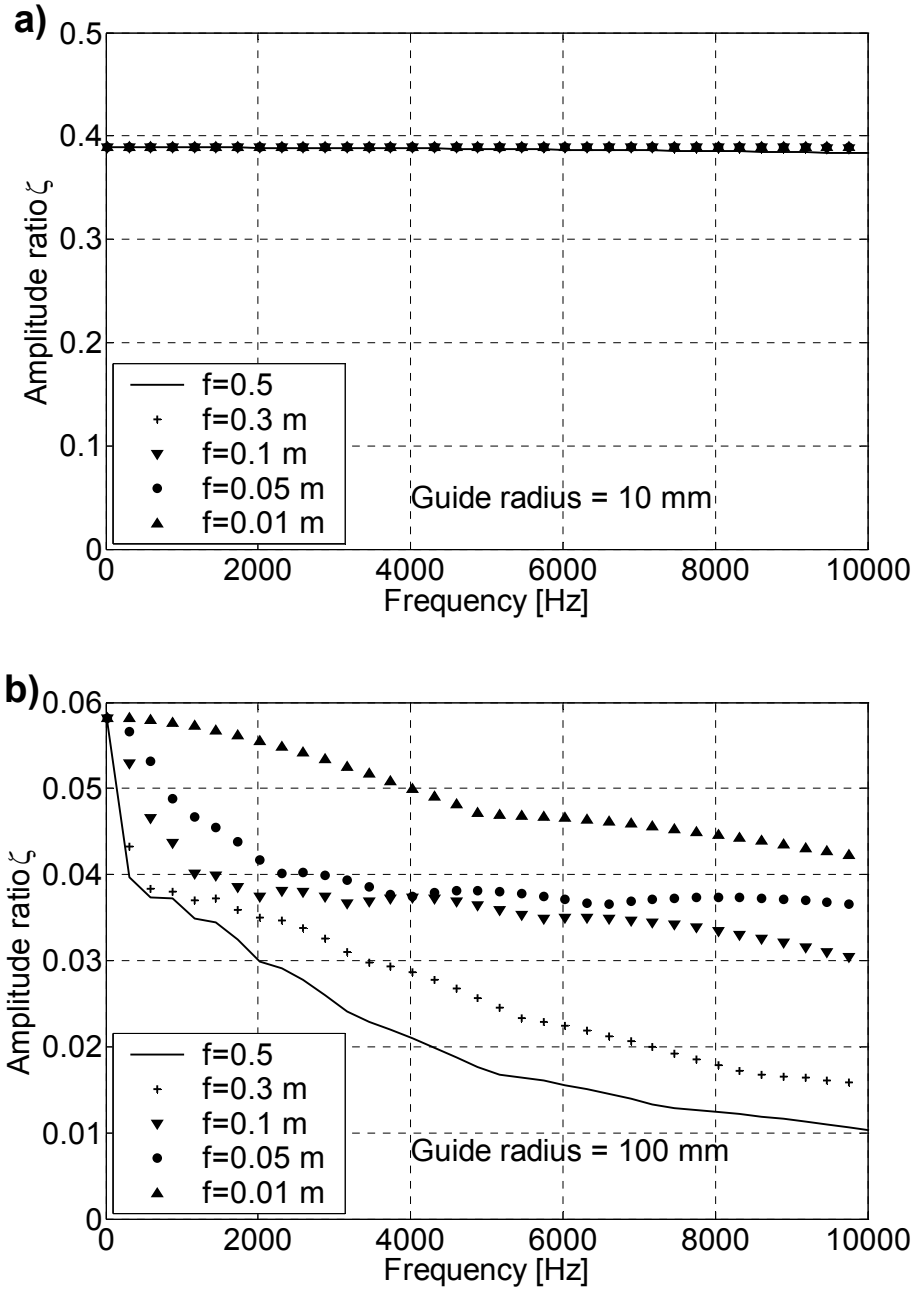

Fig. 4.10: Influence of friction coefficient on amplitude ratio as a function of frequency a) for a guide of radius 10 mm and b) for a guide of radius 100 mm

We observe that the amplitude ratio is independent of the friction coefficient for a guide of radius 10 mm (Fig. 4.10 a)), but is a stronger function of the friction coefficient for a guide radius of 100 mm (Fig. 4.10 b)). It is apparent that the amplitude ratio is dominated by the wrap angle and the guide radius, i.e., by the tape/guide contact length.

In Fig. 4.11, the influence of tape speed on the amplitude ratio ζ is shown. Fig. 4.11 a) shows the amplitude ratio versus the frequency for a guide radius of 10 mm while Fig. 4.11 b) shows the amplitude ratio for a guide radius of 100 mm. The same conditions were used as in Fig. 4.10 a) and b).

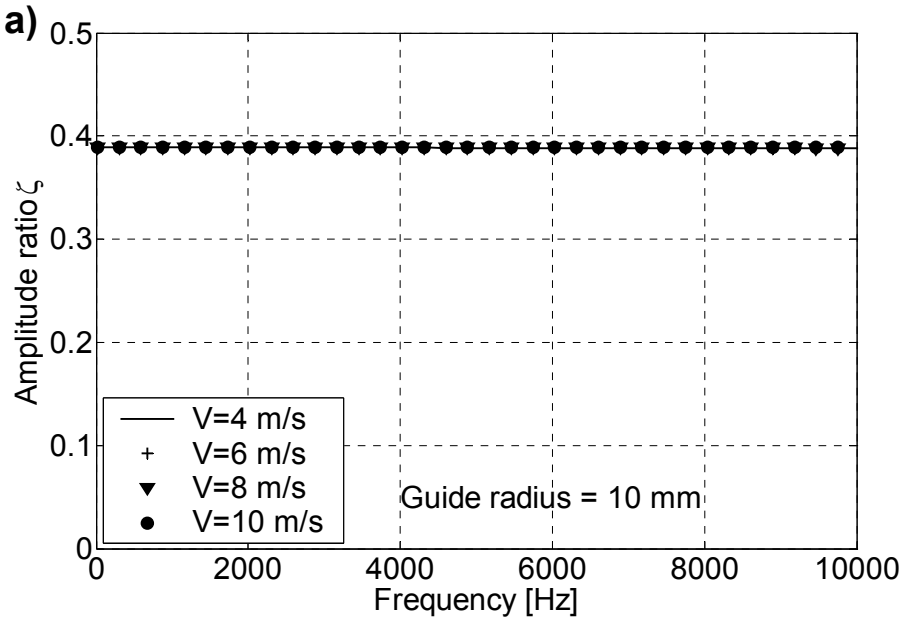

Fig. 4.11: Influence of tape speed on amplitude ratio as a function of frequency a) for a guide of radius 10 mm and b) for a guide of radius 100 mm

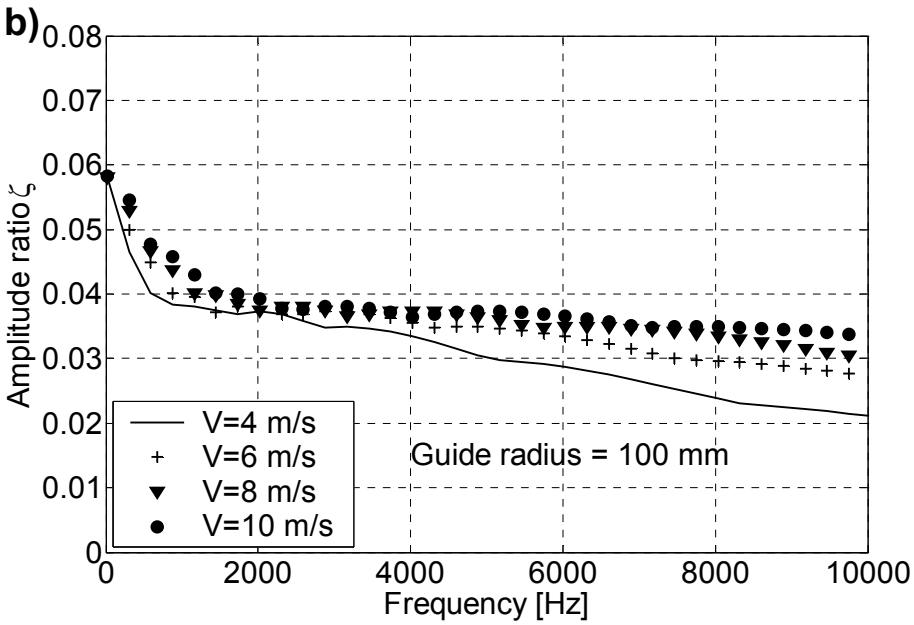

Fig. 4.11 continued: Influence of tape speed on amplitude ratio as a function of frequency a) for a guide of radius 10 mm and b) for a guide of radius 100 mm

We observe that for a guide radius of 10 mm, the amplitude ratio is almost independent of the speed. Since the effect of the friction coefficient on the amplitude ratio is small compared to the effect of the guide radius and the wrap angle, the friction coefficient was kept constant as a function of tape speed. However, the friction coefficient is expected to decrease with increasing tape speed due to the formation of a partial air bearing between the tape and the guide surface [4.17]. For the guide radius of 100 mm, the amplitude ratio is one order of magnitude smaller than for the 10 mm case, i.e., LTM is reduced more significantly.

Fig. 4.12 illustrates the influence of the nominal tape tension on the amplitude ratio ζ. The same conditions were used as in Fig. 4.10 and Fig. 4.11. Fig. 4.12 a) shows the amplitude ratio versus frequency for a guide radius 10 of mm while Fig. 4.12 b) shows the amplitude ratio for a guide radius of 100 mm.

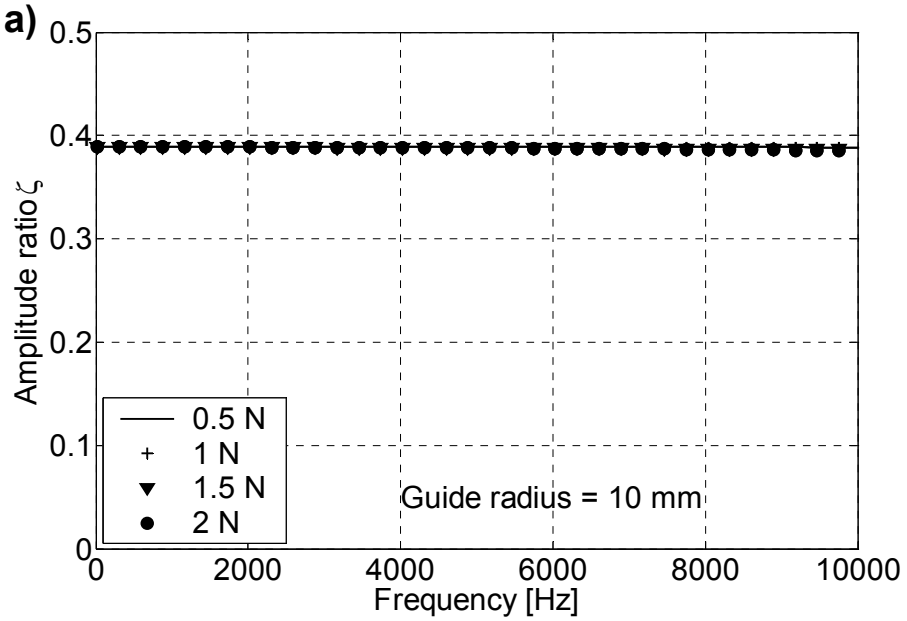

Fig. 4.12: Influence of nominal tension on amplitude ratio as a function of frequency a) for a guide of radius 10 mm and b) for a guide of radius 100 mm

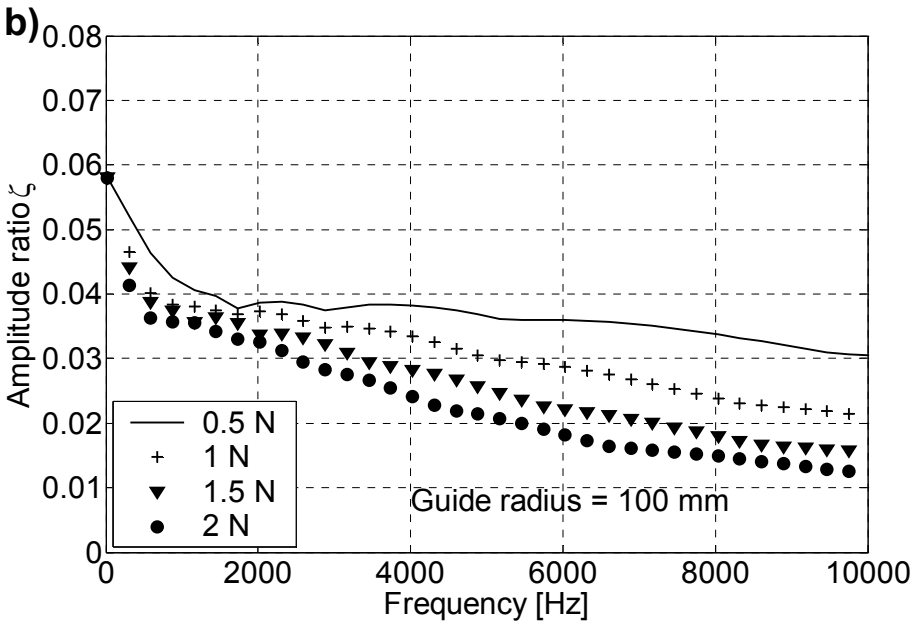

Fig. 4.12 continued: Influence of nominal tension on amplitude ratio as a function of frequency a) for a guide of radius 10 mm and b) for a guide of radius 100 mm

We observe that the amplitude ratio ζ is almost independent of tape tension for the 10 mm guide. However, for the 100 mm guide the amplitude ratio decreases for increasing tape tension (Fig. 4.12 b)). If the tape tension T increases, the "belt-wrap force" N increases as $N = 2T\sin(\theta/2)$, where θ denotes the wrap angle. An increased "belt-wrap force" creates stronger asperity contact and hence more friction. Thus, LTM will be attenuated.

Fig. 4.13 shows the influence of tape thickness. Fig. 4.13 a) shows the amplitude ratio versus frequency for a guide radius of 10 mm while Fig. 4.13 b) shows the

amplitude ratio for a guide radius of 100 mm. The wrap angle is 90 deg, the tape speed U = 4 m/s and the friction coefficient $\mu_\varphi = \mu_z = 0.2$

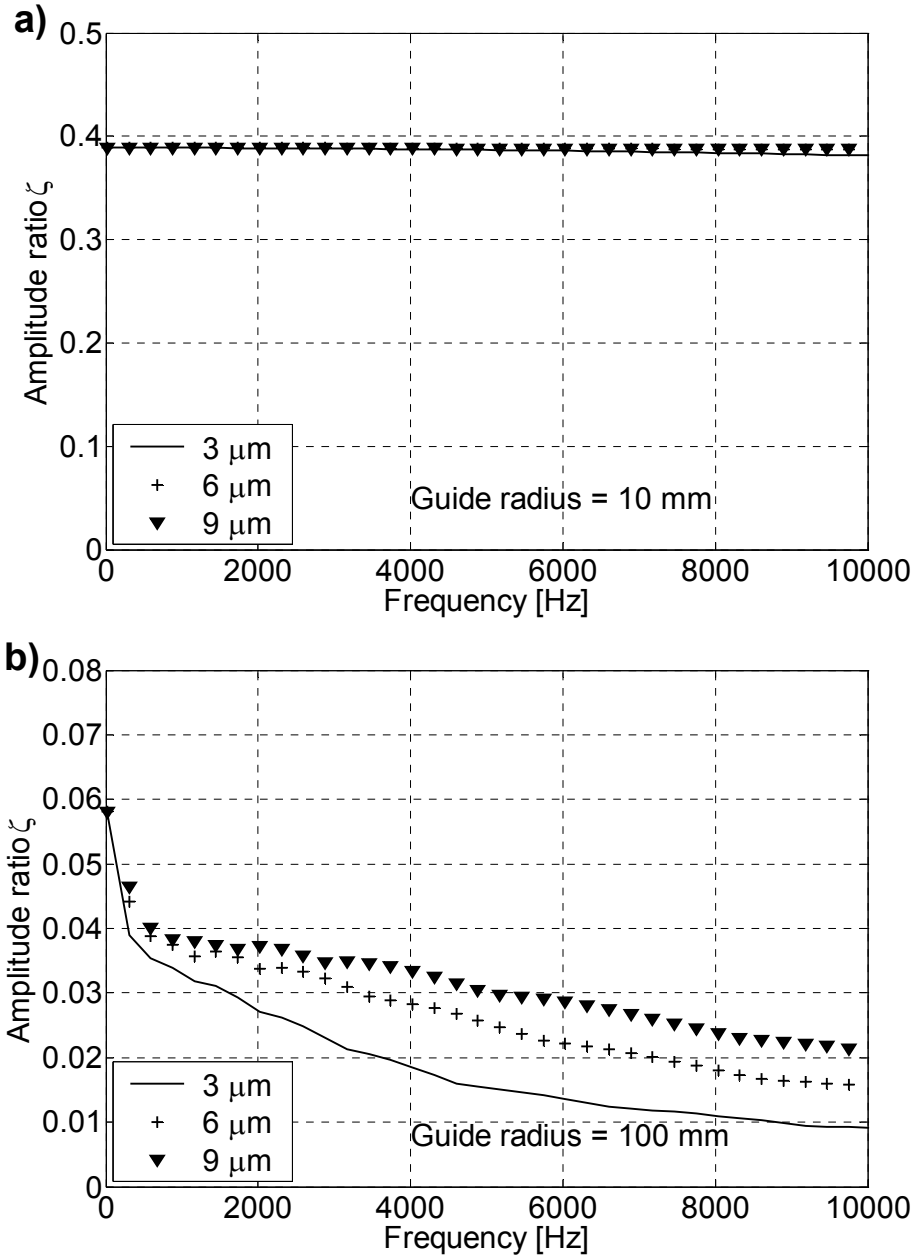

Fig. 4.13: Influence of tape thickness on amplitude ratio as a function of frequency a) for a guide of radius 10 mm and b) for a guide of radius 100 mm

Similar to the previous results, we observe that the amplitude ratio is nearly independent of the tape thickness for the 10 mm radius guide, while it decreases with decreasing thickness for the 100 mm guide radius.

4.6 Discussion

We have observed that the amplitude ratio ζ is inversely proportional to the tape/guide friction coefficient $\mu_\varphi = \mu_z = \mu$, the wrap angle θ, the nominal tape tension T and the guide radius a, and proportional to the tape speed U and tape thickness b. Hence, the amplitude ratio ζ can be defined in terms of tape design parameters as

$$\zeta = A\frac{Ub}{\mu\theta aT}, \tag{4.32}$$

where A is a proportionality constant.

It is apparent that an increase in the guide diameter or wrap angle increases the contact length and friction force. This, in turn, attenuates the LTM more strongly. In the case of commercial tape drives, the guide diameter cannot be increased arbitrarily due to space constraints. In tape manufacturing process equipment, where spatial constraints are less critical, there is greater design freedom to increase the diameter of the guides, which would reduce LTM. However, increased friction force due to increased contact length may lead to increased tape wear, and the balance between those effects must be found.

The tape industry is moving towards using thinner tapes to increase the volumetric storage density of a tape cartridge. Thinner tapes require lower tape tension to keep the stress in the tape constant. Increased storage density also calls for higher data rates (higher tape speeds). Our results show that the tape speed U, the tape thickness b, the nominal tape tension T and the friction coefficient $\mu_\varphi = \mu_z = \mu$ have only a secondary effect on the amplitude ratio for small guide diameters.

The present tape model with bending stiffness can be used to study damping and minimization of lateral tape motion. Lateral tape motion above 1 kHz cannot be followed by the servo system of the magnetic read/write head. When the amplitude of high frequency lateral tape motion is larger than 10 % of the track width, read/write errors are likely to occur. Thus, reducing high frequency tape motion before it reaches the head is desirable since it would allow narrower tracks, resulting in a higher track density and increasing the storage capacity of magnetic tape.

From the results presented it is clear that LTM can be reduced by positioning guides in the tape path before the tape passes over the read/write head. The guides would serve as “mechanical LTM-filters”. Furthermore, reducing LTM during the tape slitting process would produce tapes with improved edge quality, i.e., straighter edges.

The tape model with bending stiffness also has an important application in the tape slitting process where lateral tape displacement has to be minimized in order to

manufacture tapes with sufficiently “straight” edges. Straight edges are important for tape edge guiding [4.18, 4.19] and for servo track writing, and thus of primary concern in the tape manufacturing process. If the radius of the guides that transport the tape is increased, the amplitude of the LTM is attenuated more strongly and the edge quality of the tape produced during the slitting process should be improved. Thus, optimization of the tape path by increasing the diameter of the guides should be considered in tape slitting machines to improve the quality of future tapes.

4.7 Conclusion

The results obtained in this paper show that:

1. Bending stiffness is an important parameter in describing the lateral displacement of a tape on a cylindrical guide surface. When modeling a tape, shear forces have to be included to account for the bending stiffness.
2. The effect of a cylindrical guide in the tape path can be characterized by the amplitude ratio of output and input lateral tape displacement. The amplitude ratio mainly depends on the contact length between tape and guide surface, i.e., the guide radius and the wrap angle. An increase in the guide radius of the tape guide or an increase in the wrap angle between the guide surface and the tape improves the damping of both low and high LTM frequencies. The nominal tape tension, friction coefficient, tape thickness and tape speed also affect the amplitude ratio; however their influence is negligible with respect to the influence of the guide radius and the wrap angle.

3. The bending stiffness of the tape affects its trajectory over the cylindrical guide. As the bending stiffness increases, the tape trajectory deviates less from a straight line.
4. The tape model with bending stiffness can be used to study the design and optimization of the tape path in a tape drive and in the tape manufacturing process.

4.8 Acknowledgements

Chapter 4, in part, is a reprint of the material as it appears in "Lateral Motion of an Axially Moving Tape on a Cylindrical Guide Surface", Raeymaekers B., Talke F.E., Journal of Applied Mechanics Transactions of the ASME, 2007. The dissertation author was the primary investigator and author of this paper.

Chapter 4, in part, has been submitted for publication in "Attenuation of Lateral Tape Motion Due to Frictional Interaction with a Cylindrical Guide", Raeymaekers B., Talke F.E., Tribology International, 2007. The dissertation author was the primary investigator and author of this paper.

4.9 Appendix

Fig. A1 shows the the tension and shear force vectors with respect to the r, φ, z coordinate system.

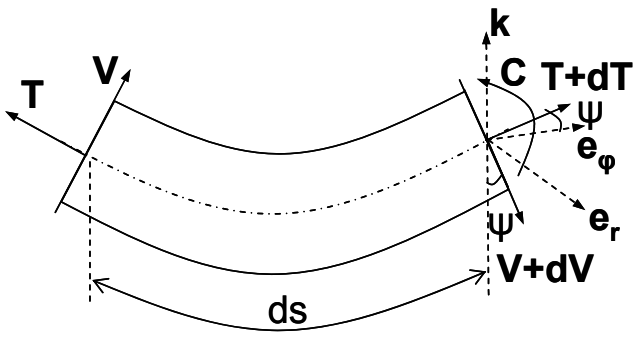

Fig. 4.A1: Shear force

From Fig. A1 we obtain

$$\boldsymbol{V} = V\boldsymbol{v} = V\frac{\partial z}{\partial s}\boldsymbol{e_\varphi} - V\frac{a\partial\varphi}{\partial s}\boldsymbol{k}\,, \tag{4.A1}$$

The unit shear vector can be written as

$$\boldsymbol{v} = \frac{\partial z}{\partial s}\boldsymbol{e_\varphi} - \frac{a\partial\varphi}{\partial s}\boldsymbol{k} \tag{4.A2}$$

thus,

$$\frac{\partial \boldsymbol{v}}{\partial s} = \frac{\partial^2 z}{\partial s^2}\boldsymbol{e_\varphi} - \frac{\partial z}{\partial s}\frac{\partial\varphi}{\partial s}\boldsymbol{e_r} - \frac{a\partial^2\varphi}{\partial s^2}\boldsymbol{k} \tag{4.A3}$$

Combining (4.A1), (A2) and (A3) with $d\boldsymbol{V}(s) = \boldsymbol{v}\frac{\partial V}{\partial s}ds + V\frac{\partial \boldsymbol{v}}{\partial s}ds$, $V = \frac{\partial C}{\partial s}$ and $C = EI\frac{\partial^2 z}{\partial s^2}$ yields

$$d\boldsymbol{V}(s) = \left[2EI\frac{\partial^5 z}{\partial s^5}ds\right]\boldsymbol{e_\varphi} - \left[EI\frac{\partial\varphi}{\partial s}\frac{\partial^4 z}{\partial s^4}ds\right]\boldsymbol{e_r} - \left[EI\frac{\partial\varphi}{\partial s}a\frac{\partial^3 z}{\partial s^3}\left(\frac{\partial z}{\partial s}+\frac{\partial\varphi}{\partial s}\right)ds\right]\boldsymbol{k}$$

(4.A4)

4.10 References

[4.1] Swope RD, Ames WF, 1963, Vibrations of a Moving Threadline, J. Franklin Institute, Vol. 275, pp. 36 - 55

[4.2] Norwood RE, 1969, Effects of Bending Stiffness in Magnetic Tape, IBM J. Res. & Dev., Vol. 13(2), pp. 205 - 208

[4.3] Shelton JJ, Reid KN, 1971, Lateral Dynamics of an Idealized Moving Web, J. Dyn., Syst., Meas. and Control T. ASME, Vol. 3, pp. 187 - 192

[4.4] Shelton JJ, Reid KN, 1971, Lateral Dynamics of a Real Moving Web, J. Dyn., Syst., Meas. and Control T. ASME, Vol. 3, pp. 180 - 186

[4.5] Wickert JA, Mote CD, 1990, Classical Vibration Analysis of Axially Moving Continua, J. Appl. Mech. T. ASME, Vol. 57, pp. 738 - 744

[4.6] Young GE, Reid KN, 1993, Lateral and Longitudinal Dynamic Behavior and Control of Moving Webs, J. Dyn., Syst., Meas. and Control T. ASME, Vol. 115, pp. 309 - 317

[4.7] Lee S, Mote Jr. CD, 1999, Wave Characteristics and Vibration Control of Translating Beams by Optimal Boundary Damping, J. Appl. Mech. T. ASME, Vol. 121, pp. 18 - 25

[4.8] Garziera R, Amabili M, 2000, Damping Effect of Winding on the Lateral Vibration of Axially Moving Tapes, J. Vib. Acoust. T. ASME, Vol. 122, pp. 49 - 53

[4.9] Benson RC, 2002, Lateral Dynamics of a Moving Web with Geometrical Imperfection, J. Dyn., Syst., Meas. and Control T. ASME, Vol. 124, pp. 25 - 34

[4.10] Yerashunas JB, Alexis De Abreu-Garcia A, Hartley T, 2003, Control of Lateral Motion in Moving Webs, IEEE T. Contr. Syst. T., Vol. 11, pp. 684 - 693

[4.11] Ono K, 1979, Lateral Motion of an Axially Moving String on a Cylindrical Guide Surface, J. Appl. Mech. T. ASME, Vol. 46, pp. 905 - 912

[4.12] Taylor RJ, Talke FE, 2005, Investigation of Roller Interactions with Flexible Tape Medium, Tribol. Int., Vol. 38, pp. 599 - 605

[4.13] Pozrikidis C, 1998, Numerical Computation in Science and Engineering, Oxford University Press, New York/Oxford

[4.14] Hirsch C, 1988, Numerical Computation of Internal and External Flows, Vol. 1 Fundamentals of Numerical Discretization, John Wiley and Sons, New York

[4.15] Berry BS, Pritchet WC, 1988, Elastic and Viscoelastic Behavior of a Magnetic Recording Tape, IBM J. Res. & Dev., Vol. 32(5), pp. 682 - 694

[4.16] Bhushan B, Tao Z, 2004, Mechanical, Hygroscopic, and Thermal Properties of Metal Particle and Metal Evaporated Tapes and Their Individual Layers, J. Appl. Polymer Science, Vol. 92, pp. 1319 - 1345

[4.17] Raeymaekers B, Etsion I, Talke FE, 2007, The Influence of Design and Operating Parameters on the Magnetic Tape/Guide Friction Coefficient, Tribol. Lett., Vol. 25(2), pp. 161 - 171

[4.18] Bhushan B, Hinteregger HF, Rogers AEE, 1994, Thermal Considerations for the Edge Guiding of Thin Magnetic Tape in a Longitudinal Tape Transport, Wear, Vol. 171, pp. 179 – 193

[4.19] Taylor RJ, Talke FE, 2005, High Frequency Lateral Tape Motion and the Dynamics of Tape Edge Contact, Microsyst. Technol., Vol. 11, pp. 1166 - 1170

5. The influence of operating and design parameters on the magnetic tape/guide friction coefficient

5.1 Introduction

The classical belt drive equation [5.1] relates the "tight-side" tension T_1 (upstream of pulley) to the "slack-side" tension T_2 (downstream of pulley) as an exponential function of the product of the friction coefficient μ and the belt/pulley wrap angle θ, i.e.,

$$\frac{T_1}{T_2} = \exp(\mu\theta) \tag{5.1}$$

This classical equation, which assumes a constant friction coefficient independent of operating conditions, is often used to measure the "belt/pulley" friction coefficient in applications such as paper, polymer and textile processing. In light of some recent findings that show deviation of the friction coefficient from the classical friction laws [5.2], a more detailed understanding of the dependence of the friction coefficient on operating parameters such as sliding speed, pulley diameter or surface finish is desirable. One of the most intricate applications of the "belt/pulley" concept can be found in magnetic tape recording, where accurate knowledge of the friction coefficient is needed. Magnetic tape is transported from the supply reel to the take-up reel, thereby passing over guides, rollers and a magnetic read/write head.

A key problem related to lateral tape motion (LTM) is the friction between tape and cylindrical guides and rollers. By investigating the effect of operating conditions such as tape speed and tape tension in conjunction with design parameters such as guide diameter, surface quality, and material properties, one can optimize the frictional behavior between tape and guide to reduce LTM and tape wear.

Broese van Groenou [5.3] suggested that the friction between tape and guides is determined by the mechanical interaction of the microscopic asperities on the two surfaces in contact. He defined the friction coefficient as the ratio of the shear strength at which the asperities yield irreversibly and the normal stress on the asperities. Osaki [5.4] pointed out tribological obstacles which need to be overcome in order to achieve higher recording area densities in tape drives. The use of metal evaporated (ME) tape, which has superior magnetic characteristics compared to magnetic particulate (MP) tape, allows increasing the recording density. However, the smoother surface of ME tapes causes a higher friction coefficient at low speed due to stiction effects. Osaki and Endo [5.5] investigated the tribology of helical scan tape drive systems and found that a higher static friction coefficient increases the generation of wear debris. They concluded that a solid lubricant reduces the friction coefficient but might damage the tape. Panda and Engelmann [5.6] studied the dependence of the friction coefficient on tape speed and investigated the importance of estimating the correct friction coefficient in the control of reel-to-reel tape drives without a tension transducer. No experimental or analytical validation of their hypothesis was provided. Taylor and Talke [5.7] investigated LTM and reported on roller interactions with a flexible tape medium. They

showed that lateral tape motion is a function of the tape/roller friction coefficient. Bhushan [5.8] investigated the friction coefficient between a magnetic tape and a guide and concluded that the friction coefficient depends on the guide radius and the nominal tape tension, but is independent of the wrap angle and the speed. In [5.8], operational parameters were used that are not within the range of parameters used in state-of-the-art high performance tape drives. Thus, a more detailed study is desirable.

The friction coefficient at the tape/guide interface is a strong function of speed. This speed dependence is caused by the formation of a partial air bearing at the tape/guide interface which leads to a reduction in the contact load between tape and guide. The air bearing causes “load sharing”, i.e., the tape is partially supported by contacting asperities and partially supported by the pressure in the air bearing. This reduces the friction coefficient significantly. At high tape speeds, a self-acting air bearing is created between the tape and the guide and hence, very low friction coefficients are observed for this regime. At low tape speeds, boundary lubrication exists and the interactions between the magnetic tape and the guide are dominated by asperity contact. A transition region exists between high and low tape speeds where air bearing effects coexist with partial asperity contact. Lacey and Talke [5.9] studied the hydrodynamic flying and the transition region effects for the case of a magnetic head in a tape drive.

Current tape friction models [5.8] rely mostly on eq. (5.1) and hence, neglect the effects of tape speed, partial hydrodynamic lubrication, surface characteristics, material properties and guide dimensions. No published papers appear to be available that

consider the effect of these parameters on the coefficient of friction between a tape and a guide. It is the purpose of this chapter to bridge this gap and present a model that includes the effects of operation and design parameters on the friction coefficient between a tape and a guide.

5.2 Theoretical model

There are two problems involved in developing a friction model for the tape/guide interface. These are: a) partial air bearing formation and "load sharing", and b) modeling of the friction contributed by the contacting asperities.

5.2.1 Load sharing

Fig. 5.1 a) shows a tape element of width w in contact with a cylindrical guide of radius a. The relative linear velocity between tape and guide is ωa, as shown in the figure. The local tape tension is denoted by T while dT is the increment in tape tension due to the local friction force F_f that resists the sliding of the tape. As shown in Fig. 5.1 b), the angular coordinate is denoted by α and the wrap angle by θ. The tape tension results in a normal load which is partially supported by the air bearing pressure and partially by asperity contact. It is justifiable to assume that contacts between tape and guide are absent if the spacing $h \geq 3\sigma_s$, where σ_s is the standard deviation of asperity summit heights distribution [5.10].

In the case of hydrodynamic lubrication between a perfectly smooth tape and guide, the spacing can be obtained from the steady-state, one-dimensional, compressible Reynolds equation with first order rarefaction effects [5.9]:

$$\frac{d}{dx}\left(ph^3 \frac{dp}{dx} + 6\lambda_a p_a h^2 \frac{dp}{dx} \right) = 6U\mu_a \frac{d}{dx}(ph) \tag{5.2}$$

In eq. (5.2), μ_a represents the air viscosity, λ_a is the mean free path of air under atmospheric conditions, p_a is the atmospheric pressure, x denotes the length coordinate along the tape/guide interface, $p(x)$ is the air bearing pressure and $h(x)$ is the spacing between the magnetic tape and the guide. In the case of rough surfaces, the mean through the surface is generally used to denote the effective spacing. Alternatively, Patir and Cheng [5.10] introduced averaging procedures ending in pressure flow and shear flow terms.

Lacey and Talke [5.9] presented an empirical expression relating the load carried by contacting asperities to the spacing at the head/tape interface. This expression depends on two parameters α^* and β^*. The parameter α^* represents the spacing at which head/tape contact begins. Hence, according to [5.10], α^* is equivalent to $3\sigma_s$ in our model. The parameter β^* represents the pressure required to force zero spacing between the head and the tape.

Based on the analysis in [5.9], one can express the load portion N_{asp} carried by the contacting asperities in the form:

$$N_{asp} = N(1 - h/3\sigma_s)^2 \text{, for } h \le 3\sigma_s \tag{5.3}$$

in which N is the maximum tape/guide contact load in the absence of any air bearing support (equivalent to parameter β^* in [5.9]).

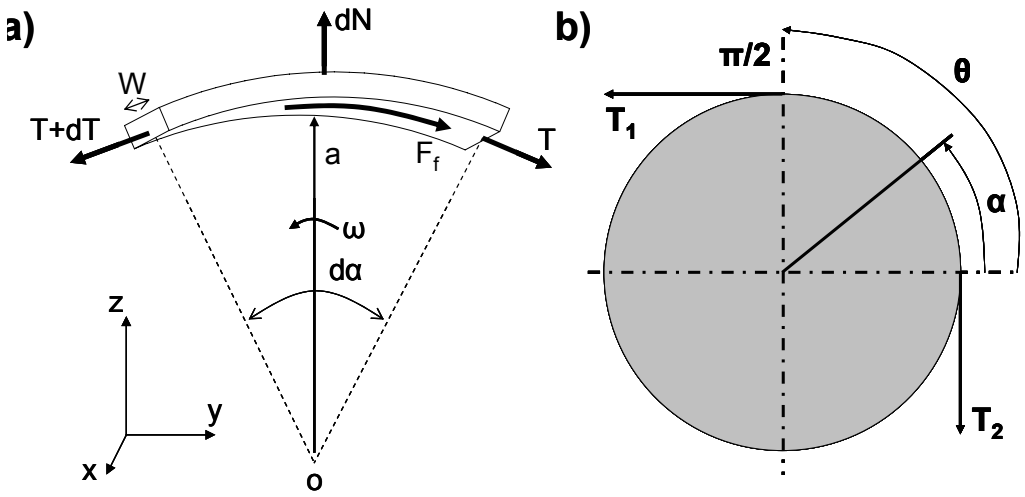

Fig. 5.1: Free body diagram of a tape element

In the absence of an air bearing between tape and guide, and assuming that $d\alpha$ is small [5.1], (i.e. $\sin\alpha \cong \alpha$ and $\cos\alpha \cong 1$), static equilibrium of forces in the z- and y-direction gives:

$$dN = Td\alpha \tag{5.4}$$

$$\mu dN = dT \tag{5.5}$$

Assuming that the friction coefficient is constant, one obtains eq. (5.1). This classical equation represents a simplified situation of the tape/guide interface, since it neglects the effects of surface characteristics, material properties and guide dimensions on the friction coefficient. In the following, a more realistic model will be developed in which these neglected effects will be included.

5.2.2 Friction model

Several friction models of rough surfaces have been proposed in the past [5.11-5.15]. Recently, Brizmer et al. [5.16] proposed a new model for the static friction coefficient for a single deformable asperity in contact with a rigid flat based on the assumption that the contact interface is under stick condition (frictional contact). They obtained numerical results for the friction coefficient μ which they presented in the form

$$\mu = 0.27 \coth\left(0.27\left(P^*\right)^{0.35}\right) \tag{5.6}$$

where the non-dimensional load P^* on one asperity has the form $P^* = P_{asp} / L_C$. Here P_{asp} is the normal load on one asperity and L_C is its critical normal load at yield inception under frictional contact, given by [5.17]

$$L_C = \overline{L_C} P_C \tag{5.7}$$

where

$$\overline{L_C} = 8.88\nu - 10.13\left(\nu^2 + 0.089\right) \tag{5.8}$$

and

$$P_C = \frac{\pi^3}{6} C_\nu^3 Y \left(r\left(1-\nu^2\right)\frac{Y}{E} \right)^2 \tag{5.9}$$

In eq. (5.9), P_C (see Ref. [5.17]) is the critical normal load in slip (frictionless), r is the radius of the asperity tip. The material properties Y, E and ν are the yield strength, Young's modulus, and Poisson's ratio, respectively, of the deformable asperity and $C_\nu = 1.234 + 1.256\nu$.

To apply eq. (5.6) to the case of the tape/guide interface, the following simplifying assumptions are made:

1. The effects of the various relevant parameters such as tape tension, guide radius, surface roughness and material properties on the dynamic friction between tape and guide are similar as on the static friction. Hence, eq. (5.6) can be used for a qualitative evaluation of these effects. This assumption is justifiable based on experimental observations reported in the literature [5.18].
2. The tape is assumed "rigid" so that local elastic deformations of the tape can be neglected. In addition, the tape is assumed to conform to the guide.
3. The contact of two rough surfaces as in the tape/guide case can be modeled by an equivalent rough surface in contact with a perfectly smooth one [5.19].

4. The actual load on each individual asperity can be approximated by an average local asperity load.

Assuming a Gaussian distribution of asperity heights [5.20], one can show that the number of contacting asperities, n, over a tape section of angular extent $d\alpha$ is given by [5.21]

$$n = \frac{\eta wad\alpha}{\sqrt{2\pi}} \int_{\bar{h}}^{\infty} \exp[-0.5(z^*)^2] dz^* = \frac{\eta wad\alpha}{2} [1 - erf(\sqrt{0.5}\bar{h})] \tag{5.10}$$

where η represents the asperity density and $\bar{h} = h/\sigma_s$ is a dimensionless spacing. Using eqs. (5.2), (5.3) and (5.9), we can express the average local load per asperity $P_{asp} = dN_{asp}/n$ as

$$P_{asp} = \frac{T(\alpha)}{\eta wa} \frac{2(1-\bar{h}/3)^2}{[1-erf(\sqrt{0.5}\bar{h})]} \tag{5.11}$$

In non-dimensional quantities, eq. (5.11) can be written as:

$$\Gamma = \frac{T(\alpha)}{\eta waL_c} \frac{2(1-\bar{h}/3)^2}{[1-erf(\sqrt{0.5}\bar{h})]} \tag{5.12}$$

where $\Gamma = \dfrac{P_{asp}}{L_C}$ is a local dimensionless tape tension, which is identical to the parameter P^* in eq. (5.6). Hence, eq. (5.6) can be re-written as:

$$\mu = 0.27 \coth(0.27\Gamma^{0.35}) \tag{5.13}$$

Finally, from eqs. (5.4), (5.5), (5.12) and (5.13) one obtains:

$$0.27 d\alpha = \frac{d\Gamma(\alpha)}{\Gamma(\alpha) \coth\left(0.27(\Gamma)^{0.35}\right)} \tag{5.14}$$

Eq. (5.14) is a non-linear ordinary differential equation which yields a solution of the form: $\Gamma / \Gamma_2 = f\left(\alpha, \Gamma_2\right)$, (5.15)

where

$$\Gamma_2 = \frac{T_2}{\eta w a L_c} \frac{2(1-\bar{h}/3)^2}{[1-erf(\sqrt{0.5}\bar{h})]} \tag{5.16}$$

is the initial condition. Since in eq. (5.15) the normalization factor is the same in the nominator as in the denominator, it can also be expressed as

$$T / T_2 = f\left(\alpha, \Gamma_2\right), \tag{5.17}$$

For a given wrap angle $\alpha = \theta$, eq. (5.17) provides the ratio T_1 / T_2 which can be used in eq. (5.1) to determine an average friction coefficient that now depends on Γ_2. Hence, this friction coefficient incorporates the tape speed (through the tape/guide spacing), the surface characteristics, the material properties and the guide geometry (see eq. (5.16)).

In order to relate the initial condition Γ_2 to a rough surface with many asperities rather than to a single asperity, we assume that each asperity in a tape section of angular extent $d\alpha$ carries the same average local load (see assumption 4). The critical interference ω_C at yield inception of a single asperity was defined in [5.17] as

$$\omega_C = \left[C_\nu \frac{\pi\left(1-\nu^2\right)}{2} \frac{Y}{E} \right]^2 r \tag{5.18}$$

Hence, from this ω_C and eqs. (5.6) and (5.8) one can obtain the relationship

$$L_C = \frac{2\pi}{3} \overline{L_C} C_\nu Y r \omega_C \tag{5.19}$$

The plasticity index ψ of contacting rough surfaces contact can be written [5.19] as

$$\psi = \left(\frac{\sigma_s}{\omega_C} \right)^{1/2} \tag{5.20}$$

Substituting L_C from eq. (5.19) in eq. (5.16) and using eq. (5.20) we finally obtain

$$\Gamma_2 = \frac{3}{\pi} \frac{T_2}{wa\bar{L}_c C_v Y} \frac{(1-\bar{h}/3)^2}{[1-erf(\sqrt{0.5}\bar{h})]} \frac{\psi^2}{\eta r \sigma_s} \tag{5.21}$$

Eq. (5.21) reveals that the plasticity index ψ, which is proportional to $(E/Y)(\sigma_s/r)^{1/2}$, has a significant effect on the solution of eq. (5.14) and hence on the average friction coefficient. In addition, the material properties ν and Y as well as the guide radius a and the tape speed, which from the analysis of [5.22] determines $\bar{h}$, have also an effect on the friction coefficient. While the trend of the effects of material properties and guide radius on Γ_2 can easily be seen in eq. (5.21), the effect of tape speed is more complex. To determine this relationship we define an "asperity load factor" of the form:

$$\beta = \frac{(1-\bar{h}/3)^2}{[1-erf(\sqrt{0.5}\bar{h})]} \tag{5.22}$$

The variation of β as a function of $\bar{h}$ is illustrated in Fig. 5.2, showing a maximum for β around $\bar{h} \approx 2.2$. Since hydrodynamic flying occurs at $\bar{h} \geq 3$, our model predicts that the asperity load factor reaches a maximum somewhat before flying inception. The model also predicts (as will be shown in the discussion of Fig. 5.5) that the friction coefficient becomes very small and independent of Γ_2 if β and thus Γ_2 approaches zero.

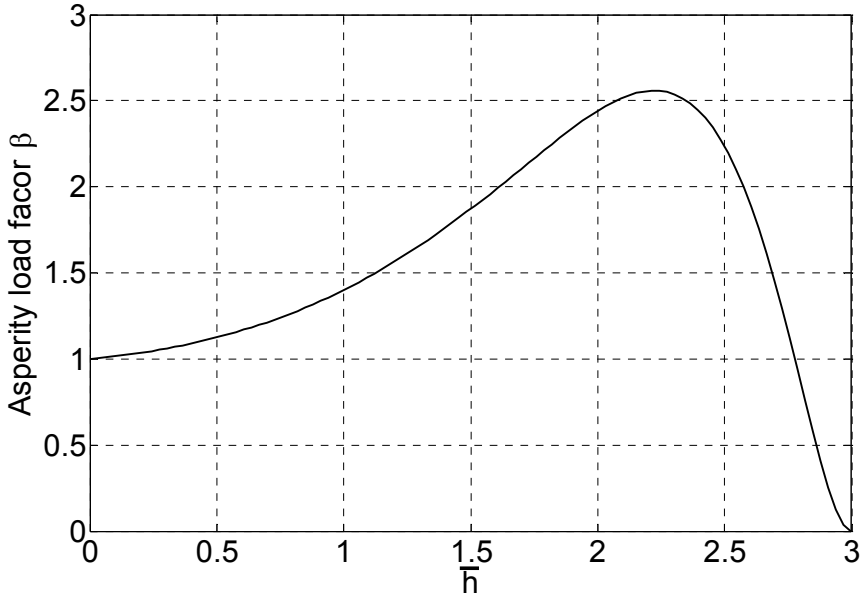

Fig. 5.2: Asperity load factor β versus dimensionless tape spacing $\bar{h}$

5.3 Experimental set-up

5.3.1 Apparatus

While in a real application the tape is sliding over a stationary guide, it is more convenient for the purpose of tension measurements to use a stationary tape sample in combination with a rotating guide.

The experimental set up, shown in Fig. 5.3, consists of a guide mounted on an adjustable speed DC-motor. A tape sample is positioned over the guide surface and is connected to a load cell that measures the tension T_1 at one end, while at the other end it is subjected to a known tension T_2 by a dead weight (see Fig. 5.3 a)). The load cell is

mounted on a sled which can slide in a circular groove to allow a variable wrap angle. Fig. 5.3 b) indicates the forces T_1 and T_2 and the wrap angle θ.

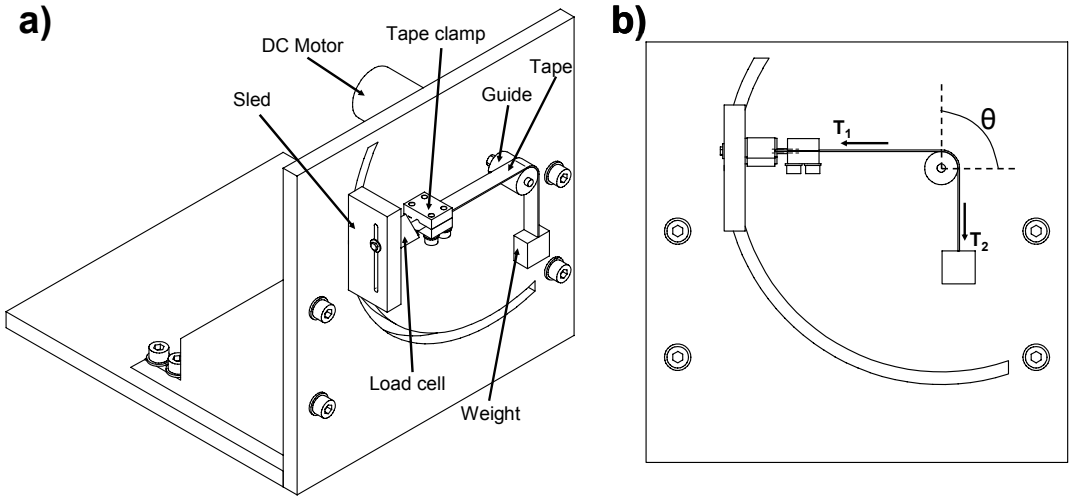

Fig. 5.3: Experimental set-up

The wrap angle can be adjusted and the rotational speed of the guide in a clockwise direction is adjustable from 0 to 125 Hz, corresponding to a maximum circumferential speed of 11.8 m/s for a guide with a radius of 15 mm. The measured force T_1 combined with the known "slack side tension" T_2 and the wrap angle θ enable calculation of the average friction coefficient μ from the ratio T_1 / T_2 using eq. (5.1).

5.3.2 Test specimens

Commercially available metal particulate (MP) tape and metal evaporated (ME) magnetic tape was used for the tests. MP tape consists of a polymer substrate, coated with a mixture of metal particles and binder material. The magnetic coating of MP tape also contains abrasive particles for recording head cleaning. ME tape is manufactured by evaporating cobalt on a polymeric substrate in a vacuum chamber.

Two types of aluminum guides with radii of 7.5 mm, 10 mm and 15 mm were used. In one case, a ceramic coating was applied and in the other case an anodizing heat treatment was used. AFM scans of the guides revealed that the surface roughness is isotropic.

Table 5.1 shows the average asperity tip radius r, the asperity density η, the standard deviation of asperity summit heights σ_s, the ratio σ_s / r and the product $\eta r \sigma_s$ for the individual tape samples and guides. The equivalent roughness parameters for two contacting rough surfaces are also shown for three tape/guide combinations. These combinations are: MP tape and a ceramic guide (C1), ME tape and a ceramic guide (C2) and MP tape in combination with an anodized guide (C3).

Table 5.1: Surface characteristics of the test specimens

	r [nm]	η [nm^{-2}]	σ_s [nm]	σ_s/r	η r σ_s
MP tape	5.55 E+3	2.18 E-6	5.34	9.63 E-4	0.064
ME tape	6.33 E+3	2.8 E-6	2.1	3.31 E-4	0.037
Ceramic	6.36 E+2	6.08 E-7	376.54	5.92 E-1	0.146
Anodized	2.17 E+3	5.08 E-7	70.72	3.26 E-2	0.078
C1	484.31	7.01 E-7	388.06	8.01 E-1	0.132
C2	484.73	7.00 E-7	388.02	8.01 E-1	0.132
C3	1.99 E3	5.53 E-7	75.77	3.82 E-2	0.083

The values in Table 5.1 were obtained using the three spectral moments m_0, m_2 and m_4 of the surface roughness as described by McCool [5.23] (see Appendix). The average radius of the asperity tips r, the asperity density η and the standard deviation of the asperity summit heights σ_s were calculated and averaged over 15 cross sections of an AFM scan for each tape and guide sample. From Table 1 we observe that the ratio σ_s / r of the anodized guide surface is an order of magnitude smaller than that of the ceramic guide surface, i.e., the surface of the anodized guide is much smoother than the surface of the ceramic guide. We also observe that the ME tape is much smoother than the MP tape. We note that while the ratio σ_s / r for the three combinations C1, C2 and C3 changes over an order of magnitude, the product $\eta r \sigma_s$ for these combinations

changes much less. Hence, Γ_2 (see eq. 5.20) is less sensitive to the dimensionless parameter $\eta r \sigma_s$ in the tested combinations.

5.3.3 Test procedure

Tape specimens of 0.1 m length were cut out of commercially available tape reels. For each test a new tape specimen was connected to the load cell through a tape clamp on one end and a 0.5 N dead weight on its other end (Fig. 5.3 a)). The tape specimen was run-in for five minutes at a rotational speed $\omega = 16$ Hz. Following this run-in procedure, the "tight side tension" T_1 was measured for stepwise increments of guide rotational speeds up to 125 Hz and was stored on a PC for further processing. The "slack-side" tension T_2 was then adjusted by adding weight, while keeping the DC-motor running. The measurements of T_1 were taken for the same range of speeds. This procedure was repeated up to a maximum slack-side tension $T_2 = 1.2$ N. The test series for each of the three combinations C1, C2 and C3 were repeated three times with a new tape specimen for each test. The calculated friction coefficient for each test was averaged over the three repetitions.

5.4 Results and Discussion

5.4.1 Theoretical results

The minimum spacing between tape and guide was calculated using the numerical procedure outlined in [5.22]. The following parameters were used: a) polyethylene terephtalate tape (PET) with a density of 1370 kg/m³, b) a Young's modulus of 7 GPa and c) a Poisson ratio of 0.3. Fig. 5.4 shows the minimum spacing versus tape speed at a nominal tape tension of 1 N for guide radii of 15 mm, 10 mm and 7.5 mm respectively.

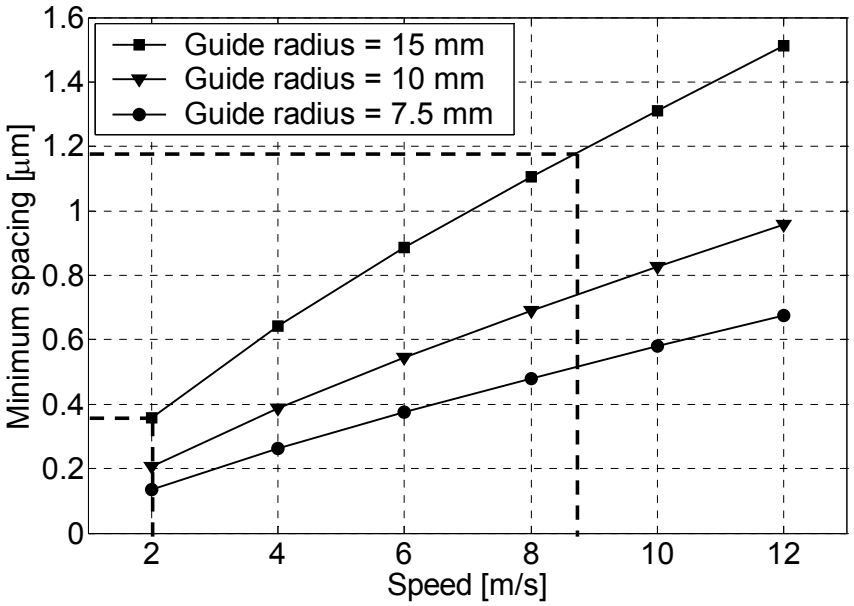

Fig. 5.4: Calculated minimum spacing versus tape speed for different guide radii at a nominal tape tension of 1 N

From Fig. 5.4 we observe that the minimum spacing increases for increasing tape speed as well as for increasing guide radius. Based on the analysis in [5.10], full fluid

film lubrication occurs when the minimum spacing between the tape and the guide is equal to or larger than $3\sigma_s$. Thus, for each of the three tape/guide combinations shown in Table 5.1, we can define a critical speed at which the transition from boundary lubrication to fluid film regime occurs. For example, for the combinations C1 and C2 (ceramic guide) in Table 5.1, we obtain $3\sigma_s = 1.164\,\mu\text{m}$, while for the combination C3 (anodized guide) we have $3\sigma_s = 0.227\,\mu\text{m}$. Correlating these values with Fig. 5.4, we conclude that with a guide radius of 15 mm at 1 N tape tension, the critical speed for combinations C1 and C2 is 8.5 m/s, while for combination C3 this critical speed is only 2 m/s, as indicated in Fig. 5.4 by the dashed lines. As we will show later (see discussion of Fig. 5.10), these values agree well with the experimental results.

For the case where the tape spacing is less than $3\sigma_s$, the asperity load factor $\beta = (1-\bar{h}/3)^2/[1-erf(\sqrt{0.5}\bar{h})]$ can be calculated from the data in Fig. 5.4 and Table 5.1. This asperity load factor is required to calculate Γ_2 according to eq. (5.21). Table 5.2 presents the values of β for some typical cases in our tests.

Table 5.2: Typical values for the asperity load factor β for tape/guide combinations C1 (MP/ceramic) and C3 (MP/anodized) at different tap tension T_2 and guide radius a

Speed [m/s]	2	4	6	8	10	12
C1, T_2=1 N, a=15 mm	1.347	2.057	2.547	0.583	0.004	0.004
C3, T_2=1 N, a=15 mm	0.004	0.004	0.004	0.004	0.004	0.004
C1, T_2=1 N, a=7.5 mm	1.073	1.201	1.378	1.6	1.863	2.152
C3, T_2=1 N, a=7.5 mm	2.195	0.004	0.004	0.004	0.004	0.004
C1, T_2=0.5N, a=7.5mm	1.179	1.532	2.038	2.507	2.231	0.22
C3, T_2=0.5N, a=7.5mm	0.004	0.004	0.004	0.004	0.004	0.004

Eq. (5.14) was integrated numerically using the fourth order Runge Kutta method to obtain the ratio Γ/Γ_2 or, equivalently, T/T_2, according to eq. (5.15) or (5.17). Fig. 5.5 shows the results as T/T_2 versus the angular coordinate α for different initial conditions Γ_2 (see eq. 5.17). We point out that the tape speed, surface characteristics, mechanical properties and guide geometry are all included (see eq. 5.21) in the model.

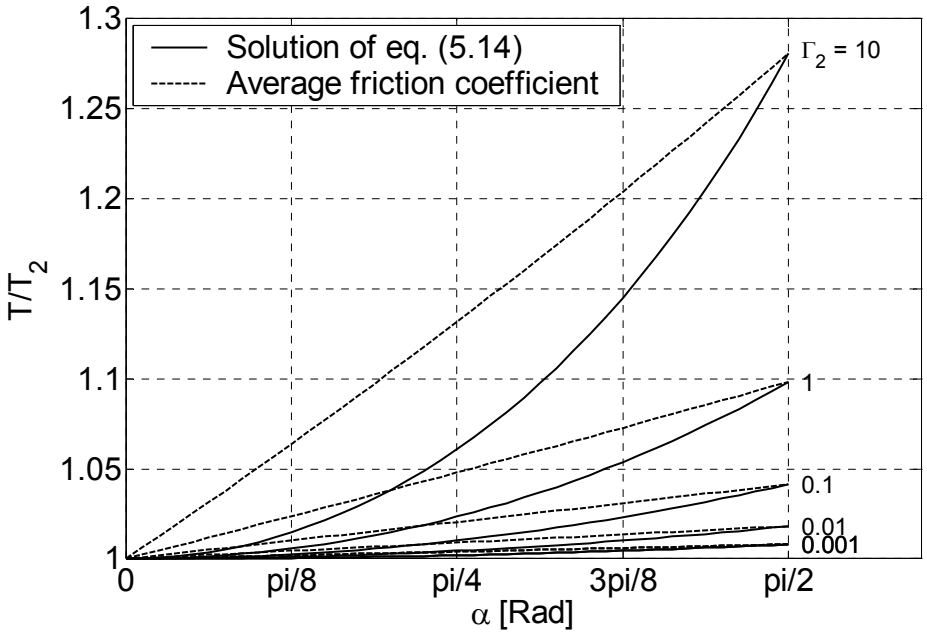

Fig. 5.5: T/T_2 **versus** α **for different values of** Γ_2

The solid lines in Fig. 5.5 present the solution of eq. 5.14 for $\theta = \pi/2$ from which the ratio T_1/T_2 at $\alpha = \theta = \pi/2$ can be determined. At a given T_2, according to eq. (5.21), a higher plasticity index ψ, which indicates a rougher surface, yields a higher Γ_2 value. Similarly, a smaller guide radius a and a smaller yield strength Y will also give higher Γ_2. As shown in Fig. 5.5, a higher Γ_2 is associated with a higher T_1/T_2 ratio and hence, according to eq. (5.1), a higher average friction coefficient. Thus, the average friction coefficient depends on tape speed, surface characteristics, material properties, and guide geometry, and is not a constant as assumed in the classical belt drive model. The average friction coefficient can be used in eqs. (5.4) and (5.5) to determine the local ratio T/T_2 versus α in the form $T/T_2 = \exp(\mu\alpha)$. These results

are also plotted in Fig. 5.5 as dashed lines. The results for T/T_2 that are based on the average friction coefficient clearly deviate from the results based on the more complete solution of eq. (5.14). The average friction coefficient, which is governed by an exponential function of α, overestimates the local tension compared to the solution of eq. (5.14) that is best described by a third order polynomial function of α.

Fig. 5.6 shows the theoretical friction coefficient μ versus Γ_2 for wrap angles of 50°, 80°, 90° and 100°.

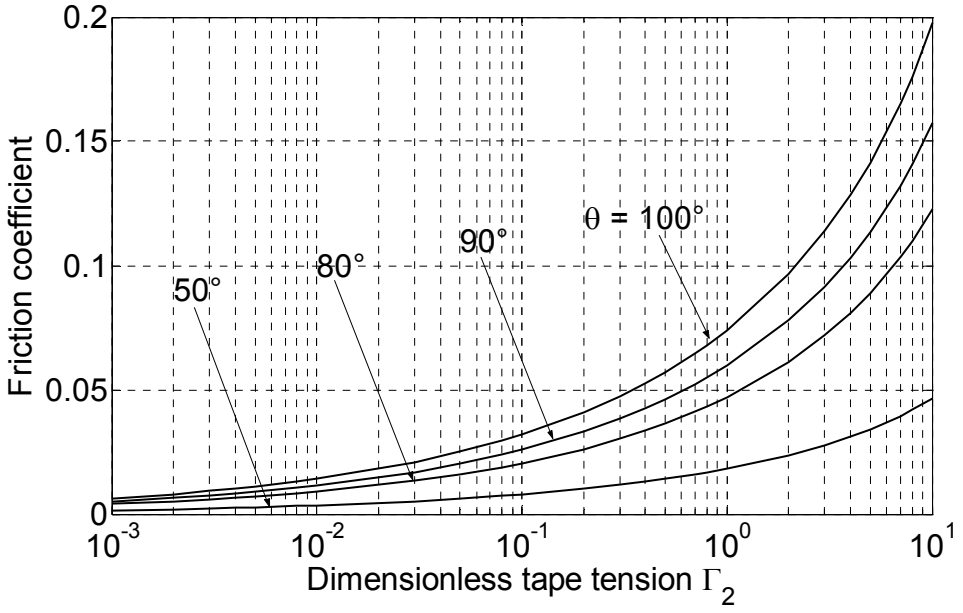

Fig. 5.6: Friction coefficient versus Γ_2 for different wrap angles

As can be seen, the friction coefficient increases slightly for a higher wrap angle in the range 80 – 100° but is substantially lower for $\theta = 50°$.

5.4.2 Experimental results

Fig. 5.7 presents experimental results for the MP tape/ceramic guide combination (C1 in Table 5.1), showing the effects of sliding speed, guide radius and tape tension T_2 on the average friction coefficient calculated from eq. (5.1). The range of the tape tension varies from 0.5 N to 1.2 N and the guide radii are 15, 10 and 7.5 mm shown in Figs. 5.7 a), 5.7 b) and 5.7 c), respectively.

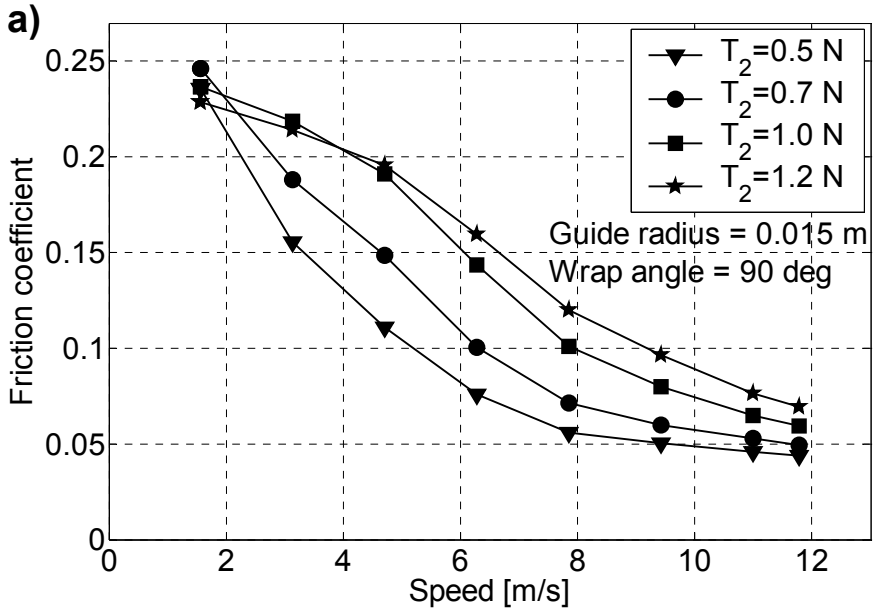

Fig. 5.7: Average friction coefficient versus speed for C1 (MP/Ceramic) combination at different nominal tape tensions and for a guide radius of a) 15 mm, b) 10 mm, c) 7.5 mm

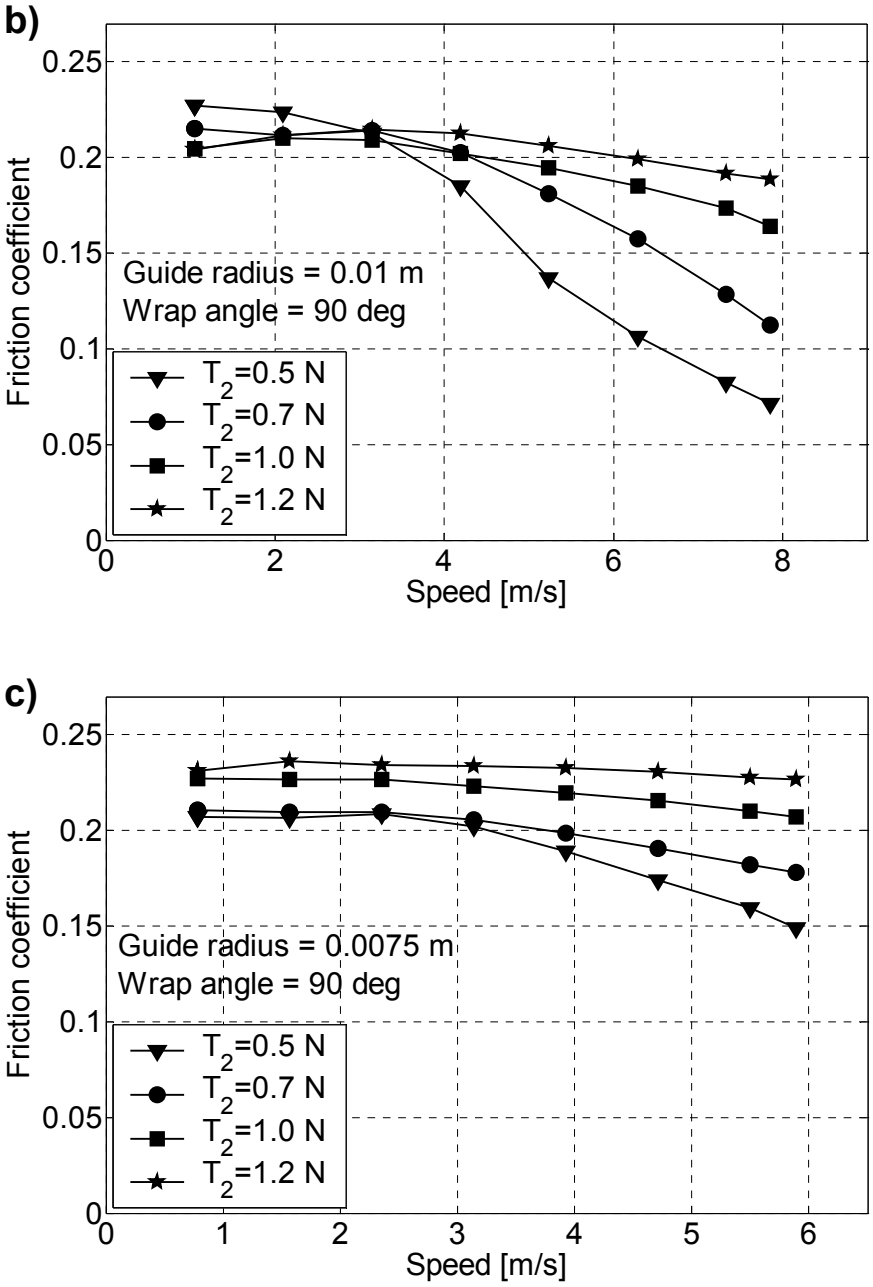

Fig. 5.7 continued: Average friction coefficient versus speed for C1 (MP/Ceramic) combination at different nominal tape tensions and for a guide radius of a) 15 mm, b) 10 mm, c) 7.5 mm

Note that at the maximum rotational speed of 125 Hz, the maximum linear speeds for the radii 15, 10 and 7.5 mm are about 12, 8 and 6 m/s, respectively. From Fig. 5.4 it is clear that a smaller guide radius requires a higher speed to maintain a given spacing. As a consequence, the friction coefficient at a given tension and speed is higher for a smaller guide radius, in agreement with our model that shows higher Γ_2 for smaller *a* values. Indeed, as can be seen in Fig. 5.7, full fluid lubrication ($\bar{h} \geq 3$) seems to exist in our tests only for the largest guide radius of 15 mm.

From Fig. 5.7 a) we observe that at the lowest speed (approximately 1.5 m/s) the friction coefficient is almost independent of the tension T_2. This differs from the prediction of our model probably because at very low speed no air bearing effects are present and elastic deformations of the tape may occur. This would violate the simplifying assumption of a "rigid" tape made in our model. It is also seen from Fig. 5.7 a) that as the speed increases, the friction coefficient decreases monotonically and becomes a strong function of tape tension, i.e., higher tape tension T_2 results in a higher Γ_2 and hence higher friction coefficient in agreement with our model (see eq. (5.21)). At the highest speed the friction coefficient is again independent of the tape tension due to the formation of an air bearing which completely removes the load from the asperities. This situation is also predicted by our model for a non-dimensional spacing of $\bar{h} \geq 3$. A similar behavior is observed in Figs. 5.7 b) and c). However, in these cases, we only see partial formation of an air bearing, because of the lower sliding speed. Identical tests were also carried out for different wrap angles between 80° and 100°

showing that the effect of the wrap angle on the friction coefficient is small, similar to the theoretical prediction for this range of θ in Fig. 5.6.

Fig. 5.8 shows the average friction coefficient versus guide radius for the C1 (MP/ceramic) combination at a sliding speed of 6 m/s. As can be seen, the average friction coefficient decreases with increasing guide radii as was also predicted by our model (see eq. (5.21)).

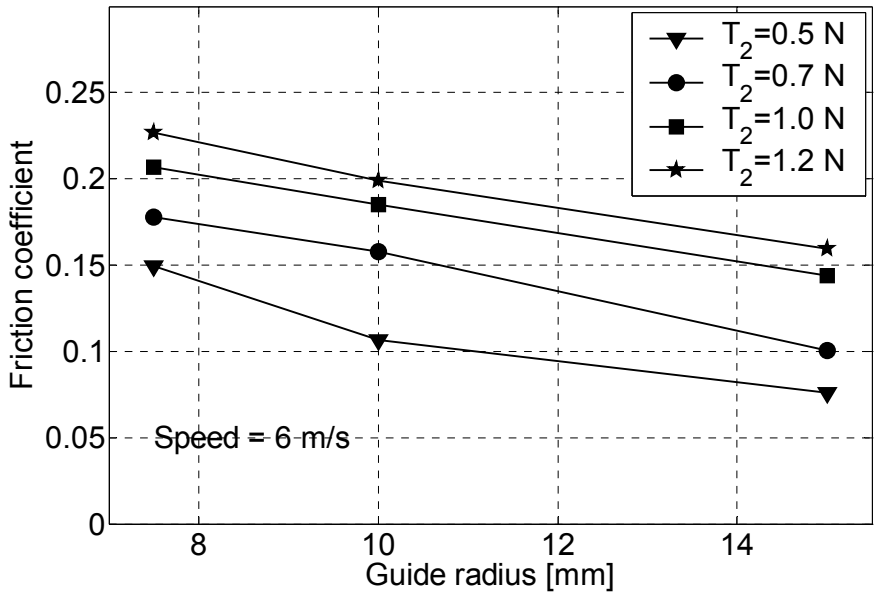

Fig. 5.8: Average friction coefficient versus guide radius for C1 (MP/Cermamic) combination at different nominal tape tensions and a tape speed of 6 m/s

In order to increase the recording density, tape manufacturers use metal evaporated (ME) tape, consisting of a high coercivity cobalt film, evaporated on the tape substrate in a vacuum chamber, as described already in chapter 1. Hempstock and Sullivan [5.24] studied the durability and signal performance of ME and MP tapes and concluded that MP tape exhibits far greater durability than ME tape. In another study Hempstock and Sullivan [5.25] identified the mechanical failure mechanism of ME tape as a form of delamination wear. Bijker et al. [5.26] discussed the use of wear protective coatings such as diamond like carbon (DLC) and a so-called super protective layer (SPL) to potentially improve the wear characteristics of ME tape. They concluded that protective coatings need further development to withstand abrasive wear.

The rotating guide of our test set-up stalled due to high stiction when attempting to test the ME tape over the full operating range (speed and tension) which was previously used with MP tape. Hence, in order to overcome the higher stiction tendency inherent to ME tape [5.4], and allow comparison with MP tape, a test was performed for both media using a low tape tension of 0.1 N in combination with an 80 degree wrap angle and a guide radius of 15 mm. Fig. 5.9 presents the comparison between the ME and MP tapes showing very similar values of friction coefficient over the entire speed range. From Table 5.1 we observe that although the ME tape has a σ_s / r value that is three times lower than that of the MP tape, the equivalent σ_s / r values for the combinations C1 (MP tape and ceramic guide) and C2 (ME tape and ceramic guide), and their corresponding plasticity index values, are almost identical. Hence, as can be seen from

eq. (5.21), a similar trend of the average friction coefficient versus speed for the MP and ME tapes is predicted by the model in agreement with the experimental results.

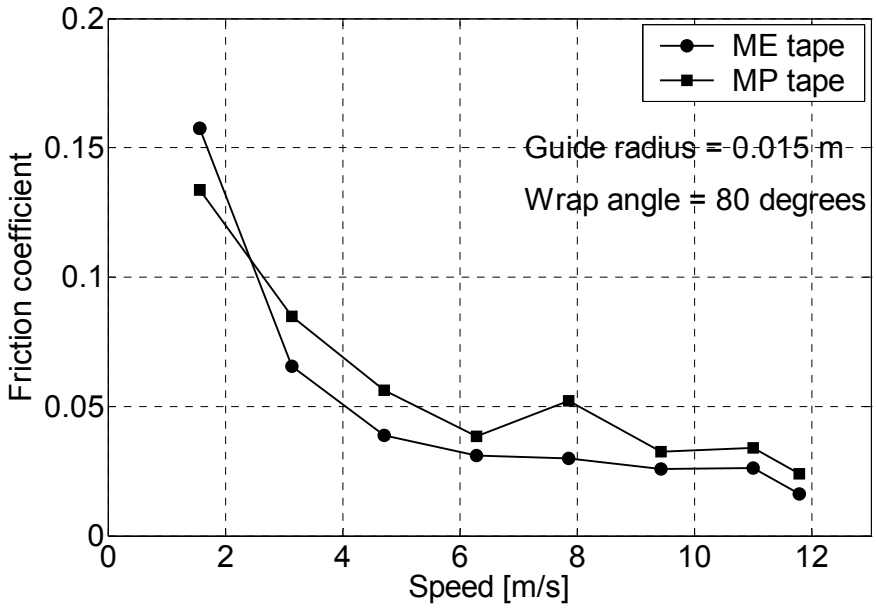

Fig. 5.9: Average friction coefficient versus speed for ME and MP tapes and a ceramic guide with a radius of 15 mm at a tape tension of 0.1 N

5.4.3 Model validation

The model derived in this chapter qualitatively predicts the effects of various design and operating parameters on the friction coefficient. In order to quantitatively correlate the theoretical and experimental results, it is desirable to use accurate material properties (E, Y and ν) of the tape/guide combinations. Because the MP magnetic coating consists of nano particles with a complex composition (cobalt-iron alloy core with a passivation shell composed of oxidized compounds of the core material [5.27]),

it is difficult to measure its material properties accurately and hence, the following average values were used: a) $E/Y = 100$, b) a yield strength $Y \cong 180\,\text{MPa}$ and c) Poisson ratio of 0.3.

Fig. 5.10 a) shows the experimentally measured (solid lines) and theoretically predicted (dashed lines) friction coefficient versus the tape speed for the rougher ceramic (C1) and the smoother anodized (C3) guide/tape (MP tape) combinations both with a radius $R = 15\,\text{mm}$, a tape tension $T_2 = 1\,\text{N}$ and a wrap angle $\theta = 90°$. Fig. 5.10 b) shows a similar comparison for a 7.5 mm ceramic guide/MP tape (C1) combination at two different tape tensions of 1 N and 0.5 N.

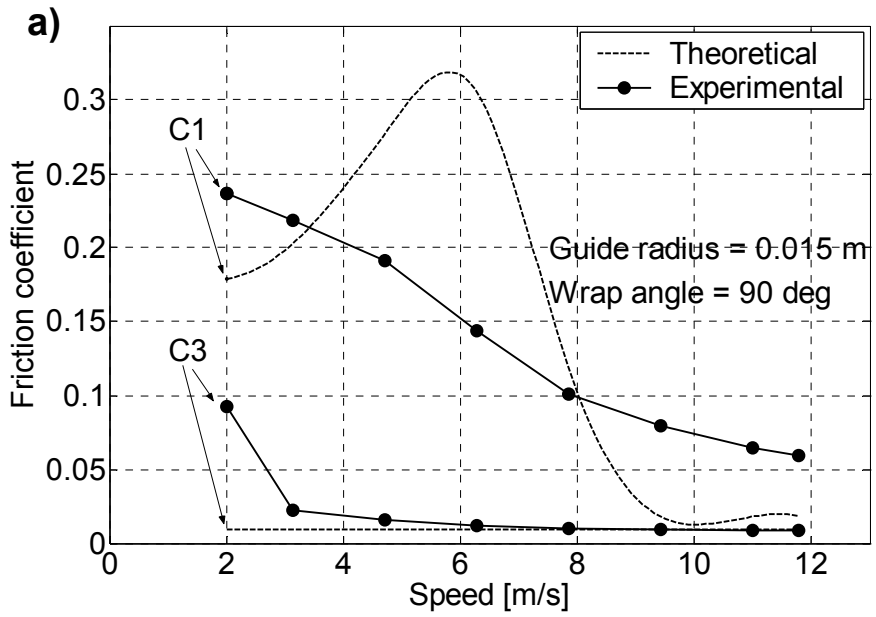

Fig. 5.10: Experimental and theoretical results for the average friction coefficient versus tape speed a) for MP tape and anodized (C3) and ceramic (C1) guides with radius of 15 mm at a tape tension of 1 N and b) for MP tape and a ceramic guide with radius of 7.5 mm at tape tensions of 1 N and 0.5 N

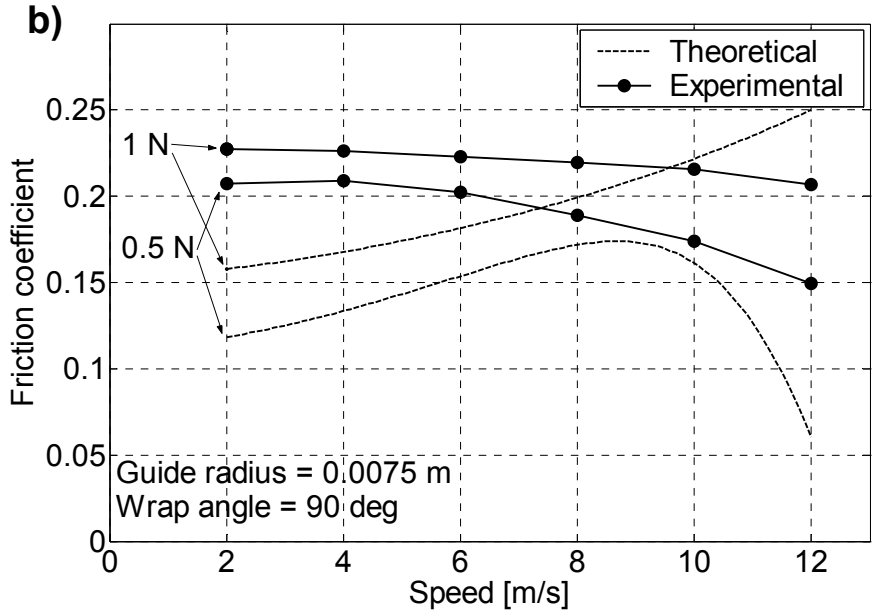

Fig. 5.10 continued: Experimental and theoretical results for the average friction coefficient versus tape speed a) for MP tape and anodized (C3) and ceramic (C1) guides with radius of 15 mm at a tape tension of 1 N and b) for MP tape and a ceramic guide with radius of 7.5 mm at tape tensions of 1 N and 0.5 N

We observe that the model predictions are of the same order of magnitude as the experimental results. The friction coefficient of the smoother anodized guide (see Table 5.1) is clearly much lower than that for the rougher ceramic guide at the same tape speed.

From Fig. 5.7 we note that the friction coefficient decreases monotonically with increasing speed. Full fluid lubrication begins when the friction coefficient versus speed curve shows a diminishing rate of decrease. According to Fig. 5.10 a) the flying speed

for C1 (ceramic guide) appears to be 9 m/s, while for C3 (anodized guide) it is 3 m/s. These values are in good agreement with the corresponding theoretical prediction of 8.5 and 2 m/s, respectively (See discussion of Fig. 5.4). From Fig. 5.10 b) very similar differences in the friction coefficient are seen for the two different tensions.

The monotonic reduction in the experimental friction coefficient with increasing speed in Figs. 5.10 a) and b) is not well captured by our model, which shows a behavior similar to that of the asperity load factor β versus $\bar{h}$ (see Fig. 5.2). This is probably due to the assumption of conformal tape having a uniform minimum spacing along the entire wrap angle. In reality, the tape/guide spacing will be larger than the minimum at the leading and trailing edges of the tape/guide interface. From Fig. 5.2 we can see that at low speeds (to the left of the maximum at $\bar{h} \approx 2.2$) an increased $\bar{h}$ will yield a higher load sharing factor β and hence will result in a higher Γ_2 and a higher predicted friction coefficient. At higher speeds (to the right of the maximum at $\bar{h} \approx 2.2$), an increased $\bar{h}$ will yield a lower load sharing factor β and hence will result in a lower predicted friction coefficient. Additionally, the assumption of a rigid tape may differ from reality and therefore may cause the theoretical results to deviate from the experimental results. Local deformations of the tape due to air bearing pressure and/or (partial) asperity contact might affect the friction coefficient. Also, we assumed that each asperity carries the same average load, despite the Gaussian distribution of asperity heights. Taking care of these effects could make the predicted results of friction coefficient versus speed closer to the experimental ones.

Fig. 5.11 compares theoretical predictions (dashed line) and experimental results (solid line) of the effect of the guide radius on the friction coefficient for a tape tension of 1 N and a ceramic guide/MP tape (C1) combination. As can be seen the agreement between the model and experiments is fairly good.

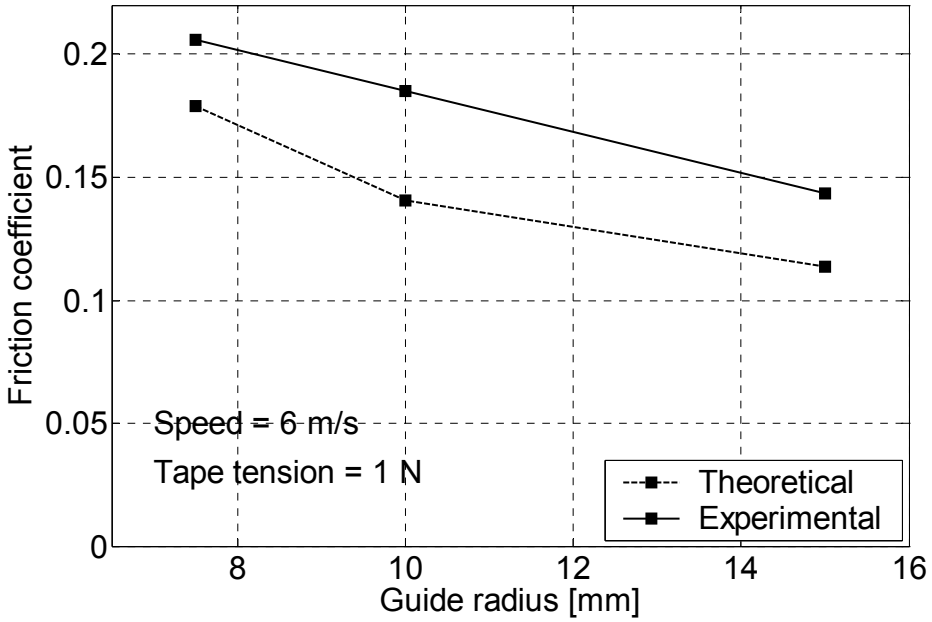

Fig. 5.11: Experimental and theoretical results for the average friction coefficient versus guide radius for a ceramic guide and MP tape at 1 N tape tension

5.5 Conclusion

A model was developed that predicts the local tape tension along the circumference of the tape/guide interface, based on a local friction coefficient model for a single contacting asperity. The model provides an average friction coefficient for different

tape/guide combinations taking into account the effects of tape sliding speed, tape and guide surface characteristics, material properties and guide dimensions. An experimental set-up was implemented to measure the average friction. Good agreement was found between theoretical predictions and the experimental results for moderate tape speeds where an air bearing coexists with partial asperity contact. The main conclusions of the present study are:

1. The classical belt drive equation that relies on a constant friction coefficient can be significantly improved to include such effects as sliding speed, surface roughness, material propertied and guide and tape geometry.
2. The plasticity index ψ, which is proportional to $(E/Y)(\sigma_s/r)^{1/2}$, has a significant effect on the average friction coefficient. A higher ψ value yields higher friction coefficients. The material properties ν and Y as well as the guide radius a also affect the friction coefficient.
3. The speed at the transition from boundary lubrication to full fluid film regime can be predicted from surface characteristics and from tape/guide flying height simulations. This speed is higher for rougher surfaces and smaller guide radii.
4. The average friction coefficient shows only a small dependence on the wrap angle, over the 80° - 100° range. However, it increases substantially for increasing dimensionless tape tension Γ_2, especially at high values of this parameter.
5. The average friction coefficient decreases for increasing speed and decreasing tape tension T_2.

6. The model can be further improved by relaxing some of its simplifying assumptions such as: rigid tape bulk and constant spacing between guide and tape.

5.6 Acknowledgements

Chapter 5, in part, is a reprint of the material as it appears in "The Influence of Operating and Design Parameters on the Magnetic Tape/Guide Friction Coefficient, Raeymaekers B., Etsion I., Talke F.E.", Tribology Letters, 2007. The dissertation author was the primary investigator and author of this paper.

5.7 Appendix

According to McCool's analysis [5.23], the spectral moments of a rough isotropic surface are given by

$$m_0 = AVG\left[y^2 \right] \tag{5.A1}$$

$$m_2 = AVG\left[\left(\frac{dy}{dx} \right)^2 \right] \tag{5.A2}$$

$$m_4 = AVG\left[\left(\frac{d^2 y}{dx^2} \right)^2 \right] \tag{5.A3}$$

where $y(x)$ is the height distribution of the surface profile.

The radius of curvature of asperity heights, the area density of the asperities and the standard deviation of asperity summit heights can be calculated as

$$r = 0.375\left(\frac{\pi}{m_4}\right)^{1/2} \tag{5.A4}$$

$$\eta = \frac{m_4}{6\pi\sqrt{3}m_2} \tag{5.A5}$$

$$\sigma_s = \left(m_0 - \frac{3.717\times10^{-4}}{\eta^2 r^2}\right)^{1/2} \tag{5.A6}$$

For the case of two contacting isotropic rough surfaces 1 and 2, an equivalent rough surface in contact with a smooth flat can be defined. The spectral moments of this equivalent rough surface are given by summing the spectral moments of the individual surfaces. Hence,

$$m_i = \left(m_i\right)_1 + \left(m_i\right)_2 \tag{5.A7}$$

where i=0, 2, 4

5.8 References

[5.1] Shigley JE, Mischke CR, 1989, Mechanical Engineering Design, 5th edition, McGraw Hill, New York

[5.2] Etsion I, Levinson O, Halperin G, Varenberg M, 2005, Experimental Investigation of the Elastic-Plastic Contact Area and Static Fricton of a Sphere on a Flat, J. Trib. T. ASME, Vol. 127, pp. 47 - 50

[5.3] Broese van Groenou A, 1990, On the Interpretation of Tape Friction, IEEE T. Mag., Vol. 26(1), pp. 144 - 146

[5.4] Osaki H, 2000, Flexible Media - Recent Developments from the Tribology Point of View, Tribol. Int., Vol. 33, pp. 377 - 382

[5.5] Osaki H, Endo T, 2005, Tribology in Helical Scan Drive Systems, Tribol. Int., Vol. 38, pp. 616 - 624

[5.6] Panda SP, Engelmann AP, 2003, Control and Operation of Reel-To-Reel Tape Drives without Tension Transducer, Microsyst. Technol., Vol. 10, pp. 53 - 59

[5.7] Taylor R, Talke FE, 2005, Investigation of Roller Interactions with Flexible Tape Medium, Tribol. Int., Vol. 38, pp. 599 - 605

[5.8] Bhushan B, 1984, Influence of Test Parameters on the Measurement of the Coefficient of Friction of Magnetic Tapes, Wear, Vol. 93, pp. 81 - 99

[5.9] Lacey C, Talke FE, 1992, Measurement and Simulation of Partial Contact at the Head/Tape Interface, J. Trib. T. ASME, Vol. 114, pp. 646 - 652

[5.10] Patir N, Cheng HS, 1978, Average Flow Model for Determining Effects of 3-Dimensional Roughness on Partial Hydrodynamic Lubrication, J. Lubr. Technol. T. ASME, Vol. 100(1), pp. 12 - 17

[5.11] Chang WR, Etsion I, Bogy DB, 1988, Static Friction Coefficient for Metallic Rough Surfaces, J. Trib. T. ASME, Vol. 110(1), pp. 57 - 63

[5.12] Tworzydlo WW, Cecot W, Oden JT, Yew CH, 1998, Computational Micro- and Macroscopic Models of Contact and Friction: Formulation, Approach and Applications, Wear, Vol. 220(2), pp. 113 – 140

[5.13] Amassad A, Shillor M, Sofonea M, 1999, A Quasistatic Contact Problem for an Elastic Perfectly Plastic Body with Tresca's Friction, Nonlinear Anal.-Theor., Vol. 35, pp. 95 - 109

[5.14] Alexandrov S, Richmond O, 2001, Couette Flows of Rigid/Plastic Solids: Analytical Examples of the Interaction of Constitutive and Frictional Laws, Int. J. Mech. Sci., Vol. 43, pp. 653 - 665

[5.15] Kogut L and Etsion I, 2004, A Static Friction Model for Elastic-Plastic Contacting Rough Surfaces, J. Trib. ASME, Vol. 126, pp. 34 - 40

[5.16] Brizmer V, Kligerman Y, Etsion I, 2007, Elastic-Plastic Contact under Combined Normal and Tangential Loading, Tribol. Lett., Vol. 25, pp. 61 - 70

[5.17] Brizmer V, Kligerman Y, Etsion I, 2006, The Effect of Contact Conditions and Material Properties on the Elasticity Terminus of a Spherical Contact, Int. J. Sol. Str., Vol. 43, pp. 5736 - 5749

[5.18] Rabinowicz E, 1965, Friction and Wear of Materials, J Wiley and sons, New York

[5.19] Greenwood JA, Williamson JBP, 1966, Contact of Nominally Flat Surfaces, Proceedings of the Royal Society of London Series A – Mathematical and Physical Sciences, Vol. 295 (1442), pp. 300 - 319

[5.20] Greenwood JA, Tripp JH, 1967, Elastic Contact of Rough Spheres, J. Appl. Mech. T. ASME, Vol. 34(1), pp. 153 - 159

[5.21] Kogut L and Etsion I, 2003, A Finite Element Based Elastic-Plastic Model for the Contact of Rough Surfaces, Tribol. T., Vol. 46, pp. 383 - 390

[5.22] Lacey C, Talke FE, 1990, A Tightly Coupled Numerical Foil Bearing Solution, IEEE T. Mag., Vol. 26(6), pp. 3039 - 3043

[5.23] McCool JI, 1987, Relating Profile Instrument Measurements to the Functional Performance of Rough Surfaces, J. Trib. T. ASME, Vol. 109, pp. 264 - 270

[5.24] Hempstock MS, Sullivan JL, 1996, The Durability and Signal Performance of Metal Evaporated and Metal Particle Tape, IEEE T. Mag., Vol. 32(5), pp. 3723 - 3725

[5.25] Hempstock MS, Sullivan JL, 1996, A Study of the Mechanical and Magnetic Performance of Metal Evaporated Tape, J. Mag. Mag. Mat., Vol. 155, pp. 323 - 328

[5.26] Bijker MD, Draaisma EA, Eisenberg M, Jansen J, Persat N, Sourty E, 2000, Future Directions in Advanced Digital Recording Technology, Tribol. Int., Vol. 33, pp. 383 - 390

[5.27] Personal communication

6. Enhancing tribological performance of the magnetic tape/guide interface by laser surface texturing

6.1 Introduction

Air-lubricated foil bearings are used in a variety of applications such as turbomachinery, journal bearings, dentistry equipment, etc. [6.1-6.3]. One of the most intricate applications of air-lubricated foil bearings can be found in magnetic tape drives [6.4], where a magnetic tape moves over a read/write head and tape drive components such as guides (stationary) and rollers (rotating). Friction is an important parameter in designing a tape transport for a commercial high performance tape drive. The overall friction force between tape and tape drive components determines the torque needed by the motor to drive the tape and affects the wear of the tape. Metal particulate (MP) tape is widely used in commercial tape recording systems since the tribological performance of the magnetically superior metal evaporated (ME) tape is inferior to that of MP tape.

Although friction between tape and tape drive components was observed to attenuate lateral tape motion [6.5-6.8], it is well known that tape drives with pressurized air bearing guides instead of rotating guides exhibit significantly lower LTM than tape drives with rotating guides [6.9]. Elimination of rotating tape drive components suppresses lateral tape motion due to run-out of those components. However, pressurized air bearing guides require an external compressor which is an obstacle for commercialization of this type of tape drive.

Based on the above information, it is therefore desirable to create an efficient self acting air bearing between the tape and the guide, thereby eliminating the need for an external compressor, while still benefiting from a low friction air bearing. In a recent study [6.10] (see also chapter 5), it was observed that for a tape tension of 1 N, a tape speed of at least 8 m/s was needed to achieve full fluid lubrication and hence, a low friction coefficient. This chapter explores the possibility of creating an efficient low speed air bearing between a magnetic tape and a cylindrical guide, thereby reducing the transition speed between boundary lubrication and full fluid lubrication regime, and thus expanding the speed range of low friction. We use a novel approach to tape guide design by using laser surface texturing (LST) of the guide surface. We have compared the tribological performance of the laser surface textured guide with various non-textured guides, thereby showing the benefits of textured guide surfaces.

6.2 Laser surface texturing

Laser surface texturing (LST) is a well established technique to create micro dimples on the surface of tribological components. These dimples act as micro-hydrodynamic bearings, thereby creating a local pressure increase between the sliding surfaces. This, in turn, increases the load carrying capacity for such bearings and reduces the friction coefficient for a constant load. The laser surface texturing technique has been successfully used in a number of applications, as, for instance, in the manufacturing of metal rolling cylinders with well-defined surface roughness [6.11] or the fabrication of laser bumps in the landing zone of a hard disk drive to facilitate

contact start/stop of the magnetic head [6.12]. It was, however, not until 1996 that LST was used in conventional lubrication situations as a method to reduce friction and optimize lubrication [6.13]. LST creates spherically shaped dimples on the surface by means of a material ablation process with a pulsed laser [6.14] and has now successfully been applied in reducing friction in various applications such as piston rings, mechanical seals and hydrodynamic seals [6.15-6.17]. The dimples also allow conducting heat from sliding interfaces and trapping of abrasive wear particles [6.18]. Hydrodynamic gas seals [6.19] and hard disk drive technology [6.20] are applications that are most relevant to the application of LST of the tape/guide interface.

No published investigations seem to exist about magnetic tape guide design in general or texturing of magnetic tape drive components in particular. This chapter fills this gap and investigates LST of magnetic tape guide surfaces in order to lower the transition speed between boundary lubrication and full fluid lubrication. This, in turn, reduces tape/guide friction and stiction, provides lower tape/guide wear and would potentially allow the use of ME tape by enhancing its tribological performance.

6.3 Experimental set-up

6.3.1 Apparatus

The same experimental set-up was used as explained in detail in Chapter 5.3.1 and illustrated in Fig. 5.3. The set-up simulates a moving tape on a stationary guide.

The wrap angle was 90 degrees for all experiments with MP tape and 45 degrees for all experiments with ME tape. The rotational speed of the guide in the clockwise direction is adjustable from 0 to 125 Hz, corresponding to a maximum circumferential speed of about 8 m/s for a guide with a radius of 10 mm. The measured force T_1 combined with the known "slack side" tension T_2 and the wrap angle θ enable calculation of the average friction coefficient μ from the ratio T_1 / T_2 and the classical belt/pulley equation, given e.g. in [6.21]

$$\frac{T_1}{T_2} = \exp(\mu\theta) \tag{6.1}$$

6.3.2 Test specimens

Commercially available metal particulate (MP) and metal evaporated (ME) magnetic tapes were used for the tests, identical to the tape specimens used in chapter 5.

A commercial tape drive roller, which was adapted to serve as a guide by removing its bearing, serves as reference case. The commercial guide is coated with ZrN (with

small percentages of Ni and W to increase the surface hardness). We compared the tribological performance of the commercial guide (reference) with an aluminum guide which was treated with LST. The laser surface texturing was applied on the guide with a 5 kHz pulsating Nd:YAG laser with a power of 11 kW and pulses of 30 ns duration and 4 mJ each (courtesy of Surface Technologies Ltd.). Fig. 6.1 shows a tape moving at a speed U over a laser surface textured guide. The LST guide consists of many dimples. The size of the dimples is exaggerated for the purpose of clarity.

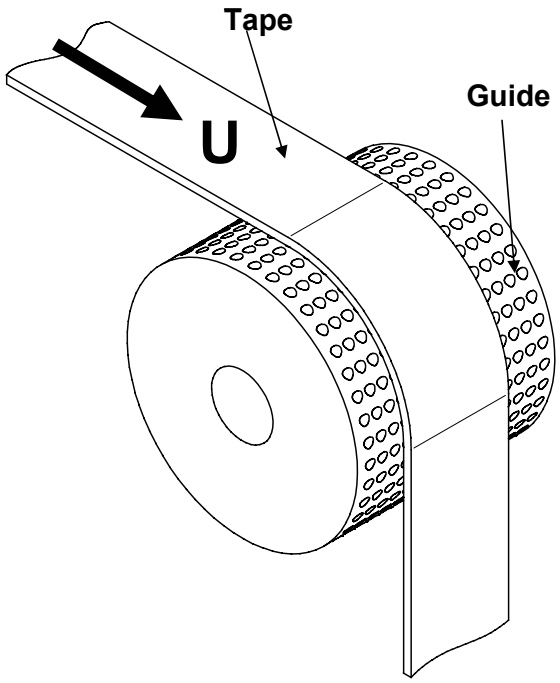

Fig. 6.1: Tape moving over a laser surface textured guide

Each of the dimples is characterized by the dimple aspect ratio $\varepsilon = h_p / 2r_p$. In Fig. 6.2, r_p denotes the radius of the dimple, h_p denotes the depth of the dimple, c is the tape/guide spacing and $h(x,y)$ is the local spacing between the guide surface and the magnetic tape. U is the linear speed of the rotating guide. The dimple density S_p expresses the ratio of the surface covered by dimples versus the total surface area.

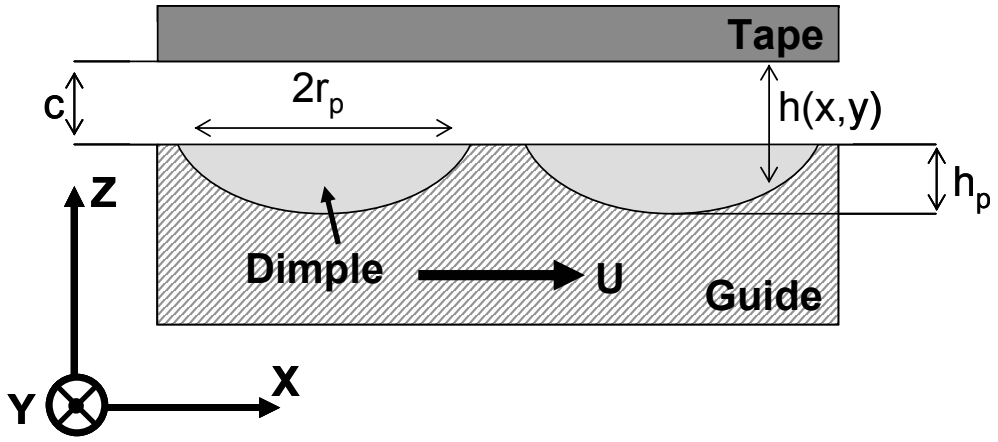

Fig. 6.2: Geometry of the dimples

The dimples are uniformly distributed over the guide surface. We used an LST guide characterized by the following parameters: a) a dimple density $S_p = 0.2$, b) a dimple radius $r_p = 50\,\mu\text{m}$ and c) a dimple depth $h_p = 2\,\mu\text{m}$. Fig. 6.3 shows a white light interferometer image (WYKO (Veeco), USA) of a dimpled surface. We also compared the reference case to the case of a ceramic coated guide and an aluminum anodized guide. All tested guides had a radius *a* of 10 mm.

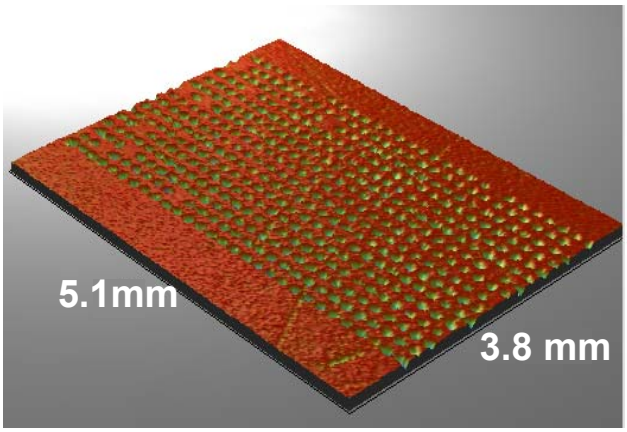

Fig. 6.3: White light interferometer image of dimpled surface

Atomic force microscopy (AFM) scans were used to determine the surface roughness of the different guides. The measurements showed that the surface roughness of the guides is isotropic. Hence, the Greenwood-Williamson approach can be used to describe their surface roughness [6.22].

Table 6.1 presents the average asperity tip radius r, the asperity density η, the standard deviation of asperity summit heights σ_s, the ratio σ_s / r and the dimensionless roughness parameter $\eta r \sigma_s$ for the individual tape samples and guides. The equivalent roughness parameters for two contacting rough surfaces [6.23] are also shown for eight different tape/guide combinations. These combinations are: a) ME tape in combination with the commercial tape drive guide (C1), b) MP tape in combination with the commercial tape drive guide (C2), c) ME tape in combination with a ceramic guide (C3), d) MP tape in combination with a ceramic guide (C4), e) ME tape and an

aluminum anodized guide (C5), f) MP tape and an aluminum anodized guide (C6), g) ME tape and an LST guide (C7) and h) MP tape and an LST guide (C8).

Table 6.1: Surface characteristics of the test specimens

	r [nm]	η [nm^{-2}]	σ_s [nm]	σ_s/r	$\eta r \sigma_s$
MP tape	5.55E+03	2.18E-06	5.34	9.62E-04	6.46E-02
ME tape	6.33E+03	2.80E-06	2.10	3.32E-04	3.72E-02
Ceramic	6.36E+02	6.08E-07	376.54	5.92E-01	1.46E-01
LST	1.79E+03	5.91E-07	76.81	4.29E-02	8.13E-02
Commercial	0.90E+03	3.64E-06	20.85	2.31E-02	6.83E-02
Anodized	2.17E+03	5.08E-07	70.72	3.26E-02	7.80E-02
C1	0.85E+03	3.69E-06	21.18	2.49E-02	6.64E-02
C2	0.85E+03	3.65E-06	21.77	2.56E-02	6.77E-02
C3	0.48E+03	7.00E-07	388.02	8.00E-01	1.32E-01
C4	0.48E+03	7.01E-07	388.06	8.01E-01	1.32E-01
C5	2.02E+03	5.44E-07	75.59	3.75E-02	8.29E-02
C6	1.98E+03	5.53E-07	75.77	3.83E-02	8.30E-02
C7	1.70E+03	6.29E-07	77.52	4.56E-02	8.29E-02
C8	1.68E+03	6.36E-07	77.70	4.63E-02	8.30E-02

The values in Table 6.1 were obtained using the three spectral moments m_0, m_2 and m_4 of the surface roughness as described by McCool [6.23] (see also [6.10]). The average radius of the asperity tips r, the asperity density η and the standard deviation of the asperity summit heights σ_s were calculated and averaged over 15 cross sections

of an AFM scan. From Table 6.1 we observe that the ratio σ_s / r for the commercial guide, the anodized guide and the LST guide is an order of magnitude smaller than for the ceramic guide, i.e., the surfaces of the commercial guide, the anodized guide and the LST guide are much smoother than the surface of the ceramic guide. We also observe that the ME tape is much smoother than the MP tape since its σ_s / r value is only one third of the other material combinations.

6.3.3 Test procedure

Exactly the same test procedure as discussed in chapter 5.3.3 was adopted for the experimental results described underneath. However, we did not apply the run-in procedure for the ME tape specimens, to avoid damage of the fragile magnetic coating by tape/guide contact. In addition, the "tight side" tension T_1 was measured for stepwise decrements of rotational speeds from 125 Hz down to 16 Hz. Thus, any damage of the coating at the lowest speed does not affect the measurements at higher speeds. These test series were repeated three times for each of the eight combinations C1 - C8, with a new tape specimen for each test. The calculated friction coefficient for each test was averaged over its three repetitions.

6.4 Experimental Results and Discussion

6.4.1 Metal particulate tape

Fig. 6.4 summarizes the results for the experiments with MP tape. These experiments include the commercial guide (C2), ceramic guide (C4), anodized guide (C6) and LST guide (C8), all with a guide radius of 10 mm. We have varied the nominal tape tension between 0.5 N and 1.2 N and observed similar behavior in terms of friction coefficient versus tape speed for all cases in that range. However, we observed that the friction coefficient increased with increasing tape tension, in agreement with the results in [10]. In this chapter, we only show results for a tape tension of 1 N, since this is the most commonly used nominal tape tension in state-of-the-art high performance tape drives. Fig. 6.4 shows the effect of sliding speed on the magnetic tape/guide friction coefficient calculated from eq. (1) for a wrap angle, θ, of 90 degrees.

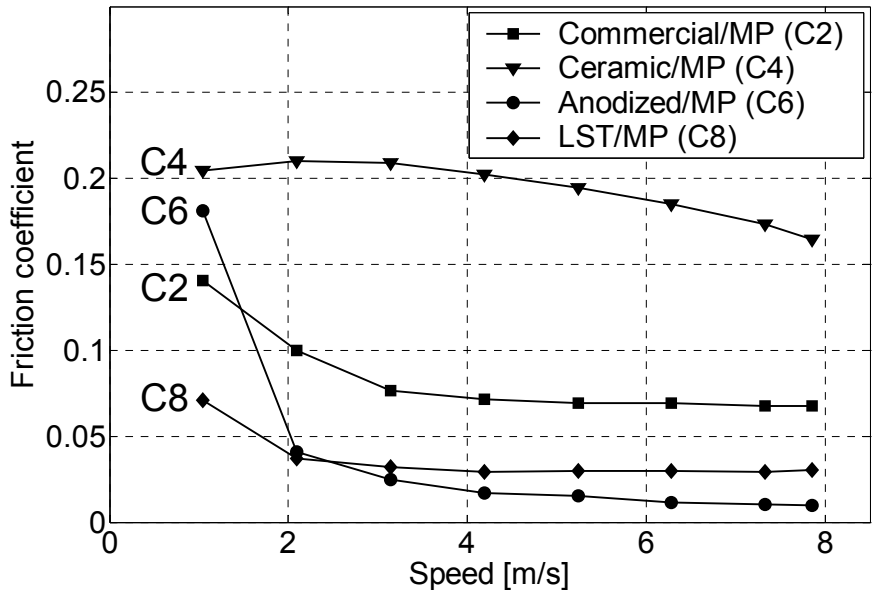

Fig. 6.4: Average friction coefficient versus speed for a tape tension of 1 N, wrap angle of 90 degrees and for a guide radius of 10 mm for combinations C2, C4, C6 and C8

From Fig. 6.4 we observe that for the case of the commercial guide (C2), the anodized guide (C6) and the LST guide (C8), the friction coefficient asymptotically approaches a very low values of about 0.075 (for the commercial guide), 0.01 (for the anodized guide) and 0.03 (for the LST guide), respectively. These low values are due to the formation of a (partial) air bearing at the tape/guide interface. We note that for the ceramic guide the friction coefficient only decreases from 0.21 at 1 m/s to 0.16 at 8 m/s and hence never reaches full fluid lubrication in the speed range of our experiments. It is justifiable to assume that full fluid lubrication exists if the tape/guide spacing c is $c \geq 3\sigma_s$ [6.24]. Since the ceramic guide has a much rougher surface than the other

guides (see Table 6.1), it is more difficult to obtain full fluid lubrication with this guide (see tape/guide spacing section).

The micro-dimples enhance the formation of an air bearing at low speeds and low tape/guide spacing since they increase the average pressure in the air bearing, compared to a non-textured guide surface. At higher speeds when full fluid lubrication has been established and the tape/guide spacing is larger, the influence of the micro-dimples becomes less significant. It is interesting to note that in the full fluid lubrication regime in Fig. 6.4 a certain correlation seems to exist between the friction coefficient and the dimensionless roughness parameter $\eta r \sigma_s$, i.e., the friction coefficient decreases as $\eta r \sigma_s$ increases (see Fig. 6.4 and Table 6.1).

At a low speed of 1 m/s, the LST guide (C8) has a friction coefficient of 0.07, while the reference commercial guide (C2) has a friction coefficient of 0.14, the anodized guide (C4) has a friction coefficient of 0.18 and the ceramic guide (C6) has a friction coefficient of 0.21. Thus, at low speeds (boundary lubrication) the LST guide outperforms all other guides and has the lowest friction coefficient.

6.4.2 Metal evaporated tape

In order to increase the recording density, tape manufacturers have introduced metal evaporated (ME) tape, where a high coercivity cobalt film is evaporated and deposited on the tape polymeric substrate in a vacuum chamber. The tribological performance and

reliability of ME tape is inferior compared to MP tape [6.25-6.27], as already mentioned in chapter 5.4.2. The use of wear protective coatings such as diamond like carbon (DLC) or a so-called super protective layer (SPL) has been used to improve the wear characteristics of ME tape [6.28]. Osaki [6.29] pointed out that the magnetic layer of ME tapes is peeled off by increased friction force due to adhesive wear and the relative motion between the tape and the tape drive components. He emphasized the necessity of reducing the friction coefficient between ME tape and tape drive components to increase durability and reliability.

All of the four different guides of our test set-up stalled due to high stiction when attempting to test the ME tape over the full speed range with a guide radius of 10 mm, a wrap angle of 90 degrees and a tape tension of 1 N, i.e., parameters which were previously used with MP tape. Under these conditions the ME tape showed a tendency to “stick” to the guide. To get a complete comparison of the tribological performance for the different guides with the ME tape, we decreased the tape tension to 0.7 N and lowered the wrap angle to 45 degrees to reduce the friction force [6.10]. Fig. 6.5 presents the results for the experiments with ME tape. These experiments include the commercial guide (C1), the ceramic guide (C3), the anodized guide (C5) and the LST guide (C7), all with a guide radius of 10 mm, a wrap angle of 45 degrees and a tape tension of 0.7 N.

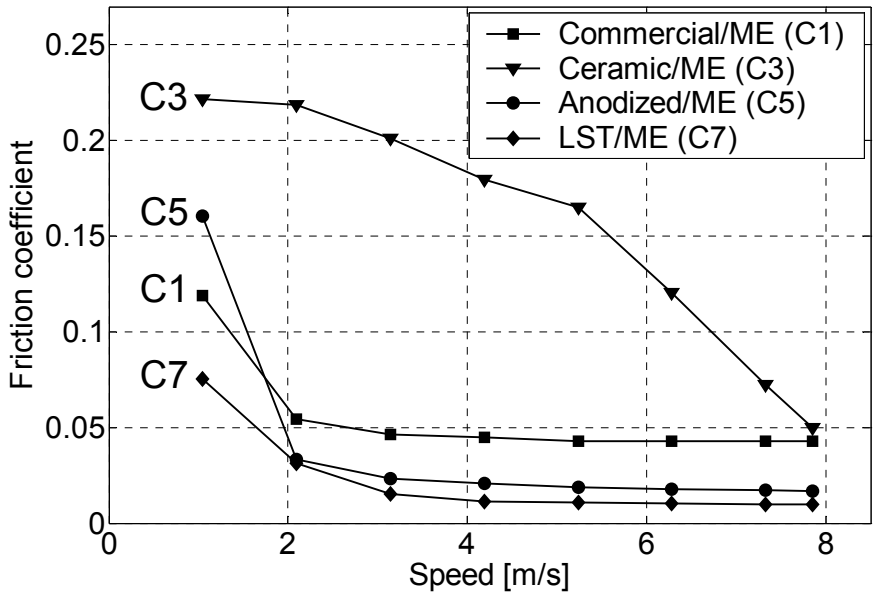

Fig. 6.5: Average friction coefficient versus speed for ME tape with a tape tension of 0.7 N, wrap angle of 45 degrees and a guide radius of 10 mm for the combinations C1, C3, C5 and C7

We observe from Fig. 6.5 that the ceramic guide (C3) has a high friction coefficient, which is highly dependent on the speed. At 1 m/s the friction coefficient for this guide is almost 0.23, while at 8 m/s it is about 0.05, due to the formation of a (partial) air bearing. The friction coefficient of the commercial guide (C1) approaches 0.04 at 2 m/s and is about 0.13 at 1 m/s. The LST (C7) and anodized (C5) guides are similar at speeds higher than 3 m/s, with a friction coefficient approaching 0.01 (note in Table 6.1 the very similar $\eta\sigma_s r$ values for these two combinations). At 1 m/s, the friction coefficient is about 0.07 for the LST guide and 0.16 for the anodized guide. Again, except for the ceramic guide, all guides reach full fluid lubrication just above 2 m/s (see tape/guide spacing section).

Fig. 6.5 (guides with ME tape) and Fig. 6.4 (guides with MP tape) reveal the same trend. The ceramic guide has the highest friction coefficient and its friction coefficient is highly dependent on speed. The commercial guide has a slightly higher friction coefficient in the full fluid lubrication regime than the anodized and the LST guides, which may again be explained by lower roughness parameter $\eta\sigma_s r$ of the commercial guide with respect to the anodized and LST guides (see Table 6.1). In the boundary lubrication regime, the LST guide yields a remarkably low friction coefficient because of its dimpled surface and increased air bearing pressure. This very promising result indicates that the use of ME tape in high performance commercial tape drives could possibly be facilitated with the use of LST guides in the tape path.

The friction coefficient of the LST guide depends less on speed than any of the other tested guides. This is true for both ME and MP tapes. This phenomenon is highly desirable in commercial tape drives since the interaction of the magnetic tape with other tape drive components does not change while the drive is ramping up to operational speed or ramping down to standstill. Hence, the number of start/stop cycles would not affect the wear of the tape, since the friction coefficient is independent of the speed. It should be noted, however, that a direct comparison between Fig. 6.4 and Fig. 6.5 must be made with care since the experiments of Fig. 6.5 were conducted under modified conditions (45 degrees wrap angle and 0.7 N tape tension), i.e., stiction effects were eliminated by reducing the friction force between tape and guide.

6.4.3 Tape/guide spacing

In the literature, simple curve fit formulas are available that neglect bending stiffness to predict the tape/guide spacing [6.30]. In our work, we have used the more involved approach discussed in [6.31] (see also [6.10]) that includes bending stiffness in the calculation of the tape/guide spacing. We have found that for a smooth guide of radius 10 mm, a tape tension of 1 N and a wrap angle of 90 degrees, the tape/guide spacing yields 0.163 μm at a tape speed of 1 m/s, 0.2 μm at 2 m/s and 0.55 μm at 8 m/s. Hence, it is clear that full fluid lubrication cannot be established for the ceramic guide at speeds below 8 m/s, since $c < 3\sigma_s$ for this guide (see Table 6.1). All other guide/tape combinations will reach full fluid lubrication at a speed slightly above 2 m/s. For the case of a smooth guide of radius 10 mm, a tape tension of 0.7 N and a wrap angle of 45 degrees, the tape/guide spacing yields 0.15 μm at a tape speed of 2 m/s and 0.53 μm at a tape speed of 8 m/s. Hence, full fluid lubrication cannot be established for the ceramic guide at speeds below 8 m/s, since again $c < 3\sigma_s$ for this guide. All other guide/tape combinations will reach full fluid lubrication at a speed just above 2 m/s.

To emphasize the benefit of LST guides at the lowest speed, we have normalized the friction coefficient at a speed of 1 m/s with respect to the relevant commercial guide reference case. In particular, we have used C1 for ME tapes and C2 for MP tapes. Fig. 6.6 shows the normalized average friction coefficient for the eight tape/guide combinations C1-C8.

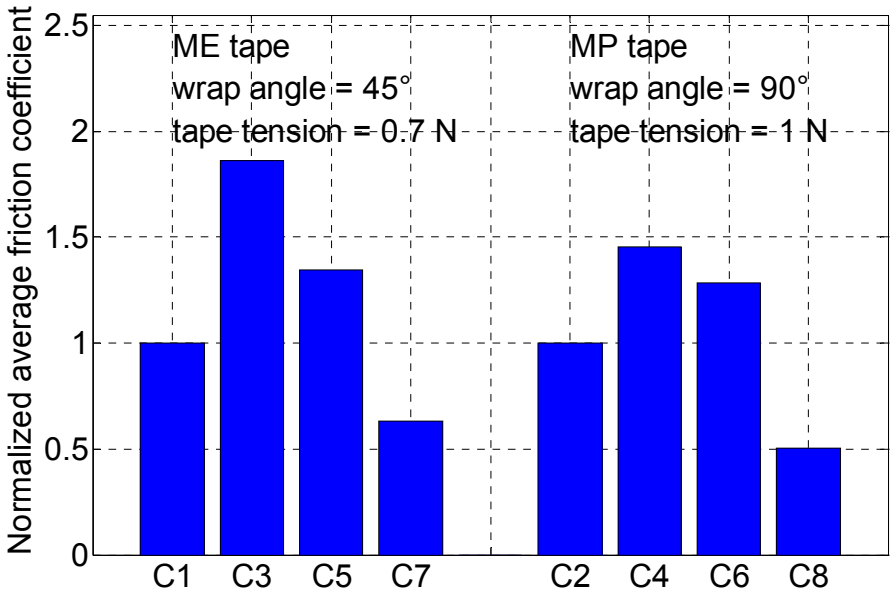

Fig. 6.6: Normalized average friction coefficient for ME and MP tapes with the different guides at a speed of 1 m/s

It was pointed out earlier that the ME and MP experiments are not directly comparable due to their different test parameters. However, we observe clearly that the combinations of LST guide and ME and MP tape, C7 and C8, respectively, yield the lowest friction coefficient of all combinations at a speed of 1 m/s. Compared to the reference case C1, the LST case C7 lowers the friction coefficient by 40 %. Compared to the reference case C2, the LST case C8 provides a 50 % lower friction coefficient. The anodized and ceramic guides yield higher friction coefficients than their respective reference case at 1 m/s for both ME and MP tapes.

6.5 Conclusion of the experimental analysis

1. Laser Surface Textured (LST) guides reduce the friction coefficient between tape and guide, compared to tested commercial and ceramic guides.
2. LST reduces the influence of speed on the friction coefficient. The critical speed where boundary lubrication regime changes into full fluid lubrication decreases significantly for LST guides.
3. Metal evaporated (ME) tape was used successfully in combination with an LST guide at a nominal tape tension of 0.7 N, and wrap angle of 45 degrees even at a tape speed as low as 1 m/s. At this low speed the ME tape tends to "stick" to all other guides (anodized, commercial and ceramic).

6.6 Theoretical model

To better understand the effect of a textured guide surface on the tribological performance of the tape/guide interface, we have simulated the pressure distribution between the tape and the guide surface for a column of ten dimples. We made the following assumptions:

1. The tape is considered rigid. Local elastic deformations of the tape are neglected. This assumption implies that no elasto-hydrodynamic effects are taken into account.
2. The tape is assumed to be conformal to the guide [6.30]. This case is identical to a parallel slider bearing. One-dimensional foil bearing simulations [6.31] show

that the tape is indeed conformal to a smooth guide over 95 percent of the interface length.

3. The shape of all dimples is identical and spherical.
4. The gas in the air bearing is compressible and has a constant viscosity.
5. The air bearing is assumed to be infinitely wide, i.e., side flow effects are neglected. Hence, one column of dimples is representative of the whole air bearing surface, when a periodic boundary condition is applied in the direction perpendicular to the flow.
6. The model is only valid for the hydrodynamic lubrication regime. No asperity contact is allowed.

According to assumption 1, the guide and magnetic tape are separated by a uniform air film of thickness c. It should be noted that in reality the tape is flexible, i.e., simultaneous solution of the Reynolds equation along with the tape elasticity equation is required. However, the assumption of a rigid tape allows a first order approximation of the physical situation without the need for extended numerical solutions.

The effects of the curvature of the cylindrical surface can be neglected in the model, since the minimum tape/guide spacing c is much smaller than the guide radius. Additionally, we assume full fluid film lubrication and therefore require $c \geq 3\sigma_s$ [6.24].

The dimples are uniformly distributed over the guide surface and each dimple is contained within an imaginary square cell of length $2r_1$. Fig. 2 shows one dimple with radius r_p, positioned at the center of the imaginary cell. We have defined a local Cartesian coordinate system x^*y^* with origin at the center of the imaginary cell.

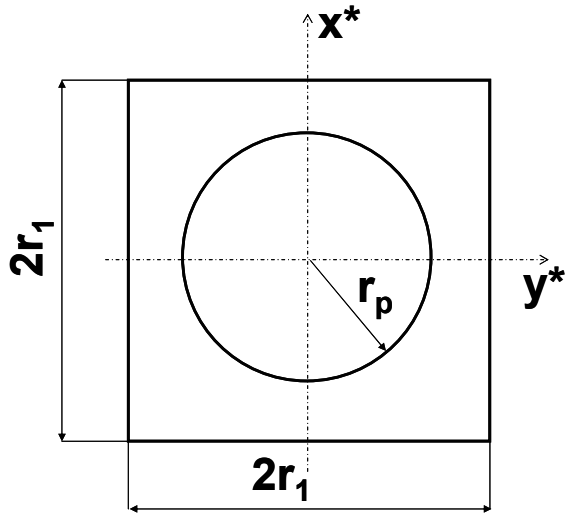

Fig. 6.7: Single dimple within its imaginary cell (local coordinates)

The cell length r_1 can be expressed as a function of the dimple area density S_p, and the dimple radius r_p, as

$$r_1 = \frac{r_p}{2}\sqrt{\frac{\pi}{S_p}} \tag{6.2}$$

Fig. 6.8 a) shows the distribution of the dimples on the guide surface in a global Cartesian xy coordinate system. Each column of dimples is parallel to the x-axis and can be modeled as shown in Fig. 6.8 b).

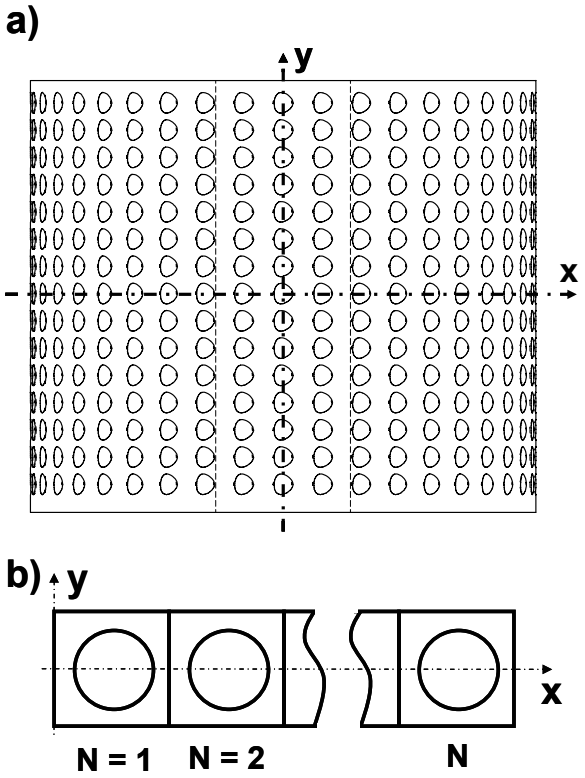

Fig. 6.8: a) Dimple distribution and b) a single column of dimples (global coordinates)

The two dimensional, steady-state compressible Reynolds equation, which relates the pressure distribution to the spacing at the tape/guide interface [6.19], is given by

$$\frac{\partial}{\partial x}\left(ph^3 \frac{\partial p}{\partial x} \right) + \frac{\partial}{\partial y}\left(ph^3 \frac{\partial p}{\partial y} \right) = 6\mu_a U \frac{\partial (ph)}{\partial x} \tag{6.3}$$

where x and y represent coordinates in a global Cartesian coordinate system, $p(x,y)$ is the air bearing pressure, μ_a is the dynamic viscosity of air and $h(x,y)$ is the clearance between tape and guide. Because the tape/guide spacing is much larger than the mean free path of air, rarefaction effects are neglected.

For the analysis of the textured surface, it is convenient to introduce the following non-dimensional expressions:

$$X = \frac{x}{r_p},\ Y = \frac{y}{r_p},\ P(X,Y) = \frac{p(x,y)}{p_a},\ H(X,Y) = \frac{h(x,y)}{c}\ , \tag{6.4}$$

where X and Y denote the non-dimensional (global) coordinates, and P and H denote the non-dimensional pressure and spacing, respectively. The normalizing pressure p_a is the atmospheric pressure. The dimensionless local spacing H^* as a function of the dimensionless local coordinates X^*, Y^* for one cell shown in Fig. 6.2 is given by [6.32]:

$$H^*(X^*,Y^*) = 1\ , \qquad \text{for } X^{*2} + Y^{*2} > 1$$

$$H^*(X^*,Y^*) = 1 + \sqrt{\left(\frac{\varepsilon}{2\delta} + \frac{1}{8\varepsilon\delta}\right)^2 - \left(X^{*2} + Y^{*2}\right)\frac{1}{4\delta^2}} - \left(\frac{1}{8\varepsilon\delta} - \frac{\varepsilon}{2\delta}\right), \text{ for } X^{*2} + Y^{*2} \le 1 \tag{6.5}$$

where $\varepsilon = h_p / 2r_p$ is the aspect ratio of the dimple and $\delta = c / 2r_p$ is the dimensionless tape/guide minimum spacing.

To create a column of dimples of identical shape (see Fig. 6.8 b)), we expand the dimensionless height distribution for a single cell, $H^*\left(X^*,Y^*\right)$, to a column of $N=10$ cells by repeating the height distribution for a single cell for each cell in the column. The dimensionless Reynolds equation in the global coordinate system can then be expressed as

$$\frac{\partial}{\partial X}\left(PH^3\frac{\partial P}{\partial X}\right)+\frac{\partial}{\partial Y}\left(PH^3\frac{\partial P}{\partial Y}\right)=\frac{\lambda}{\delta^2}\frac{\partial\left(PH\right)}{\partial X} \tag{6.6}$$

where $\lambda=3\mu_a U/2r_p p_a$ and $\delta=c/2r_p$.

The following boundary conditions are assumed. The pressure is atmospheric at the inlet and outlet of the tape/guide interface. In addition, the pressure is periodic in the direction perpendicular to the air flow (Y-direction). Multiple columns of dimples next to one another will yield a periodic pressure distribution. The period is defined by the size of the imaginary cell ($2r_1$). The boundary conditions can be expressed as

$$\begin{aligned} &P(X=0,Y)=1 \\ &P(X=N\frac{2r_1}{r_p},Y)=1 \\ &\frac{\partial P}{\partial Y}(X,Y=-\frac{r_1}{r_p})=\frac{\partial P}{\partial Y}(X,Y=\frac{r_1}{r_p})=0 \end{aligned} \tag{6.7}$$

where N is the number of cells in a column (see Fig. 6.8 b)). Eq. (6.6) can be solved for the pressure distribution if the dimensionless spacing $H\left(X,Y\right)$ and the dimensionless parameters λ, δ and ε are specified. A "staggered grid" finite

difference approach [6.33] was used to solve eq. (6.6) with the boundary conditions specified in eq. (6.7) for a non-dimensional local spacing distribution given by eq. (6.5). A grid of 200 by 200 nodes per cell was chosen based on convergence requirements. Because of symmetry with respect to the X-axis, it is only necessary to solve for half the imaginary cell. An over-relaxation factor of $\gamma = 1.4$ was used to obtain a faster convergence of the pressure distribution.

6.7 Results and discussion

6.7.1 Air bearing pressure

Fig. 6.9 a) depicts the cross section of the column of dimples along the X-axis (see Fig. 6.8 b)), normalized by r_p. The horizontal and vertical scales in Fig. 6.9 a) are uneven, resulting in the distorted appearance of the dimple shape. Fig. 6.9 b) shows the dimensionless pressure distribution along the X-axis, for a column of $N = 10$ cells and values of $\lambda = 2.14E-5$, $\delta = 0.002$, $\varepsilon = 0.01$ and $S_p = 0.15$.

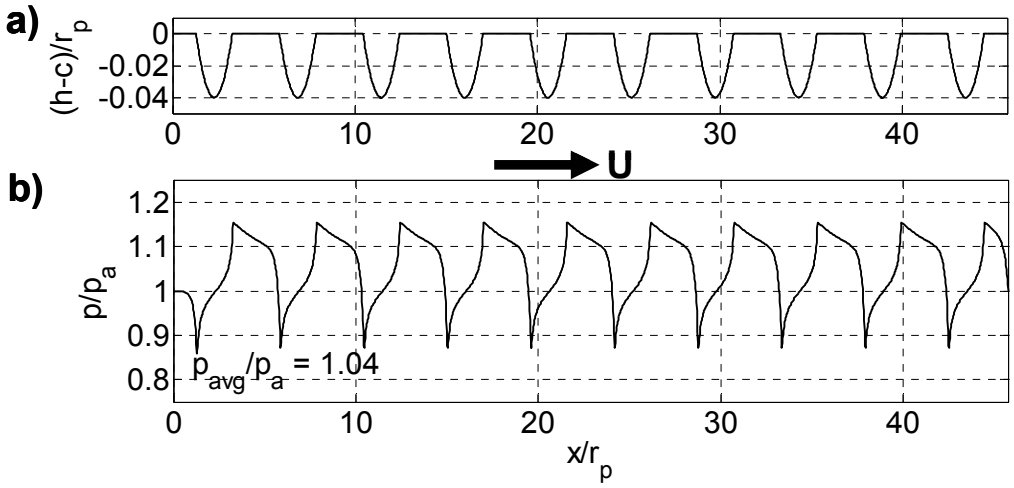

Fig. 6.9: a) Cross-sectional view of the column of dimples and b) Dimensionless pressure distribution along the X-axis for a column of N=10 dimples

The direction of the flow (tape speed U) has been indicated in Fig. 6.9. From Fig. 6.9 b) we observe that the pressure at the inlet of a dimple (with reference to the direction of the flow) becomes sub-ambient, because the local spacing between the tape and guide increases. When the flow passes the midpoint of the dimple, the spacing decreases and thus, the pressure increases. The pressure distribution is non-symmetric over the dimple region, i.e., the net effect of the dimples is an increased average air bearing pressure p_{avg}, which is greater than the atmospheric pressure p_a, i.e., $p_{avg} / p_a > 1$. Without dimples, the dimensionless pressure $p_{avg} / p_a = 1$, equivalent to the parallel slider case. The increased pressure p_{avg} will increase the load bearing capacity and spacing between the tape and the guide for a fixed tape tension and speed. In other words, for a dimpled guide surface, the transition from boundary lubrication to hydrodynamic lubrication occurs at a lower tape speed than in the case of a smooth guide. We point out that a single column of five to ten consecutive dimples is

representative of the entire dimpled surface. As observed in Fig. 6.9, the pressure profile becomes identical for each dimple, except for the first two dimples at the inlet and outlet of the column. Therefore, the simulation of just one column of ten dimples is a valid representation for the effects of a complete textured surface.

6.7.2 Optimization of dimple geometry

The dimensionless parameters S_p, ε, δ and λ define the dimple area density, dimple aspect ratio, the dimensionless minimum spacing between tape and guide and the flow parameter, respectively. Table 6.2 shows a typical reference case along with the range of variation of the dimple depth and tape/guide spacing as well as the corresponding dimensionless parameters. The atmospheric pressure p_a was taken to be 0.1 MPa and the viscosity of air $\mu_a = 1.81E-5$ Pas. The typical standard deviation of asperity summit heights in commercial tape/guide contacts is on the order $\sigma_s = 30$ nm. This number is the equivalent roughness of the mating tape and guide surfaces, see McCool [6.23]. The assumption of full fluid film lubrication, $c \geq 3\sigma_s$ [6.24], requires the minimum tape/guide spacing c to be larger than 100 nm. The dimple radius was selected to be $r_p = 50$ μm for ease of manufacturing.

Table 6.2: Range of the dimensional and dimensionless parameters

Parameter	Minimum	Reference	Maximum
h_p [μm]	0.3	1	5
c [nm]	100	200	400
ε	0.003	0.01	0.05
δ	0.001	0.002	0.004
λ	5E-06	2E-05	3E-05

In the following, we use our model to numerically investigate how these parameters can be chosen to yield the highest possible average air bearing pressure between the conformal tape and the guide. A maximized average air bearing pressure will yield the highest load carrying capacity and hence, the highest tape/guide spacing for a given tape tension.

Fig. 6.10 shows the dimensionless average air bearing pressure p_{avg} / p_a versus the dimple density S_p for different values of the dimple aspect ratio ε and for the reference values $\delta = 0.002$ and $\lambda = 2E-5$.

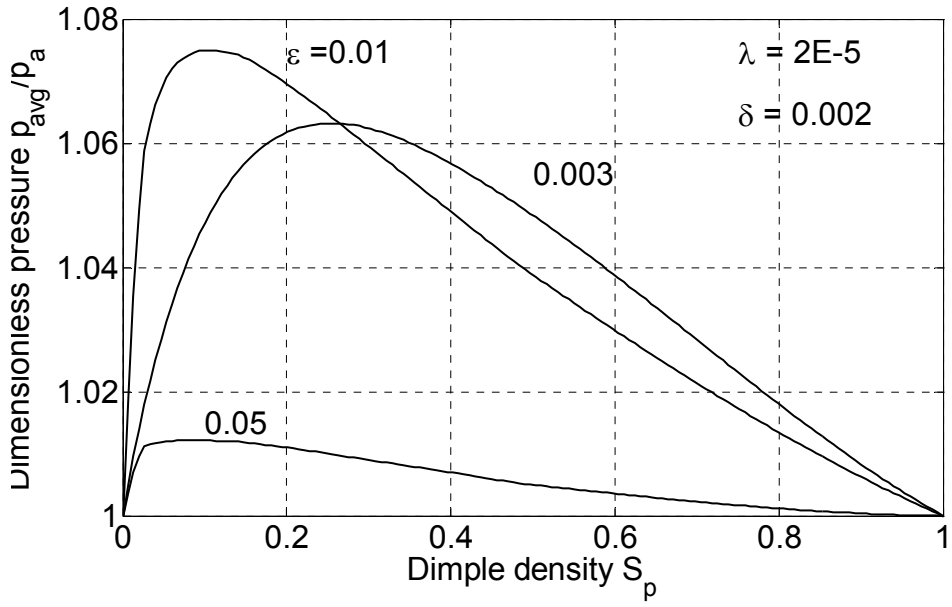

Fig. 6.10: Dimensionless average air bearing pressure, p_{avg}/p_a versus dimple density S_p

Since the guide surface is smooth (parallel slider bearing) for both of the extreme dimple densities $S_p = 0$ and $S_p = 1$, an optimum density must exist which yields the highest average air bearing pressure p_{avg} / p_a. From Fig. 6.10 we observe that the optimum S_p occurs for values from 0.10 to 0.30 depending on the dimple aspect ratio ε. We note that the optimum dimple density shifts towards lower values for an increasing dimple aspect ratio ε. Hence, when the dimple aspect ratio is increased, fewer dimples per unit surface are needed to obtain the maximum dimensionless air bearing pressure for that specific dimple aspect ratio. We also found that the dimensionless tape/guide minimum spacing δ does not affect the optimum dimple

density. Additionally, it is clear from Fig. 6.10 that an optimum dimple aspect ratio exists in the range $0.003 \le \varepsilon \le 0.05$.

Fig. 6.11 a) shows the dimensionless pressure versus the dimple aspect ratio for different values of the dimensionless spacing δ and for $\lambda = 2\times10^{-5}$ and a dimple density $S_p = 0.15$. Fig. 6.11 b) shows the dimensionless pressure versus the dimple aspect ratio for different values of the parameter λ and for $\delta = 0.002$. For a given ε and for a constant atmospheric pressure p_a, dimple radius r_p and air viscosity μ_a, the flow parameter λ depends only on the tape speed U.

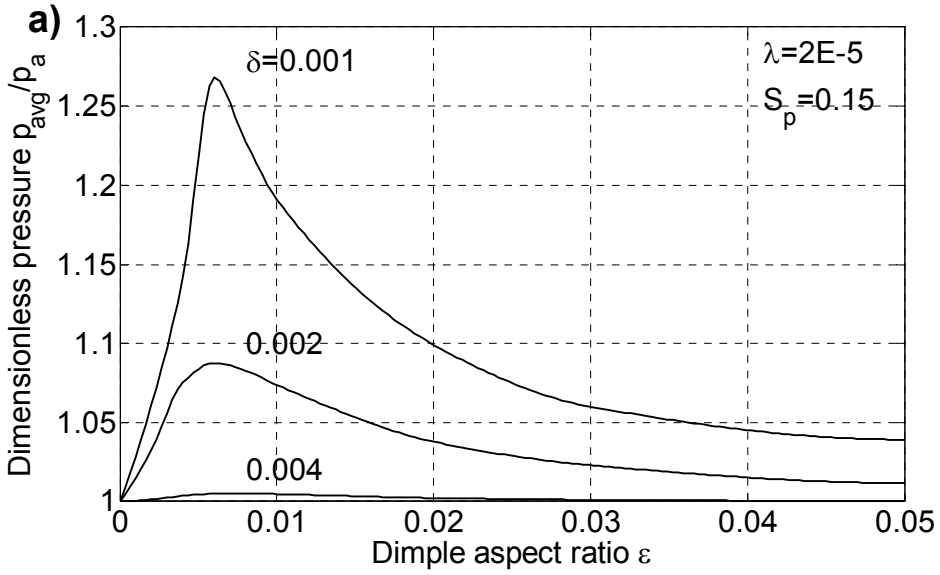

Fig. 6.11: Dimensionless average air bearing pressure versus dimple aspect ratio for a) different dimensionless spacing values and b) different values of λ

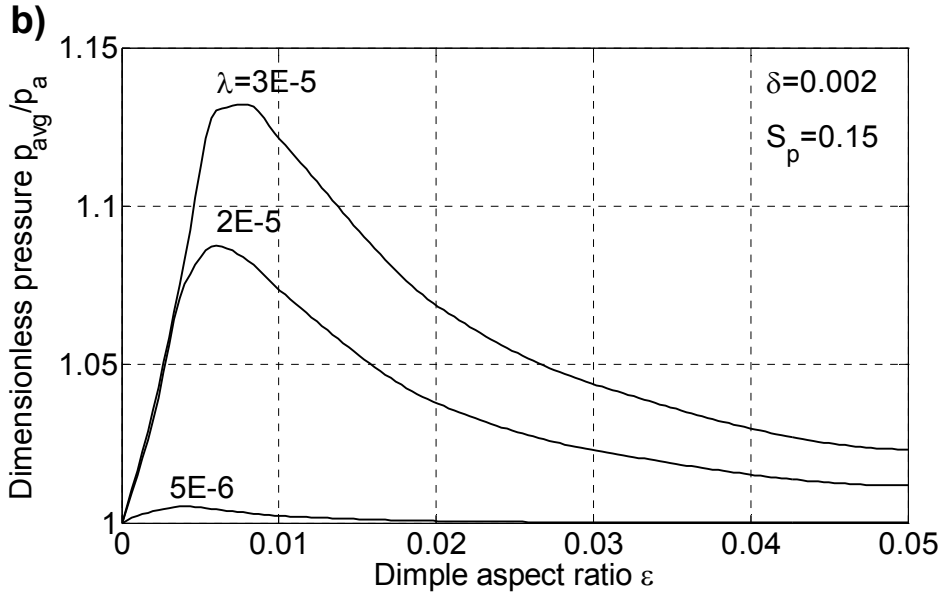

Fig. 6.11 continued: Dimensionless average air bearing pressure versus dimple aspect ratio for a) different dimensionless spacing values and b) different values of λ

From both Fig. 6.11 a) and b) we observe that the optimum value for the dimple aspect ratio ε is approximately 0.006 regardless of δ or λ. For instance, if the dimple radius $r_p = 50$ μm, we observe that the optimal value of the dimple depth $h_p = 0.6$ μm. From Fig. 6.11 a) and b) we also note that the dimensionless average air bearing pressure increases for decreasing δ and for increasing tape speed U (increasing λ), as would be expected.

Fig. 6.12 shows the dimensionless average pressure p_{avg} / p_a versus the dimensionless spacing $\delta = c / 2r_p$ for different values of the dimple aspect ratio ε and for $S_p = 0.15$ and $\lambda = 2E-5$.

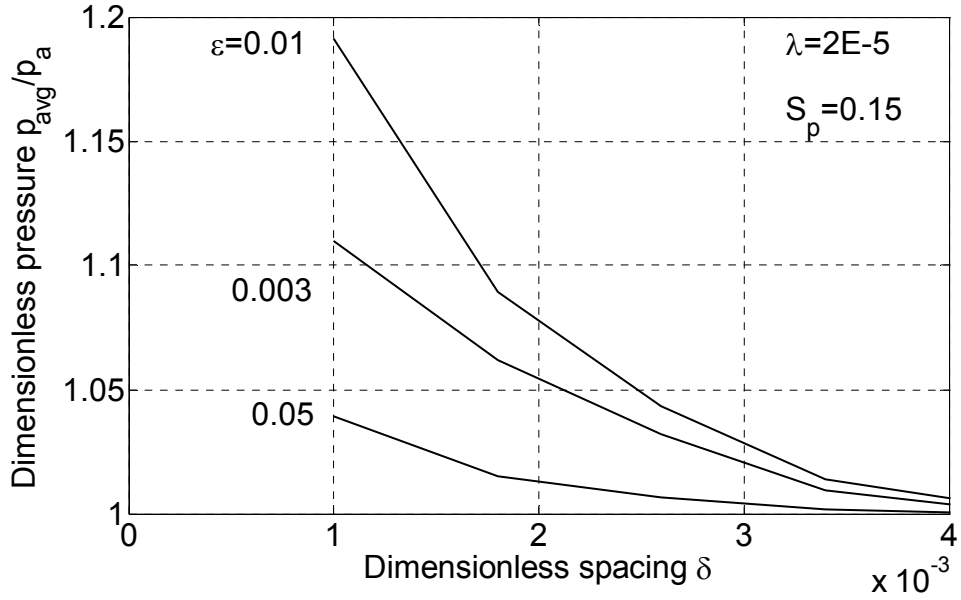

Fig. 6.12: Dimensionless average air bearing pressure versus dimensionless spacing for different dimple aspect ratios

The results are shown for $\delta \geq 0.001$ only, corresponding to full fluid lubrication. We observe a sharp increase in the dimensionless pressure for decreasing values of δ, which corresponds to decreasing tape/guide spacing.

Finally, Fig. 6.13 shows the optimum combination of dimple density and dimple aspect ratio, for different values of the dimensionless tape/guide minimum spacing and for $\lambda = 2E-5$.

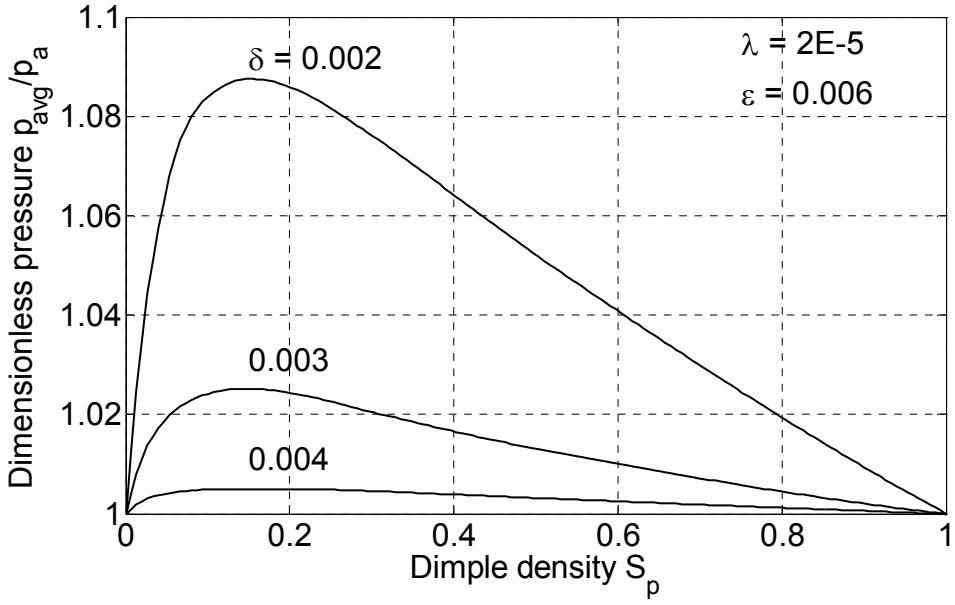

Fig. 6.13: Dimensionless average air bearing pressure versus dimple density S_p, for the optimum dimple aspect ratio

We observe that for the optimum dimple aspect ratio $\varepsilon = 0.006$ and the optimum dimple density $S_p = 0.15$, the dimensionless pressure reaches a maximum value of approximately 1.09 for $\delta = 0.002$ and $\lambda = 2E-5$. This number represents the maximum dimensionless average pressure that can be obtained, according to our simplified model.

6.7.3 Friction

When neglecting the tape bending stiffness, the equilibrium between the tape tension per unit tape width, T, and the air bearing pressure requires that [6.34]

$$p_{avg} - p_a = T / R, \tag{6.8}$$

for a guide with radius R. Non-dimensionalizing eq. (6.8) with the atmospheric pressure p_a yields

$$p_{avg} / p_a - 1 = T / (p_a R) \tag{6.9}$$

Fig. 6.14 shows the dimensionless tape/guide spacing δ versus the dimple aspect ratio ε for different values of the dimensionless tape tension $T / (p_a R)$ (dimple density $S_p = 0.15$ and flow parameter $\lambda = 2E - 5$). The results shown in Fig. 6.14 were obtained from $p_{avg} / p_a = f(\delta)$ curves as shown in Fig. 6.12. The intersection of these curves with horizontal lines for $p_{avg} / p_a = constant$ yields values of δ for each ε-curve. The dimensionless average air bearing pressure was then converted to a dimensionless tape tension by eq. (6.9). To obtain Fig. 6.14, we considered more values of ε than displayed in Fig. 6.12.

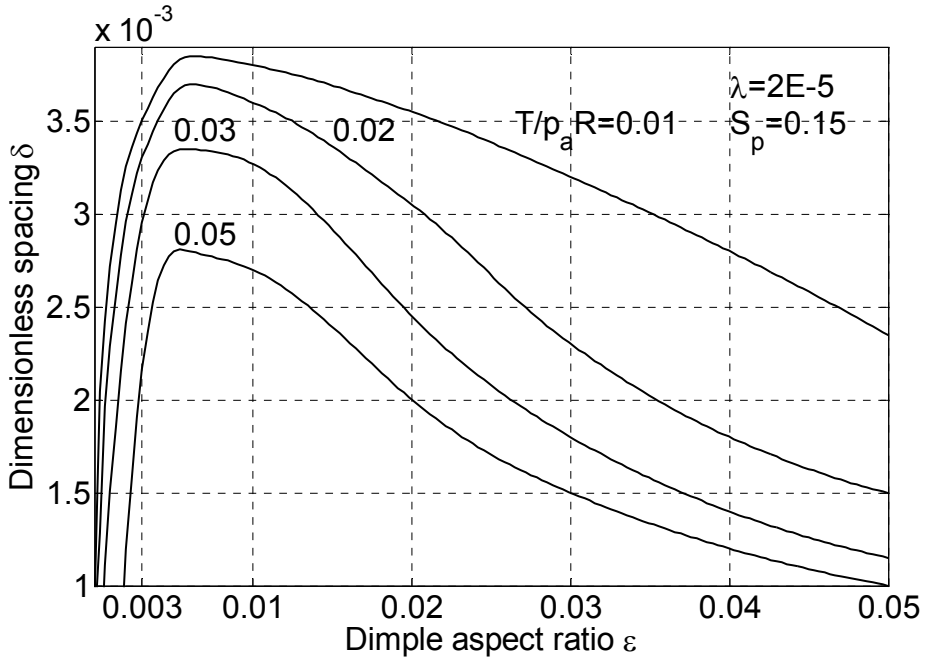

Fig. 6.14: Dimensionless tape/guide spacing δ versus the dimple aspect ratio ε for different values of the dimensionless tape tension

Since we assumed that the tape and guide are conformal, Fig. 6.14 shows the dimensionless tape/guide spacing which is only due to the pressure generated by the presence of dimples in the tape/guide interface. The results presented in Fig. 6.14 were obtained for $\delta > 0.001$ to comply with the assumption of full fluid film lubrication. We observe that the optimum dimple aspect ratio $\varepsilon = 0.006$ maximizes the tape/guide spacing regardless of the tape tension, since this optimum aspect ratio always yields the highest average pressure. For any given ε value, the dimensionless tape/guide spacing decreases when the dimensionless tape tension is increased, as would be expected. We observe that the dimensionless spacing δ is very sensitive to the dimple aspect ratio when $\varepsilon < 0.006$. This is further amplified when the dimensionless tape tension is increased.

The average shear stress in the air bearing, which is a measure of the air friction, can be expressed as

$$\tau = \mu_a U / c_{eq} \tag{6.10}$$

where τ is the shear stress, μ_a is the air viscosity and U is the tape speed. The spacing c_{eq} is an equivalent tape/guide spacing that takes into account the dimple depth [6.19] and can be determined as

$$c_{eq} = c + h_{eq} \tag{6.11}$$

In eq. (6.11), h_{eq} can be obtained by dividing the volume of a dimple by the surface area of its imaginary square cell. Hence,

$$h_{eq} = \frac{h_p S_p}{6 r_p^2}\left(h_p^2 + 3 r_p^2\right) \tag{6.12}$$

Non-dimensionalizing eq. (6.11) with $2r_p$ yields

$$\delta_{eq} = \delta + \frac{2}{3}\varepsilon S_p (\varepsilon^2 + \frac{3}{4}) \tag{6.13}$$

which, for $\varepsilon \le 0.05$, can be approximated by

$$\delta_{eq} = \delta + \varepsilon S_p / 2 \tag{6.14}$$

If $\tau = f(\delta)$ and $\delta = f(\varepsilon)$ are known (see Eqs. (6.10) – (6.14) and Fig. 6.14), one can determine the relationship between the shear stress τ and the dimple aspect ratio ε. Eq. (6.10) can be re-written in terms of δ_{eq} as

$$\tau = \frac{\mu_a U}{2 r_p \delta_{eq}} \tag{6.15}$$

The dimensionless shear stress, or equivalently, the friction coefficient, can be obtained as

$$\frac{\tau}{p_{avg}-p_a}=\frac{\mu_a U}{2r_p\delta_{eq}\left(p_{avg}-p_a\right)} \tag{6.16}$$

Using the non-dimensional flow parameter $\lambda=3\mu_a U/2r_p p_a$ and substituting eq. (6.8) in eq. (6.16), we obtain:

$$\frac{\tau}{p_{avg}-p_a}=\frac{\lambda}{3\delta_{eq}}\frac{p_a R}{T} \tag{6.17}$$

Equation (6.17) represents the friction coefficient $\tau/\left(p_{avg}-p_a\right)$ of the air bearing, generated by presence of the dimples. Fig. 6.15 shows the friction coefficient $\tau/\left(p_{avg}-p_a\right)$ versus the dimple aspect ratio ε for different values of the dimensionless tape tension with a dimple density $S_p=0.15$ and a flow parameter $\lambda=2E-5$.

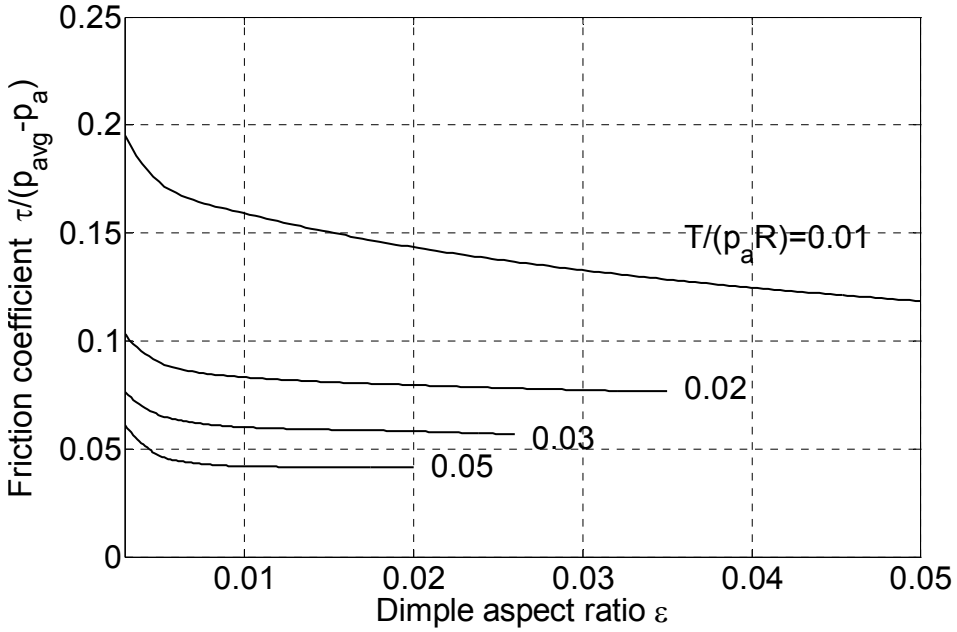

Fig. 6.15: Dimensionless shear stress versus the dimple aspect ratio ε for different dimensionless values of the tape tension

From Fig. 6.15 we observe that for a dimensionless tape tension below 0.02 the dimensionless shear stress decreases monotonically as the dimple aspect ratio increases. For a dimensionless tape tension above 0.02 the dimensionless shear stress initially decreases with increasing dimple aspect ratio but then levels off for aspect ratios above 0.01. This behavior can be understood from the results in Fig. 6.14 and from Eqs. (6.14) and (6.17). As can be seen from Fig. 6.14 for $\varepsilon < 0.006$, a small increase in ε results in a large increase in δ and hence, from Eqs. (6.14) and (6.17), a large increase in δ_{eq} and a large decrease in the friction coefficient, respectively. On the other hand at $\varepsilon > 0.01$ (see Fig. 6.14) an increase in ε may be compensated by a decrease in δ when calculating δ_{eq} thereby leaving the friction coefficient unchanged. This is not the case

for a low tape tension where an increase in ε above 0.01 results in a relatively small decrease in δ (see Fig. 6.14) causing δ_{eq} to increase and the friction coefficient to decrease. As a result, the optimum dimple aspect ratio $\varepsilon = 0.006$ which yields maximum load bearing capacity does not provide a minimum for the friction coefficient.

Finally, we observe from Fig. 6.15 that the friction coefficient decreases for increasing non-dimensional tape tension $T/(p_a R)$, regardless of the dimple aspect ratio ε in accordance with eq. (6.17).

6.7.4 Numerical example

In this section we have compared the predictions of our simplified numerical model with experimental results. We have used the experimental set-up and procedure outlined in [6.18] and [6.16] to measure the friction coefficient between a tape and a guide at tape speeds between 4 and 7 m/s, to make sure the tape operates under full fluid lubrication conditions. Fig. 6.16 shows a comparison between the theoretical predictions and experimental results for a textured guide with a radius *R* of 15 mm, dimple density $S_p = 0.15$ and dimple aspect ratio $\varepsilon = 0.02$. The tape was a commercial MP tape of width $w = 0.0127$ m. The tape tension was 1 N and the atmospheric pressure $p_a = 0.1$ MPa, i.e., $T/(p_a R) = 0.05$.

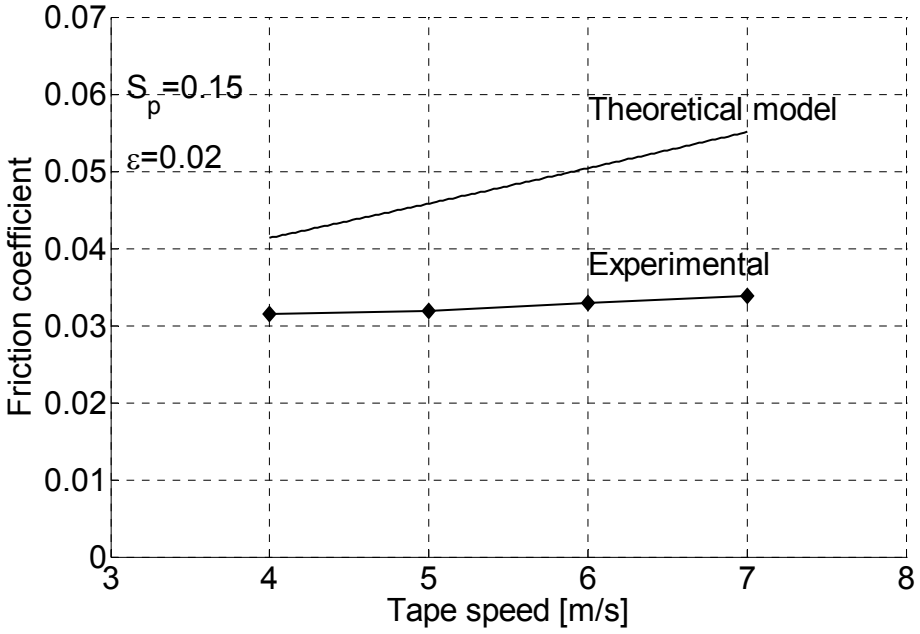

Fig. 6.16: Friction coefficient versus tape speed for an LST guide of radius 15 mm, S_p=0.15 and ε=0.02

The theoretical model is in good agreement with experimental measurements. In the full fluid lubrication regime, the friction coefficient increases slightly for increasing tape speed as predicted qualitatively by the Stribeck curve. The experimental results show that the friction coefficients predicted by the model are of the same order as the experimental results. We note that the values for the theoretical results are higher than those for the experimental results. This is likely due to the simplifying assumption of a conformal and "rigid" tape. A converging channel at the leading edge would create a higher average pressure and thus a higher load bearing capacity. This would result in lower friction coefficients, which would improve the agreement between the theoretical model and experimentally obtained friction coefficients.

6.7.5 Transition speed estimation

In the design of tape drives, it is important to minimize the speed at which the transition from boundary lubrication to hydrodynamic lubrication occurs. For a typical smooth guide with $\sigma_s = 30$ nm, hydrodynamic lubrication occurs for a tape/guide spacing of approximately $c = 100$ nm [6.24]. Fig. 6.17 shows the minimum tape/guide spacing c versus the tape speed for a dimensionless tape tension $T/(p_a R) = 0.1$, for a smooth and a textured guide.

The results in Fig. 6.17 were obtained by superimposing the spacing due to the presence of dimples in the tape/guide interface, calculated with our model, on the spacing calculated for a smooth guide with [6.31]. This approach neglects non-linear effects of the compressible air bearing. However, since compressibility effects are small at low velocity, it can be justified that the total tape guide/spacing for a dimpled guide is, to a first order, the sum of the spacing of a smooth guide and the extra spacing created by the presence of dimples in the tape/guide interface.

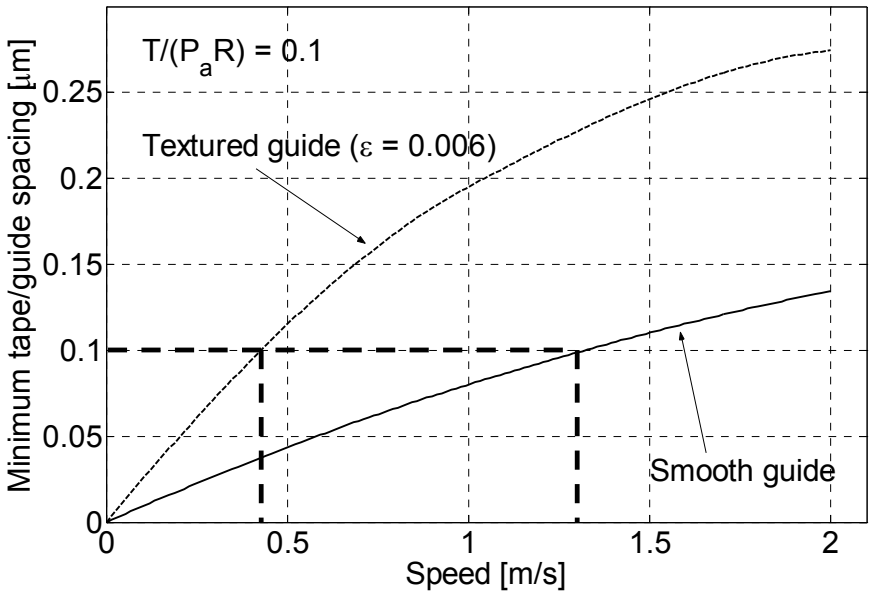

Fig. 6.17: Minimum spacing c versus tape speed for a dimensionless tape tension of $T/(p_a R) = 0.1$

In Fig. 6.17, a horizontal line for $c = 3\sigma_s$ yields the transition speed between boundary and hydrodynamic lubrication for both the smooth and the textured guide. For a $3\sigma_s$-value of 100 nm, we observe from Fig. 6.17 that in the case of a textured guide (dashed line) the transition speed is 0.4 m/s, while in the case of a smooth guide the transition speed is 1.35 m/s. Similarly, for a $3\sigma_s$-value of 130 nm, the transition speed for a textured guide would be 0.55 m/s, and 2 m/s in the case of a smooth guide.

6.7.6 Discussion

Our model predicts that dimpled guides feature a significantly lower transition speed between boundary lubrication and hydrodynamic lubrication than smooth guides. Using dimpled guides (stationary) in commercial tape drives instead of the currently used smooth rollers (rotating), would potentially yield improvements in terms of tape transport and lateral tape motion. Furthermore, tape wear, which is a problem of considerable interest in tape drives with smooth stationary guides, will also be reduced due to the lower transition speed.

Additionally, dimpled guides would potentially enable the wide-spread introduction of metal evaporated (ME) tape. ME tape is desirable from a magnetics point of view, since the cobalt magnetic layer has a higher coercivity than the currently used metal particulate (MP) tape. Hence, ME tape would allow an increase in storage density, compared to MP tape. The tribological performance of ME tape, however, is problematic compared to MP tape, especially at low tape speeds, where surface contact occurs between the tape and the guide surface [6.10, 6.25-6.26]. Dimpled guide surfaces create a higher air bearing pressure compared to smooth guides and, thus, increase the flying height at low speeds. This would improve the tribological performance of ME tape.

Our model neglects elasto-hydrodynamic effects. However, for low tape speeds corresponding to the transition from boundary to hydrodynamic lubrication, the bearing

number is small and thus the compressibility effects of the air bearing are less prominent, i.e., it is justifiable to approximate the compressible air bearing by an incompressible one.

Including elasto-hydrodynamic effects in the model would yield a more accurate solution than our current model but would require a substantially larger numerical effort. For a full-size simulation of the complete tape/dimpled guide interface we calculate the following scenario. Assuming a guide with a radius of 10 mm, a dimple density of 0.2 and a dimple radius of 50 μm, in combination with a 12.7 mm wide tape and a wrap angle of 90 degrees, we calculate that the tape/guide interface contains approximately 20,000 dimples. To fully capture the pressure gradient created over a dimple, a grid of 200 by 200 nodes per dimple (imaginary cell) is needed. Hence, 800 million nodes would be required to simulate the complete tape/guide interface. A numerical problem of this size poses a challenge to present day computer hardware and requires long simulation times, if it is at all solvable.

6.8 Conclusion

- The optimum dimple density was found to be between 0.1 and 0.3, depending on the dimple aspect ratio. A greater dimple aspect ratio will reduce the optimum dimple density. The tape/guide minimum spacing does not affect the optimum dimple density.

- The optimum dimple aspect ratio for maximum average air bearing pressure was found to be 0.006, almost independent of the dimensionless tape/guide spacing δ and the flow factor λ.
- The friction coefficient decreases monotonically with increasing dimple aspect ratio. Our simplified model shows good qualitative agreement with experimental results.
- The transition speed between boundary and hydrodynamic lubrication is reduced for a dimpled guide compared to a smooth guide.
- Improvements to the present model can be obtained by including the elasto-hydrodynamic effects.

6.9 Acknowledgements

Chapter 6, in part, is a reprint of the material as it appears in "Enhancing the Tribological Performance of the Magnetic Tape/Guide Interface by Laser Surface Texturing", Raeymaekers B., Etsion I., Talke F.E., Tribology Letters, 2007. The dissertation author was the primary investigator and author of this paper.

Chapter 6, in part, has been submitted for publication in "A Model for Magnetic Tape/Guide Friction Reduction by Laser Surface Texturing", Raeymaekers B., Etsion I., Talke F.E., Tribology Letters, 2007. The dissertation author was the primary investigator and author of this paper.

6.10 References

[6.1] Peng ZC, Khonsari MM, 2004, Hydrodynamic Analysis of Compliant Foil Bearings with Compressible Air Flow, J. Trib. T. ASME, Vol. 126, pp. 542 - 546

[6.2] Peng ZC, Khonsari MM, 2004, On the Limiting Load-Carrying Capacity of Foil Bearings, J. Trib. T. ASME, Vol. 126, pp. 817 - 818

[6.3] Fields S, 2004, Foil Air Bearing Takes Flight, Tribol. Lubr. Technol., Vol. 60(4), pp. 29 - 33

[6.4] Baugh E, Talke FE, 1996, The Head Tape Interface: A Critical Review and Recent Results, Tribol. T., Vol. 39(2), pp. 306 - 313

[6.5] Richards DB, Sharrock MP, 1998, Key Issues in the Design of Magnetic Tape for Linear Systems of High Track Density, IEEE T. Mag., Vol. 34(4), pp. 1878 - 1882

[6.6] Taylor RJ, Talke FE, 2005, Investigation of Roller Interactions with Flexible Tape Medium, Tribol. Int., Vol. 38, pp. 599 - 605

[6.7] Raeymaekers B, Talke FE, 2007, Lateral Motion of an Axially Moving Tape on a Cylindrical Guide Surface, J. Appl. Mech. T. ASME (in press)

[6.8] Ono K, 1979, Lateral Motion of an Axially Moving String on a Cylindrical Guide Surface, J. Appl. Mech. T. ASME, Vol. 46, pp. 905 - 912

[6.9] Taylor RJ, Strahle P, Stahl J, Talke FE, 2000, Measurement of Cross-Track Motion of Magnetic Tapes, J. Info. Storage Proc. Syst., Vol. 2, pp. 255 - 261

[6.10] Raeymaekers B, Etsion I, Talke FE, 2007, The Influence of Design and Operating Parameters on the Magnetic Tape/Guide Friction Coefficient, Tribol. Lett., Vol. 25(2), pp. 161 - 171

[6.11] Crahay J, Bragard A, 1983, Gravure de la Rugosité des Cylindres de Laminoir par Impulsions Laser, Revue de Métallurgie CIT, pp. 393 - 401

[6.12] Ranjan R, Lambeth DN, Tromel M, Li Y, 1991, Laser Texturing for Low-Flying-Height Media, J. Appl. Phys., Vol. 69(8), pp. 5745 - 5747

[6.13] Etsion I, Burstein L, 1996, A Model for Mechanical Seals with Regular Microsurface Structure, Tribol. T., Vol. 39(3), pp. 667 - 683

[6.14] Scott DA, Brandt M, Dorien-Brown B, Valentine B, De P, 1993, Laser Modification of Metal Surfaces, Opt. Laser Eng., Vol. 18, pp. 1 - 13

[6.15] Etsion I, 2004, Improving Tribological Performance of Mechanical Components by Laser Surface Texturing, Tribol. Lett., Vol. 17(4), pp. 733 - 737

[6.16] Etsion I, 2005, State of the Art in Laser Surface Texturing, J. Trib. T. ASME, Vol. 127, pp. 248 - 253

[6.17] Duffet G, Sallamand P, Vannes AB, 2003, Improvement in Friction by cw Nd:YAG Laser Surface Treatment on Cast Iron Cylindrical Bore, Appl. Surf. Sci., Vol. 205, pp. 289 - 296

[6.18] Erdemir A, 2005, Review of Engineered Tribological Interfaces for Improved Boundary Lubrication, Tribol. Int., Vol. 38, pp. 249 - 256

[6.19] Kligerman Y, Etsion I, 2001, Analysis of the Hydrodynamic Effects in a Surface Textured Circumferential Gas Seal, Tribol. T., Vol. 44(3), pp. 472 - 478

[6.20] Tan AH, Cheng SW, 2006, A Novel Textured Design for Hard Disk Drive Tribology Improvement, Tribol. Int., Vol. 39, pp. 506 - 511

[6.21] Shigley JE, Mischke CR, 1989, Mechanical Engineering Design, 5th edition, McGraw Hill, New York

[6.22] Greenwood JA, Williamson JBP, 1966, Contact of Nominally Flat Surfaces, Proceedings of the Royal Society of London Series A – Mathematical and Physical Sciences, Vol. 295 (1442), pp. 300 - 319

[6.23] McCool JI, 1987, Relating Profile Instrument Measurements to the Functional Performance of Rough Surfaces, J. Trib. T. ASME, Vol. 109, pp. 264 – 270

[6.24] Patir N, Cheng HS, 1978, Average Flow Model for Determining Effects of 3-Dimensional Roughness on Partial Hydrodynamic Lubrication, J. Lubr. Technol. T. ASME, Vol. 100(1), pp. 12-17

[6.25] Hempstock MS, Sullivan JL, 1996, The Durability and Signal Performance of Metal Evaporated and Metal Particle Tape, IEEE T. Mag., Vol. 32(5), pp. 3723 - 3725

[6.26] Hempstock MS, Sullivan JL, 1996, A Study of the Mechanical and Magnetic Performance of Metal Evaporated Tape, J. Mag. Mag. Mat., Vol. 155, pp. 323 - 328

[6.27] Patton ST, Bhushan B, 1999, Origins of Friction and Wear of the Thin Metallic Layer of Metal Evaporated Magnetic Tape, Wear, Vol. 224, pp. 126 - 140

[6.28] Bijker MD, Draaisma EA, Eisenberg M, Jansen J, Persat N, Sourty E, 2000, Future Directions in Advanced Digital Recording Technology, Tribol. Int., Vol. 33, pp. 383 - 390

[6.29] Osaki H, 2003, Recent Research of Tape/Drive Tribology, Tribol. Int., Vol. 36, pp. 349 - 360

[6.30] Hashimoto H, Okajima M, 2006, Theoretical and Experimental Investigations Into Spacing Characteristics Between Roller and Three Types of Webs With Different Permeabilities, J. Trib. T. ASME, Vol. 128, pp. 267 - 274

[6.31] Lacey C, Talke FE, 1990, A Tightly Coupled Numerical Foil Bearing Solution, IEEE T. Mag., Vol. 26(6), pp. 3039 - 3043

[6.33] Hirsch C, 1988, Numerical Computation of Internal and External Flows, Vol.1, J. Wiley and Sons, New York

[6.34] Eshel A, Elrod HG, 1965, The Theory of the Infinitely Wide, Perfectly Flexible, Self-Acting Foil Bearing, J. Basic Eng. T. ASME, Vol. 87, pp. 831 - 836

7. Design of a dual stage actuator tape head with high bandwidth track-following capability

7.1 Introduction

In a typical tape head as shown in Fig. 7.1, the read/write heads are an integral part of the air bearing surface. The entire head is mounted on a bracket, which is connected to the movable coil of the voice coil motor (VCM). The read/write heads can be displaced laterally by the VCM. Alignment and stiffness is provided by a leaf spring on top of the head. Fig. 7.1 a) shows a typical tape head, while Fig. 7.1 b) shows the voice coil motor, which is mounted in the housing at the bottom of the tape head.

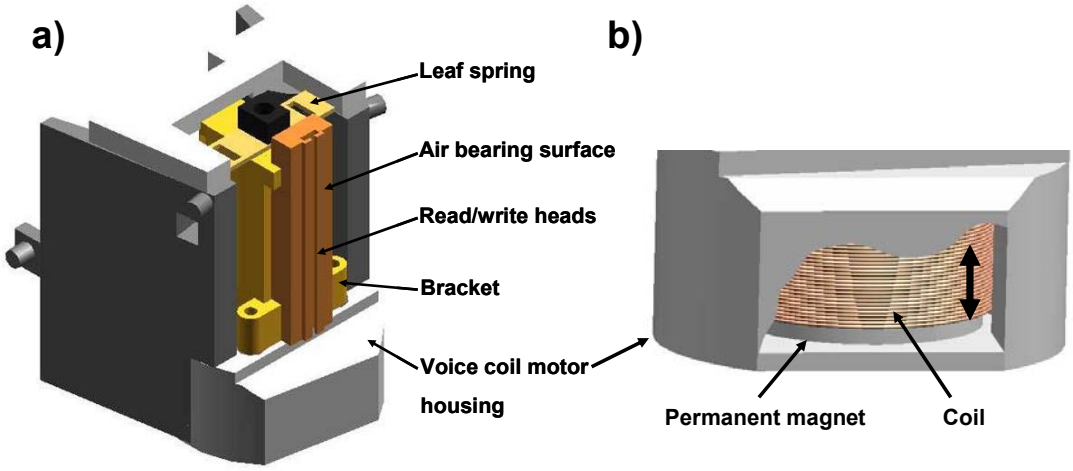

Fig. 7.1: a) Typical tape head and b) schematic of a voice coil motor (VCM)

The VCM consists of a stationary permanent magnet, which is fixed to the VCM housing, and a coil that can move co-axially with the permanent magnet. The coil is

connected to the bracket. The lateral position of the coil in the VCM (and thus the read/write heads) is determined by the electromagnetic force F_{em} acting on the coil, given by

$$F_{em} = \left(B \times I_c \right) l_c \tag{7.1}$$

where B is the magnetic inductance of the permanent magnet, I_c is the electric current flowing through the coil and l_c is the length of the coil. Hence, the magnitude of the current I_c determines the lateral position of the coil in the VCM.

The lateral position of the head is controlled by a servo loop. During lateral tape displacement, an error signal from the servo head is generated and the head is moved by the VCM to avoid track misregistration. However, the bandwidth of the VCM is limited, mainly due to mass and available power. LTM frequencies higher than the bandwidth of the servo actuator, generally referred to as high frequency LTM, cannot be followed by the servo actuator. State-of-the-art tape head actuators have a bandwidth on the order of 750 – 1000 Hz.

7.2 Concept of the dual stage actuator head

The concept of a dual stage actuator was first introduced in hard disk drive (HDD) technology about 15 years ago. Mori et al. introduced a piezo (PZT) based rotary micro-actuator at the suspension level [7.1]. The VCM is used as a “coarse actuator”, while the PZT is used as a “fine actuator”. Different types of micro-actuator designs have been

proposed in the literature. Koganezawa et al. devised a micro-actuator that operates at the suspension level of a HDD but uses a flexural cross-shaped spring [7.2]. Instead of using a "stacked"-PZT, they used shear-mode PZT crystals [7.3]. Evans and Griesbach presented a piezoelectric micro-actuator design that takes into account manufacturability and economical considerations [7.4]. They modeled the dynamics of their design and presented two voltage drivers that can be used to drive the actuator. Nakamura et al. introduced a push-pull multi-layered piggyback PZT actuator that operates at the suspension level [7.5]. Their design features a high stroke, combined with a low voltage.

While most designs are PZT-based, some researchers also attempted to manufacture electrostatic micro-actuators. Fan et al. implemented a micro-actuator that operates at the slider level instead of the suspension level [7.6]. A more in-depth analysis of the design proposed by Fan et al. was presented in [7.7] by Hirano et. al. Horsley et al. used parallel-plate capacitive electrodes to generate an electrostatic force, which was used to drive an actuator [7.8]. Finally, the design of an electromagnetic micro-actuator was investigated by Tang et al. [7.9].

This chapter presents the design of a dual stage actuator tape head. We attempt to increase the bandwidth of the servo loop by introducing a piezo crystal (PZT) micro-actuator. This micro-actuator serves as a fine-tuning mechanism that can follow high frequency LTM (> 1 kHz) but is limited in its stroke. Increased servo bandwidth would allow an increase in track density, since track misregistration will be reduced. The main

goal of this dual stage actuator tape head design is to follow the low frequency LTM (< 1 kHz) with the VCM, and to follow the high frequency LTM (> 1 kHz) with the micro-actuator.

7.3 Piezo-electricity

7.3.1 Principle

Piezo-electric (PZT) transducers have the characteristic to expand/contract when a potential difference is applied over both ends of the transducer. A PZT transducer thus converts electrical energy into mechanical energy (and vice versa). Fig. 7.2 illustrates the piezo-electric effect. Fig. 7.2 a) shows how a PZT crystal expands when a voltage v is applied over its poles, while Fig. 7.2 b) shows how a PZT crystal contracts when it is subjected to a voltage $-v$ (opposite polarity) [7.10].

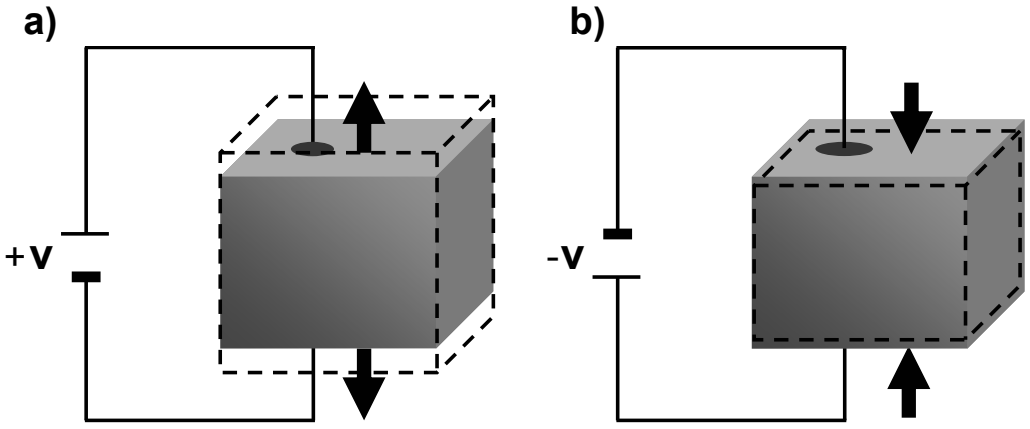

Fig. 7.2: Principle of piezo-electricity a) expansion and b) contraction as a result of an applied voltage (potential difference)

Among materials that exhibit the piezo-electric effect are quartz and ceramics with perovskite or tungsten-bronze structures ($BaTiO_3$, $SrTiO_3$, $Pb\left(ZrTi\right)O_3$,...) [7.11, 7.12].

7.3.2 Constitutive equation

The constitutive equation that relates the strain ε of the PZT transducer to the applied electric field E is given by [7.13]

$$\varepsilon_i = S_{ij}^E \sigma_j + d_{ki} E_k \tag{7.2}$$

$i, j = 1\ldots6$ and $k = 1\ldots3$. ε is the strain tensor, S^E is the compliance matrix at constant electric field strength [m²/N], σ is the stress tensor [N/m²], d is the matrix with piezoelectric constants of the PZT transducer [C/N] and E is the strength of the electric field [N/C].

Assuming that the material is poled along axis 3, and taking into consideration that piezoelectric material is transverse isotropic, i.e., it exhibits the same properties in the plane but different properties in the direction normal to this plane, eq. (7.2) can be written as

$$\begin{bmatrix} \varepsilon_1 \\ \varepsilon_2 \\ \varepsilon_3 \\ \varepsilon_4 \\ \varepsilon_5 \\ \varepsilon_6 \end{bmatrix} = \begin{bmatrix} S_{11}^E & S_{12}^E & S_{13}^E & 0 & 0 & 0 \\ S_{12}^E & S_{11}^E & S_{13}^E & 0 & 0 & 0 \\ S_{13}^E & S_{13}^E & S_{33}^E & 0 & 0 & 0 \\ 0 & 0 & 0 & S_{44}^E & 0 & 0 \\ 0 & 0 & 0 & 0 & S_{44}^E & 0 \\ 0 & 0 & 0 & 0 & 0 & 2\left(S_{11}^E - S_{12}^E\right) \end{bmatrix} \begin{bmatrix} \sigma_1 \\ \sigma_2 \\ \sigma_3 \\ \sigma_4 \\ \sigma_5 \\ \sigma_6 \end{bmatrix} + \begin{bmatrix} 0 & 0 & d_{31} \\ 0 & 0 & d_{31} \\ 0 & 0 & d_{33} \\ 0 & d_{15} & 0 \\ d_{15} & 0 & 0 \\ 0 & 0 & 0 \end{bmatrix} \begin{bmatrix} E_1 \\ E_2 \\ E_3 \end{bmatrix} \tag{7.3}$$

The stress and strain can be represented as column vectors with six elements, because the stress and strain tensors are symmetric tensors of rank two [7.13]. Thus, the indices of the tensor can be replaced as follows: 11→1, 22→2 , 33→3 , 12→4, 23→5, 13→6. The compliance matrix can be presented as a 6-by-6 matrix.

Fig. 7.3 shows an example of a PZT crystal poled along axis 3. An electric field E_3 is created due to a voltage v, applied over the poles of the crystal. $E_1 = E_2 = 0$ and no mechanical stress is applied on the crystal ($\sigma = 0$). From eq. (7.3), it can be seen that the crystal expands along axis 3, resulting in a strain $\varepsilon_3 = d_{33}E_3$. Simultaneously, the crystal contracts along axis 1 and axis 2, resulting in a strain $\varepsilon_1 = \varepsilon_2 = d_{13}E_3$, where d_{13} is negative. In the design of the micro-actuator for the dual stage tape head, poling along axis 3 will be used.

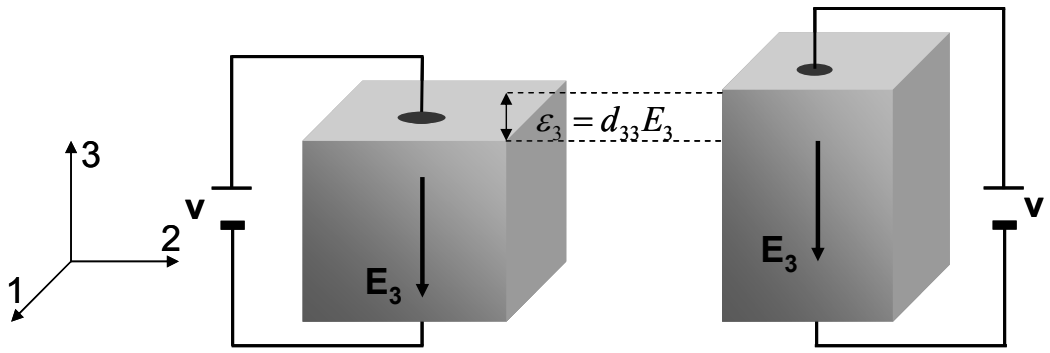

Fig. 7.3: Application of piezoelectricity

7.4 Design of dual stage actuator tape head

Fig. 7.4 illustrates the mechanical design of the dual stage actuator tape head. Fig. 7.4 a) shows an isometric view, while Fig. 7.4 b) shows a side view. Fig. 7.4 c) and d) show pictures of the actual mechanical prototype of the dual stage actuator head.

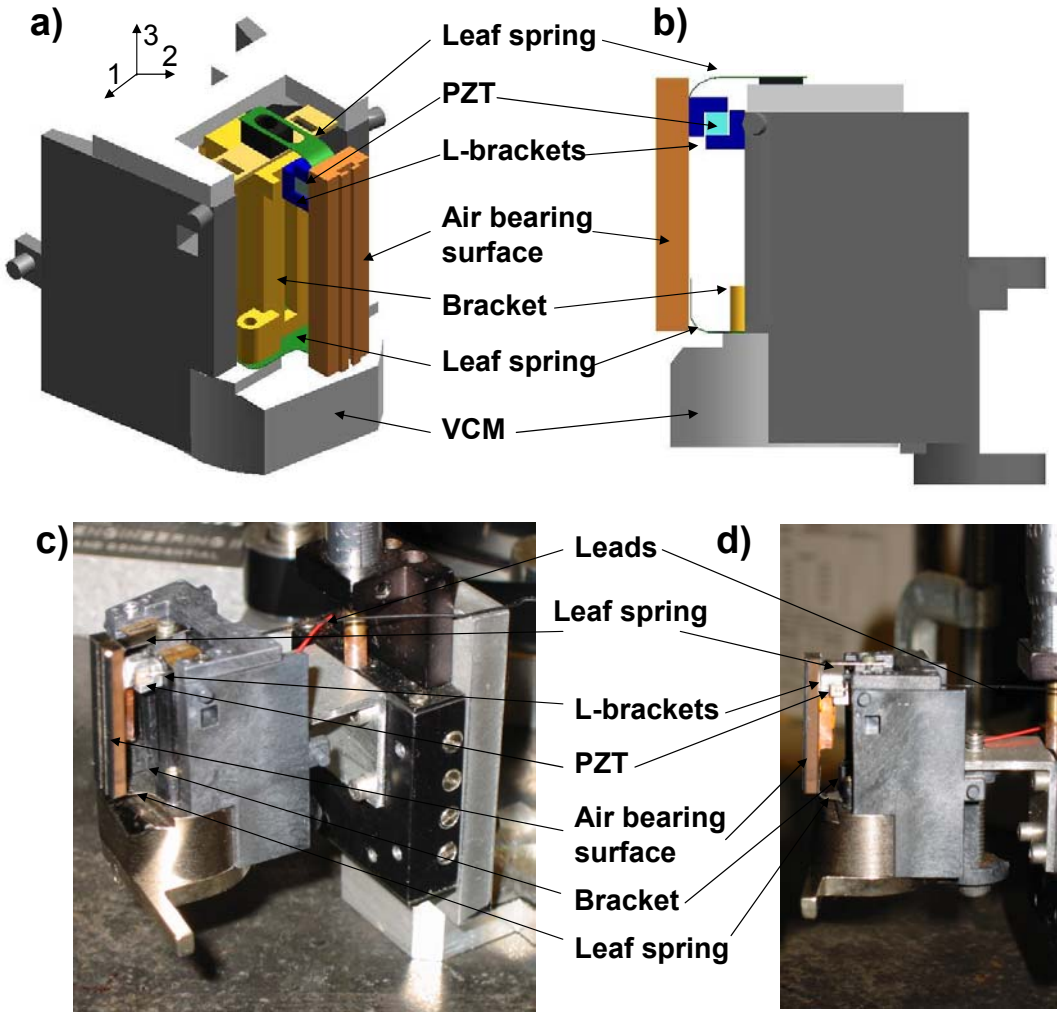

Fig. 7.4: Mechanical design of dual-stage actuator tape head a) isometric view, b) side view, c) isometric view of prototype and d) side view of prototype

The design is based on a commercial tape head, shown in Fig. 7.1 a). Two L-brackets, which encapsulate a PZT transducer, form the micro-actuator which drives the second stage of the dual stage actuator tape head. The L-brackets are attached to the tape head bracket and the air bearing surface, respectively. Two leaf springs at the top and bottom of the air bearing surface provide alignment and stiffness. The leaf springs are flexible with respect to bending around axis 1 (see Fig. 7.4 a)), but inhibit bending around axis 2 and axis 3. Therefore, warping and torsion of the air bearing surface is minimized. The PZT is a 2 x 2 x 2 mm stacked crystal (type PL022 from Physik Instrumente (PI)).

7.5 Dynamics

7.5.1 Static response

Fig. 7.5 a) shows the displacement versus voltage of the PZT micro-actuator, while Fig. 7.5 b) shows displacement versus voltage of the VCM. We observe that the PZT micro-actuator exhibits a linear response with a small hysteresis. Hysteresis is caused by crystalline polarization effects and molecular effects within the piezoelectric material [7.13]. The use of a closed-loop control system allows accounting for the hysteresis during dynamic operation [7.13]. From Fig. 7.5 b) we observe that the VCM has a linear range between 0 and 2 Volts. Higher voltages lead to saturation of the VCM. As can be seen from Fig. 7.5 b), the displacement-voltage curve levels off for voltages

above 2 Volts. Analog to the case of the PZT micro-actuator, a small amount of hysteresis is also observed for the VCM.

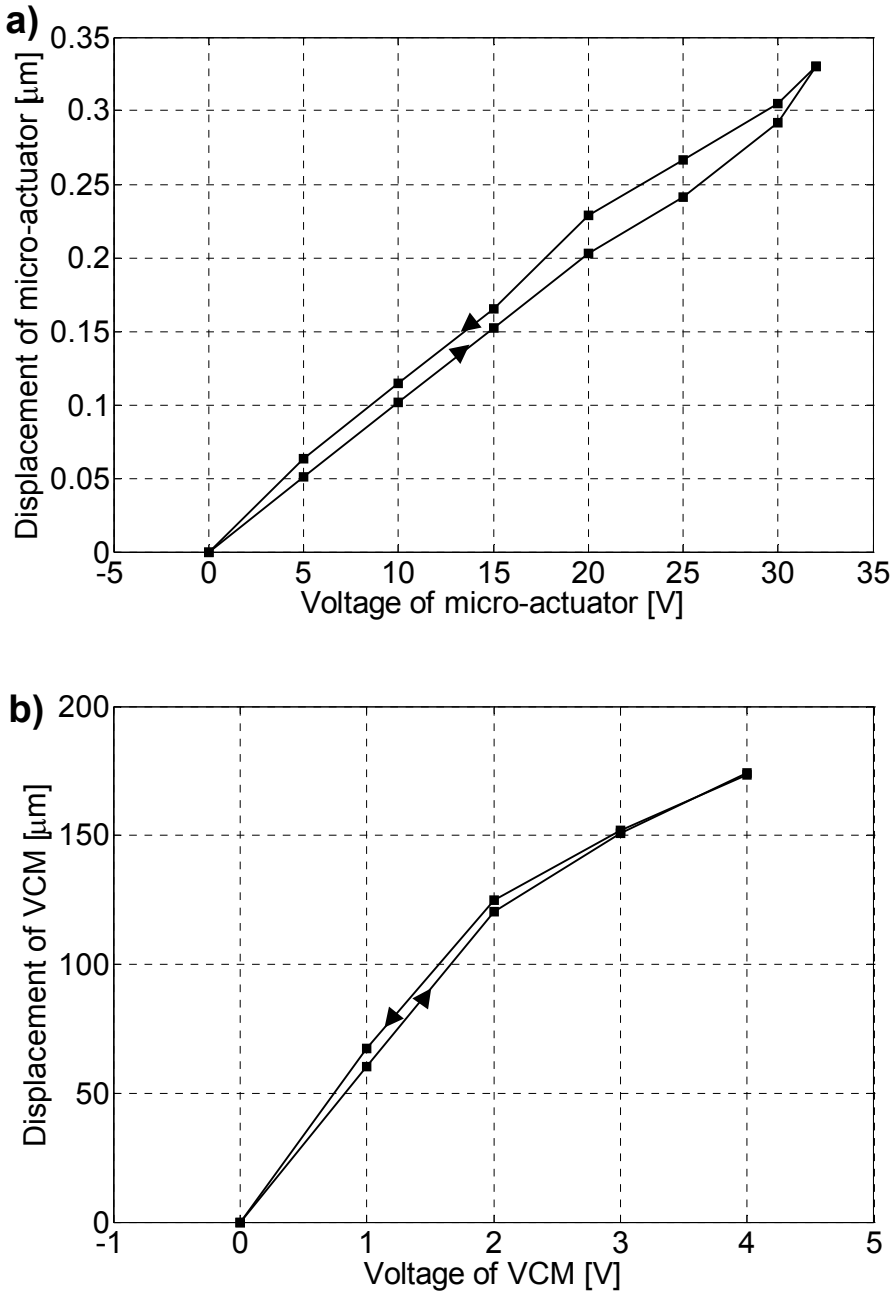

Fig. 7.5: Static response of a) PZT micro-actuator and b) voice coil motor

7.5.2 Dynamic response

The dual stage actuator head design can be represented by the mechanical model shown in Fig. 7.6. The mass m_1 represents the VCM with stiffness k_1 and damping c_1. The mass m_2 represents the PZT micro-actuator with stiffness k_2 and damping c_2. Mass m_1 is connected to a fixed base, indicating that the VCM is firmly connected to the rest of the tape drive. The displacement of the PZT micro-actuator and the VCM are denoted by y_2 and y_1, respectively. The force during actuation of the VCM is denoted by u_1, while u_2 represents the force during actuation of the PZT.

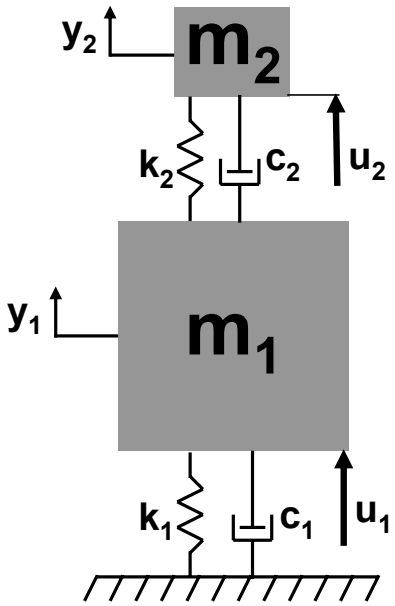

Fig. 7.6: Simplified mechanical model of the dual-stage actuator head

The equations of motion for the dynamic system shown in Fig. 7.6, when actuated with a force u_2, can be written as

$$\begin{cases} m_1\ddot{y}_1 = -k_1 y_1 - c_1\dot{y}_1 + k_2\left(y_2 - y_1\right) + c_2\left(\dot{y}_2 - \dot{y}_1\right) - u_2 \\ m_2\ddot{y}_2 = u_2 - k_2\left(y_2 - y_1\right) - c_2\left(\dot{y}_2 - \dot{y}_1\right) \end{cases} \tag{7.4}$$

After Laplace transform, the effect of the force u_2 on the displacement of the PZT micro-actuator (y_2) can be written as

$$\frac{Y_2}{U_2} = \frac{\left(m_1 s^2 + c_1 s + k_1\right)}{\left(m_1 m_2\right)s^4 + \left[m_2\left(c_1 + c_2\right) + m_1 c_2\right]s^3 + \left[2\left(k_1 + k_2\right)m_2 + c_1\right]s^2 + \left(c_1 k_2 + c_2 k_1\right)s + k_1 k_2} \tag{7.5}$$

where U_2 and Y_2 are the Laplace transforms of u_2 and y_2, given by $U_2(s) = \int_0^\infty e^{-st} u_2(t)dt$ and $Y_2(s) = \int_0^\infty e^{-st} y_2(t)dt$.

Fig. 7.7 shows the FRF for the simplified second order mass-spring-damper model of Fig. 7.6. To obtain a first order approximation of the dynamics of the PZT micro-actuator, the following parameters were used: $m_1 = 0.1$ kg (measured), $m_2 = 0.005$ kg (measured), $c_1 = c_2 = 1$ Ns/m, $k_1 = 1000$ N/m (measured), $k_2 = 30\times10^6$ N/m (data sheet PZT).

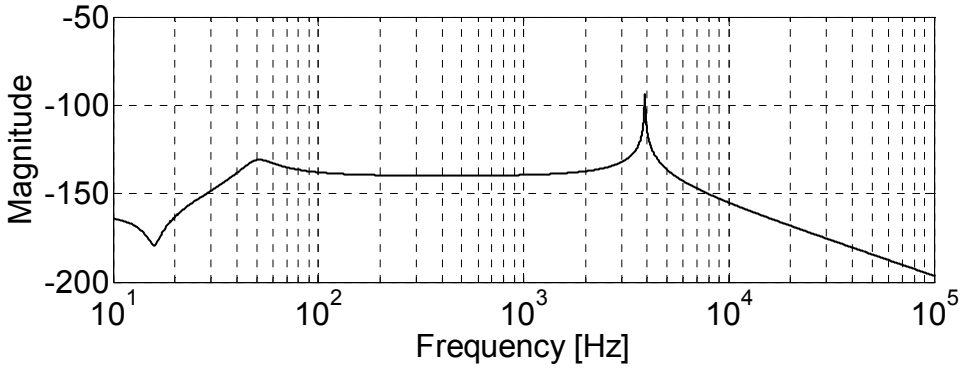

Fig. 7.7: FRF of the simplified mechanical model of the dual-stage actuator head

The model and its frequency response, shown in Fig. 7.6 and Fig. 7.7, do not represent the dual stage actuator of Fig.7.4 accurately, and a better model is desirable. The dual stage actuator head is a higher order system than the simplified second order mass-spring-damper system shown in Fig. 7.6. Furthermore, stiffness of the brackets, joints and adhesives introduce a high degree of complexity into the system. To design a dual stage actuator servo controller that can operate with the dual stage actuator tape head, the dynamics of the latter must be obtained more accurately.

To determine the dynamic behavior of the VCM and the PZT micro-actuator, the experimental set-up shown in Fig. 7.8 was used. A test signal with varying frequency content (see 7.8 Appendix) was injected into the VCM and the PZT micro-actuator, and the resulting displacements y_1 and y_2 (see Fig. 7.6) were determined with a laser Doppler vibrometer (LDV).

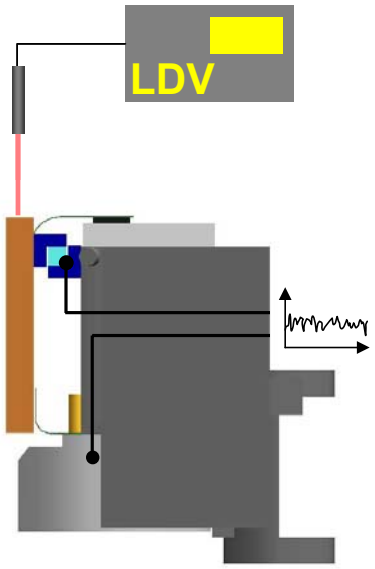

Fig. 7.8: Experimental set-up to determine the frequency response function

The ratio of output and input signal, i.e., the ratio of the measured displacement y_1 or y_2 and the input test signal, yields the frequency response function (FRF). The FRF is a transfer function, which expresses the response of a dynamic system to a given input signal, as a function of frequency. The coherence function was determined for each FRF and found to be equal to one over most of the frequency spectrum investigated. The coherence function is a measure of the quality of the FRF as a function of the frequency. A value of one indicates that the measured output results entirely from the input signal, while a coherence value of zero indicates that the measured output signal is completely unrelated to the input signal.

Fig. 7.9 shows the FRF for the case that the VCM is excited and the response of the VCM is measured (input = u_1, output = y_1). Thus, Fig. 7.9 visualizes the dynamics of the VCM.

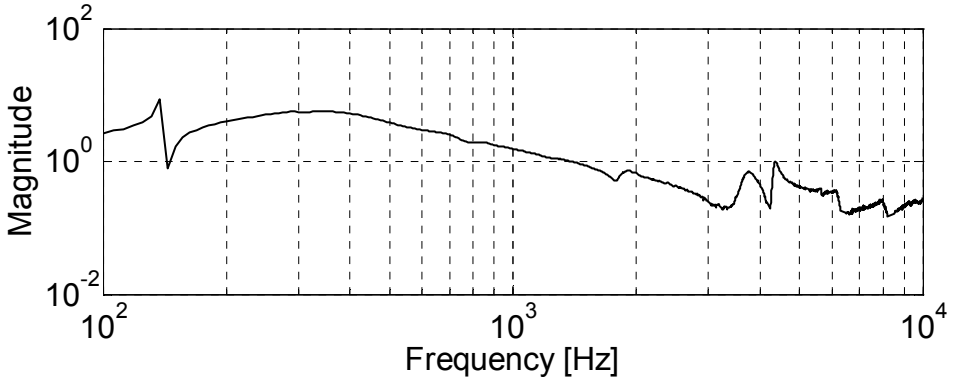

Fig. 7.9: Frequency response function, input = u_1, output = y_1

In Fig. 7.9 we observe that a resonance peak exists at 130 Hz followed by an anti-resonance peak. The resonance peak corresponds to the resonance frequency of the VCM. Furthermore, a fairly flat frequency response up to 3 kHz is observed.

Fig. 7.10 shows the FRF for the case where the VCM is excited and the response of the PZT micro-actuator is measured (input = u_1, output = y_2). Hence, the effect of the VCM on the dynamics of the PZT micro-actuator is visualized.

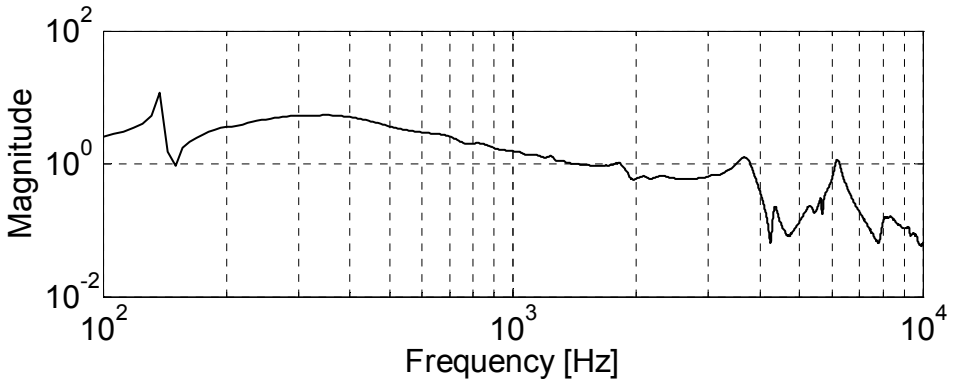

Fig. 7.10: Frequency response function, input = u_1, output = y_2

In Fig. 7.10 we again observe that a well-defined resonance frequency of the VCM exists around 130 Hz. At 1.9 kHz another resonance peak, followed by an anti-resonance peak, is observed. We postulate that this peak corresponds to the frequency where VCM and PZT micro-actuator are counter-acting each other. The resonance peaks at 3.6 and 5.1 kHz are likely eigenfrequencies related to the PZT micro-actuator.

Fig. 7.11 shows the FRF for the case where the PZT micro-actuator is excited and the response of the VCM is measured (input = u_2, output = y_1).

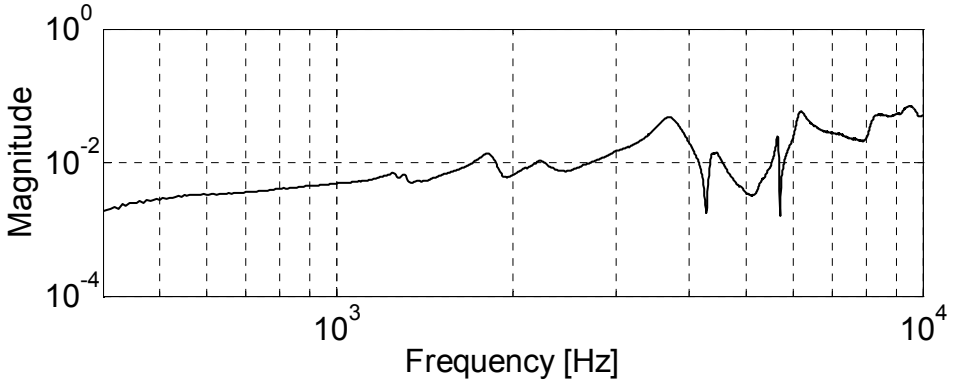

Fig. 7.11: Frequency response function, input = u_2, output = y_1

The effect of the PZT micro-actuator on the dynamics of the VCM is limited, since its mass is much smaller than the mass of the VCM. Therefore, the VCM acts as a solid base and the resonance frequencies observed in Fig. 7.11 are likely related to the PZT micro-actuator.

Fig. 7.12 shows the FRF for the case where the PZT micro-actuator is excited and the response of the PZT micro-actuator is measured (input = u_2, output = y_2). Hence, the dynamics of the PZT micro-actuator are revealed.

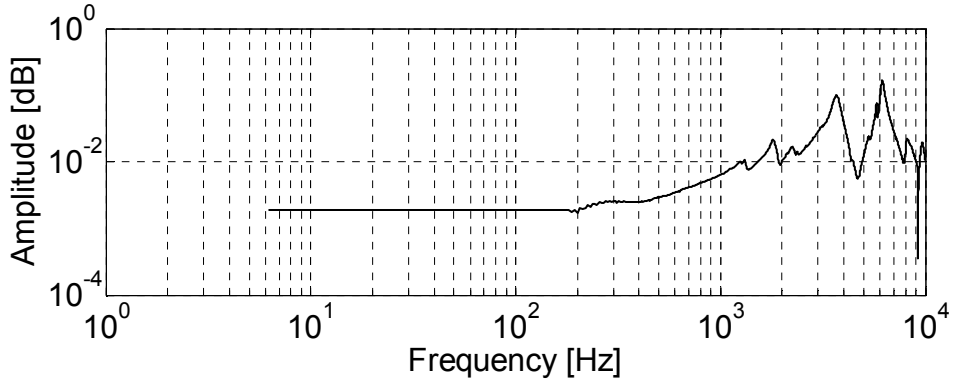

Fig. 7.12: Frequency response function; input = u_2, output = y_2

The resonance peaks of the PZT micro-actuator are again observed in Fig. 7.12. The peaks at 3.6 kHz and 5.1 kHz coincide with the peaks that were observed earlier in Fig. 7.10.

7.6 Modeling of the frequency response function

We have modeled the FRF using system identification techniques. We have fitted a 16th-order ARX model (Auto-Regressive with eXogenous input) [7.15] to the experimentally obtained FRF, shown in Fig. 7.12. The results are displayed in Fig. 7.13 The experimental FRF is shown as a solid line, while the fitted model is shown as a dashed line. Details of the modeling theory and procedure can be found in [7.15, 7.16].

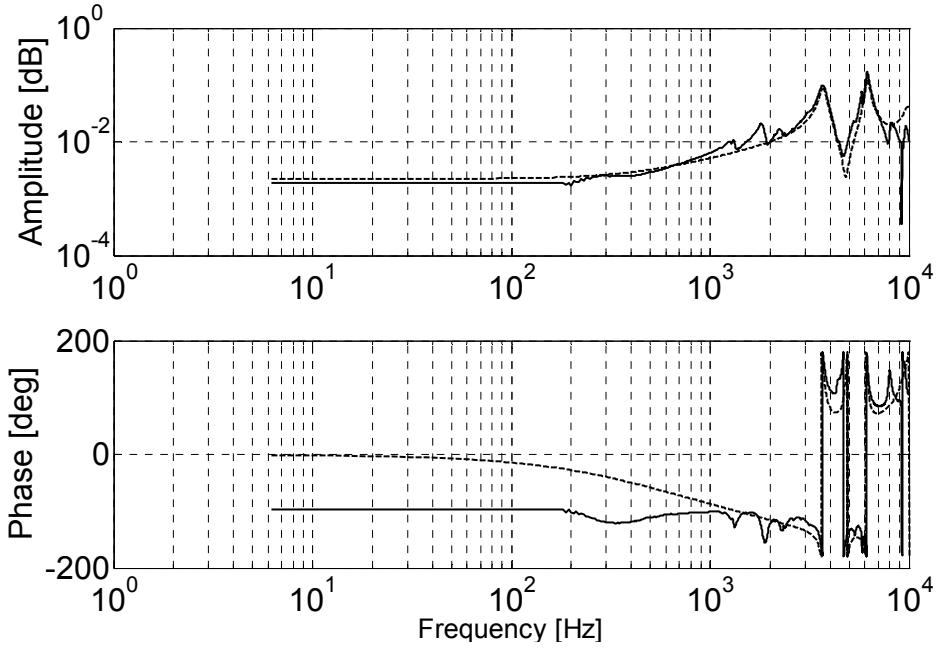

Fig. 7.13: Frequency response function, experimental (solid line), model (dashed line)

To evaluate the quality of our model, we have injected a position error signal (PES) from a commercially available tape drive (LTO generation 2 [7.17]) into the PZT micro-actuator, and measured the response of the air bearing surface with the LDV. For this test we have used the same set-up as shown in Fig. 7.8. Since the PZT micro-actuator will serve as a fine tuning mechanism to track-follow LTM > 1 kHz, we have first high pass filtered the PES > 1 kHz, before injecting it into the actuator. Next, we have injected the same high pass filtered PES into our model and simulated the response of the system. Fig. 7.14 shows both the experimentally obtained (solid line) and simulated response (dashed line) of the PZT micro-actuator as a function of time.

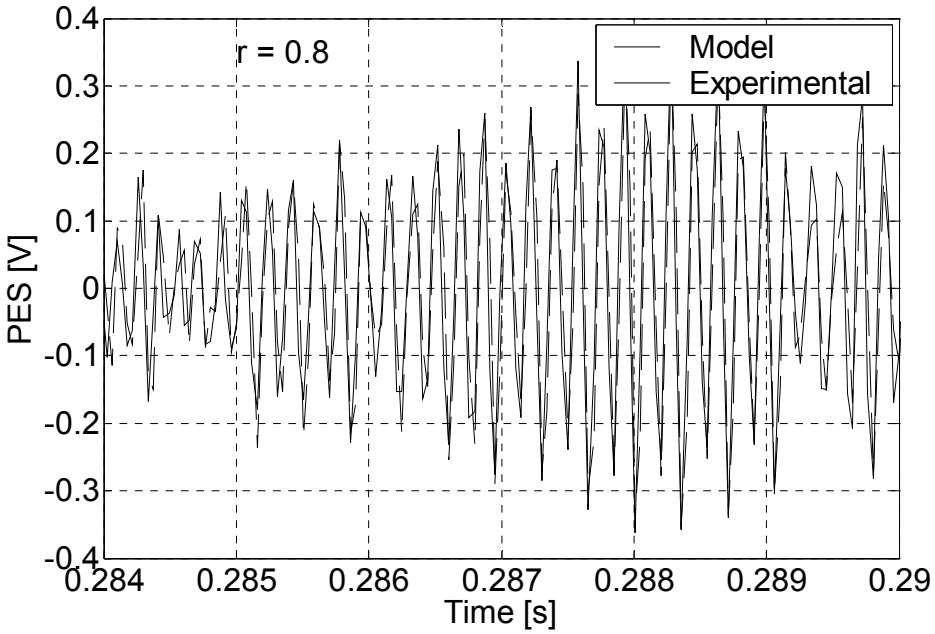

Fig. 7.14: PZT micro-actuator response, experimental (solid line), model (dashed line)

Comparing the experimentally obtained response with the simulated response, we observe very good agreement. We have calculated a cross-correlation coefficient between both responses of 80 %.

7.7 Conclusion

We have implemented the mechanical design of a dual stage actuator tape head for high-bandwidth track-following. The new dual stage actuator tape head promises a significant increase in track density for future high-performance tape drives. We have developed a model based on system identification techniques. Good agreement between the model and the experimental results for the dynamic performance of the new actuator was observed.

The design presented in this chapter is purely a mechanical design. The next step would be to include servo- and read/write capability. This requires the cables to be re-routed around the PZT. The final step would be to redesign the injection molded parts of the tape head, in order to accommodate the PZT, and to enable integration in a commercial tape drive.

7.8 Appendix

A test signal with varying frequency content is generally referred to as a chirp signal. In a linear chirp signal, the instantaneous frequency $f_c(t)$ varies linearly with time, i.e., $f_c(t) = f_{c,0} + k_c t$. $f_{c,0}$ is the starting frequency at $t = 0$ and k_c is the rate of frequency increase [7.14]. A chirp function is particularly interesting to determine a frequency response function of a system since the signal can contain all desired

frequencies with the same amplitude. A sinusoidal chirp function with amplitude one is given as

$$y_c(t) = \sin\left(2\pi\left(f_{c,0} + \frac{k_c}{2}t\right)t\right) \tag{7.A1}$$

Fig. 7.A1 shows a sinusoidal chirp function with amplitude one, a starting frequency $f_{c,0}$ = 0.1 Hz and "chirp factor" k_c =100.

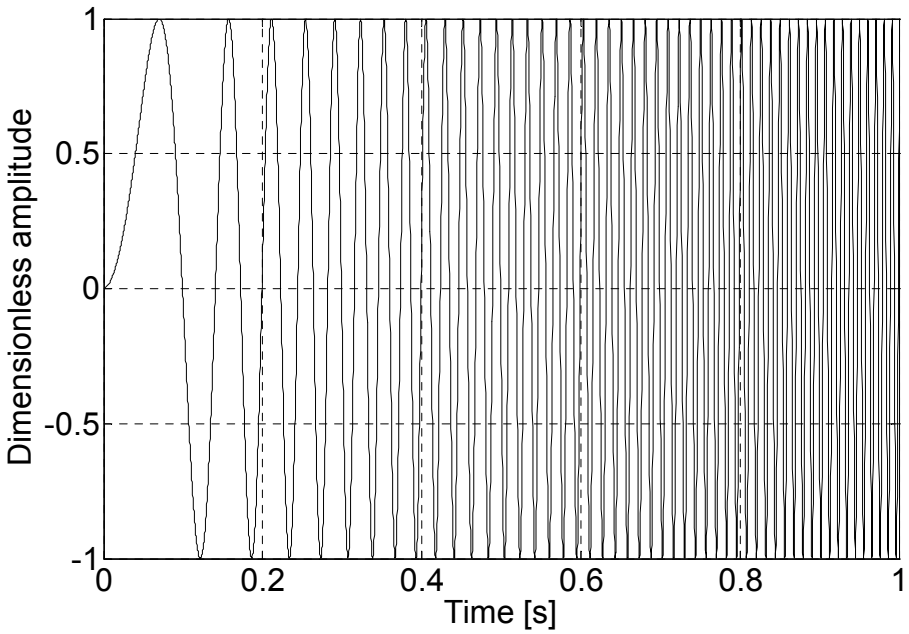

Fig. 7.A1: Chirp function

7.9 References

[7.1] Mori K, Munemoto T, Otsuki H, Yamaguch Y, Akagi K, 1991, A Dual Stage Magnetic Disk Drive Actuator Using A Piezoelectric Device for a High Track Density, IEEE T. Mag., Vol. 27(6), pp. 5298 – 5300

[7.2] Koganezawa S, Takaishi Y, Mizoshita Y, Uematsu Y, Yamada T, Hasegawa S, Ueno T, 1996, A Flexural Piggyback Mill-Actuator for Over 5 Gbit/in.² Density Magnetic Recording, IEEE T. Mag., Vol. 32(5), pp. 3908 – 3910

[7.3] Hirano T, Fan LS, Lee WY, Hong J, Imaino W, Pattanaik S, Chan S, Webb P, HorowitzR, Aggarwal S, Horsley D, 1998, High-Bandwidth High-Accuracy Rotary Microactuators for Magnetic Hard Disk Drive Tracking Servos, IEEE/ASME T. Mech., Vol. 3(3), pp. 156 – 165

[7.4] Koganezawa S, Uematsu Y, Yamada T, 1999, Dual Stage Actuator System for Magnetic Disk Drives Using a Shear Mode Piezoelectric Microactuator, IEEE T. Mag., Vol. 35(2), pp. 988 – 992

[7.5] Nakamura S, Numasato H, Kobayashi M, Naniwa I, 2002, A Push-Pull Multi-Layered Piggyback PZT Actuator, Microsyst. Technol., Vol. 8, pp. 149 – 154

[7.6] Fan LS, Ottesen HH, Reiley TC, Wood RW, 1995, Magnetic Recording Head Positioning at Very High Track Densities Using a Microactuator-Based, Two-Stage Servo System, IEEE T. Ind. Electr., Vol. 42(3), pp. 222 – 233

[7.7] Evans RB, Griesbach JS, 1999, Piezoelectric Microactuator for Dual Stage Control, IEEE T. Mag., Vol. 35(2), pp. 977 – 982

[7.8] Horsley DA, Wongkomet N, Horowitz R, Pisano AP, 1999, Precision Positioning Using a Microfabricated Electrostatic Actuator, IEEE T. Mag., Vol. 35(2), pp. 993 – 999

[7.9] Tang W, Temesvary V, Miller R, Desai A, Tai YC, Miu D, 1995, Silicon Micromachined Electromagnetic Microactuators for Rigid Disk Drives, IEEE T. Mag., Vol. 31(6), pp. 2964 – 2966

[7.10] Sashida T, Kenjo T, 1993, An Introduction to Ultrasonic Motors, Calarendon Press, Oxford

[7.11] Uchino K, 1997, Piezoelectric Actuators and Ultrasonic Motors, Kluwer Academic Publishers, Boston/Dordrecht/London

[7.12] Ikeda T, 1990, Fundamentals of Piezoelectricity, Oxford University Press, Oxford/New York/Tokio

[7.13] Moheimani SOR, Fleming AJ, 2006, Piezoelectric Transducers for Vibration Control and Damping, Springer Verlag, London

[7.14] Proakis JG, Manolakis DG, 1988, Introduction to Digital Signal Processing, McMillan Publishing Company, New York

[7.15] van den Bosch PPJ, van der Klauw AC, 1994, Modeling, Identification and Simulation of Dynamical Systems, CRC Press, Boca Raton

[7.16] Claes M, 2006, Frequency Domain Weighted Subspace Identification With Application To a Tape Servo System, Master Thesis, University of California San Diego

[7.17] Jacquette GA, 2003, LTO: A Better Format for Mid-Range Tape, IBM J. Res. & Dev., Vol. 47(4), pp. 429 - 444

8. Summary

In this dissertation, an experimental and theoretical analysis of sliding contacts and dynamics of tape transports has been presented. Dynamics of tape transports are important since lateral vibrations of the magnetic tape, generally referred to as lateral tape motion (LTM), limit the track density on a tape.

Tape tension transients and tape edge contact contribute significantly to lateral tape motion in tape transports. An optical non-contact tape tension sensor was implemented and used to characterize tape tension transients during tape drive operation. Good correlation between tape tension transients and LTM was found. Furthermore, a new method to measure tape edge contact force, based on acoustic emission, has been introduced. After calibrating the acoustic emission (AE) probe, it was used as an "artificial flange", to measure impact force. The AE sensor was fixed just above a roller in a tape drive, thereby replacing the original flange. Using this method, it was observed that tape edge contact creates LTM, especially in the 1-2 kHz frequency range. Additionally, tape edge impact force was observed to be most severe for a half full tape pack. A simplified one-dimensional impact oscillator model was shown to predict tape edge contact well.

In this dissertation, the dynamic behavior of a tape as it moves over a cylindrical guide has been investigated theoretically as well as experimentally. The equation of motion was derived and solved numerically. The model was then validated with

experimental data. Good agreement between the model and the experiments was found in the time domain as well as in the frequency domain. Using this model, we have investigated the effect of bending stiffness on tape dynamics. In addition, the influence of operating parameters on LTM was studied, as the tape moves over a cylindrical guide. The tape/guide contact length, which is function of the wrap angle and the guide radius, was found to have a major influence on LTM, while the influence of tape tension, friction coefficient and tape thickness appeared to be less significant.

When the tape is in contact with tape drive components such as a cylindrical guide, the tape dynamics are related to frictional interaction between the tape and the guide surface. Therefore, a model for the dynamic friction coefficient between the polymeric tape and a metallic cylindrical guide was proposed. The model extends the well-known "belt-drive" equation and introduces the effects of operating and design parameters on the tape/guide friction coefficient. Both load sharing and asperity contact effects were taken into account. The theoretical predictions of the model showed good agreement with experimental measurements of the tape/guide friction coefficient.

The last part of the dissertation focuses on improvements that can be made to tape transport design in order to yield lower LTM and thus improved tape transport. First, the idea of laser surface textured (LST) guides was presented. The surface of LST guides are covered with micro-dimples which enhance the formation of an air bearing, compared to smooth guides. Enhanced air bearing formation was shown to reduce the transition speed between boundary lubrication and hydrodynamic lubrication. The

friction coefficient was found to be almost independent of the tape speed, when using LST guides. This is very beneficial to avoid tape wear during start/stop of a tape drive and provides stability to the tape drive operation. The effect of LST on the friction coefficient was investigated experimentally as well as numerically.

Another improvement that can be made in commercial tape drives is the introduction of a dual stage actuator head. The tape head, actuated by a voice coil motor (VCM), and controlled by a servo loop, attempts to follow the lateral tape motion. To improve the bandwidth of the servo controller, the implementation of a second stage actuator, based on a piezo crystal, was proposed. The main idea is that the VCM stage follows the low frequency LTM (< 1 kHz), while the second stage follows the high frequency LTM (> 1 kHz). The second stage moves only the air bearing surface with the read/write heads while the VCM actuates the whole tape head mass. Hence, only a small mass needs to be actuated by the second stage. This increases the bandwidth. A prototype of a dual stage actuator head was built and tested. The dynamics of the newly proposed dual stage actuator head was investigated and captured in a mathematical model. The dynamics of the model showed good agreement with experimental observations. The prototype promises excellent performance in following high frequency LTM up to 2.5 kHz, which represents a bandwidth expansion of at least 1.5 kHz compared to current state-of-the-art commercial tape drive heads.

As track density needs to be increased to accommodate higher recording densities, LTM needs to be reduced. A thorough understanding of sliding contacts and friction is

essential in achieving this goal; improved guiding technologies need to be developed. A novel idea could be “active guiding”, where a guide is controlled by a servo actuator and can be tilted to “steer” the tape laterally, thereby counter-acting the LTM. Also, the effect of the laterally actuated tape head on the LTM in the tape path, due to frictional coupling between the air bearing surface and the tape, needs to be fully understood. The development of a complete tape path simulator that captures the exact mechanics of the tape and the tribological interaction between tape and tape drive components would also be desirable for simulating the next generation tape transports.

In conclusion, tape technology is a dynamic, interdisciplinary research area. New areas of interest are evolving continuously, creating new challenges for engineers and researchers in academia as well as industry.